Novel metrologies of thermophysical properties on the nanoscale

A Dissertation presented to the
faculty of the School of Engineering and Applied Science
University of Virginia

In partial fulfillment
of the requirements for the degree of
Doctor of Philosophy
Mechanical and Aerospace Engineering

Thomas Wayne Pfeifer
May, 2025

APPROVAL SHEET

The dissertation is submitted in partial fulfillment of the
requirements for the degree of

Doctor of Philosophy in Mechanical and Aerospace Engineering

Thomas Wayne Pfeifer

This dissertation has been read and approved by the Examining Committee:

Patrick E. Hopkins, Advisor

Ethan A. Scott, Chair

Jon F. Ihlefeld

Prasanna V. Balachandran

Eric R. Hoglund

Accepted for the School of Engineering and Applied Science:

Jennifer L. West, Dean
School of Engineering and Applied Science

May, 2025

Abstract

The measurement of thermal properties on the micro- and nano-scale is essential for understanding fundamental thermophysical phenomena such as heat flow and phase change. Existing measurement techniques (such as Time Domain (TDTR), Frequnency Domain (FDTR), or Steady State (SSTR) Thermoreflectance) or simulation techniques (such as lattice dynamics (LD) or molecular dynamics (MD)) have offered key insights into some of the fundamental principles of heat transfer over the last few decades. Several properties and length-scales have persisted which cannot be simulated or measured however. Similarly, there is little consensus within the nanoscale thermal measurement community as to the correct means by which measurement error and experimental uncertainty should be characterized.

Over the course of my studies at The University of Virginia, I have done work on several topics in this area. These topics can be broken down into three primary thrusts. To begin, I present several advancements in the analysis of existing measurement techniques ("Development of new analysis methodologies for existing measurement techniques"). As a prerequisite to this, I identify and outline the sources of measurement error and uncertainty associated with the existing measurement techniques, as these serve to limit whether a given thermal property can reasonably be measured. I next expand TDTR for use as a depth-dependent thermal conductivity measurement, and present a hybrid fitting analysis method for simultaneous analysis of TDTR and SSTR data. In both cases, additional thermal properties can be extracted which could not have otherwise been measured. Next, I will discuss computational advancements ("Advancements to computational techniques"), starting with Spectral Heat Flux (SHF) and disorder analysis. These tools helped to elucidate the underlying mechanisms of thermal boundary resistance (TBR), highlighting the effects of scattering within the two materials on either side of an interface. I have also developed a method of exciting specific targeted phonon modes in an effort to explore the

effects on TBR, based on the hypothesis that overexciting modes could increase scattering and lead to a reduction in TBR. Finally, I present the development of two new measurement techniques ("Development of new experimental metrologies"). The first is an optical pump-probe experiment for defect detection, taking advantage of the exceptional signal-to-noise available using lock-in detection and the ability of defects to strongly affect the optical and electronic properties of materials. The second is a pump-probe micro-scale calorimetry technique, wherein the pump beam melts a portion of the sample, and the temporal signal is analyzed to determine the latent heat.

Acknowledgements

I have many to thank for their role in helping me reach this point. I thank my parents for instilling in me a great curiosity, wonder, and desire for endless learning. “If you’re the smartest person in the room, you’re in the wrong room” and “when you stop learning, it’s time to keep moving”. I thank my dogs, Bailey, Cooper, and Kuma, for the emotional support when times were stressful. I also thank Bailey for *making* some of those times stressful...it’s all about balance. I thank my girlfriend, Hannah, for her infinite support and patience. I also thank her for taking the leap to move with me to Tennessee so I could fully immerse myself in microscopy. I thank my many wonderful colleagues who distracted me endlessly on side-quests, but who also lent great insights on various fronts. A distraction is just an idea for more projects, in disguise. I thank my advisor, Patrick, for trusting in me when I did other interesting stuff instead of what he asked. It’s only a rabbit hole if it doesn’t come to anything. I thank Hutchins and Harrison for the nonstop science chats, both in the lab and at conferences. I thank Eric for taking me under his wing so I could enter and explore the wild and wonderful world of electron microscopy. Finally, I thank my friend Henry for sending on this trajectory in the first place.

Contents

List of Figures

List of Tables

Chapter 1

Introduction

1.1 Motivation

At a fundamental level, thermal properties are dominated by nanoscopic effects such as the scattering of phonons from boundaries, impurities, and structural defects. Similarly, thermal properties on the nanoscale often differ from that of bulk materials. The role of interfaces on thermal transport is also a key interest, as the resistance associated with a material interface may dominate the thermal management in certain applications.

Examples of this are included in Fig. 1.1. In a transistor (particularly those for high-power applications, shown upper right), many layers of material may be present. The fundamental principle of the operation is similar in any field-effect transistor (FET). In a semiconductor, the Fermi Energy (maximum energy of the highest filled electron state at 0 K) is positioned between electron bands (the filled and unfilled bands being referred to as the valence and conduction band respectively). If both bands are entirely populated/unpopulated, no charge can flow, and the material is electrically insulative. Conversely, the semiconductor can be doped: p-type or n-type, i.e., with fewer electrons in the valence band or electrons present in the conduction band, respectively. This makes the semiconductor electrically conductive. Within the FET, a voltage applied to the gate moves the electrons or holes (spatially). Depending on the type of transistor and whether the semiconductor is p-type or n-type, this controls the carrier mobility within the semiconductor between source and drain contacts, turning the FET on or off. In some architectures (such as the vertical GaN device shown [1]) multiple layers of multiple materials may be required: here a middle semi-insulating layer serves as a switch, and requires additional adjacent n-doped (electron-rich) regions to supply electrons to reach a highly-conductive state. Within each layer, thermal conductivity may be dominated by phonon-phonon scattering, boundary scattering, or microscale defect scattering (upper left). Individual atomic defects (such as crystalline disorder or impurities) can also contribute to phonon scattering, inhibiting heat flow. Interfacial resistances also result from the scattering of heat carriers (middle left). Other macroscopic thermal phenomena such as melting also depend on nano- or atomic-scale behavior, i.e., the rearrangement of atoms. Phase change memory devices (lower right) are an example of a practical application of this. In these devices, differing phases can be obtained through heating (e.g. $Ge_2Sb_2Te_4$, crystalline to amorphous [2]), and probed via the measured electrical resistivity. This offers a mechanism by which bits can be written and stored in a fast and non-volatile manner, and memory devices are currently being developed based on this premise.

The ability to measure these properties (using both micro- and nano- scale measurements) is critical for allowing engineers to accurately model thermal management within a wide range of applications. Similarly, a fundamental understanding of these mechanisms can aid in material design and selection, and simulations are often used to elucidate phenomena which may be difficult or impossible to measure directly.

1.2 Theory of phonons

A phonon is a vibrational wave within a crystal (i.e., the collective oscillatory motion of atoms), defined as having both a frequency and a wavelength. These wave-like vibrations contain thermal energy (contributing to the heat capacity of the crystal) and carry thermal energy (contributing to the thermal conductivity of the crystal). By understanding

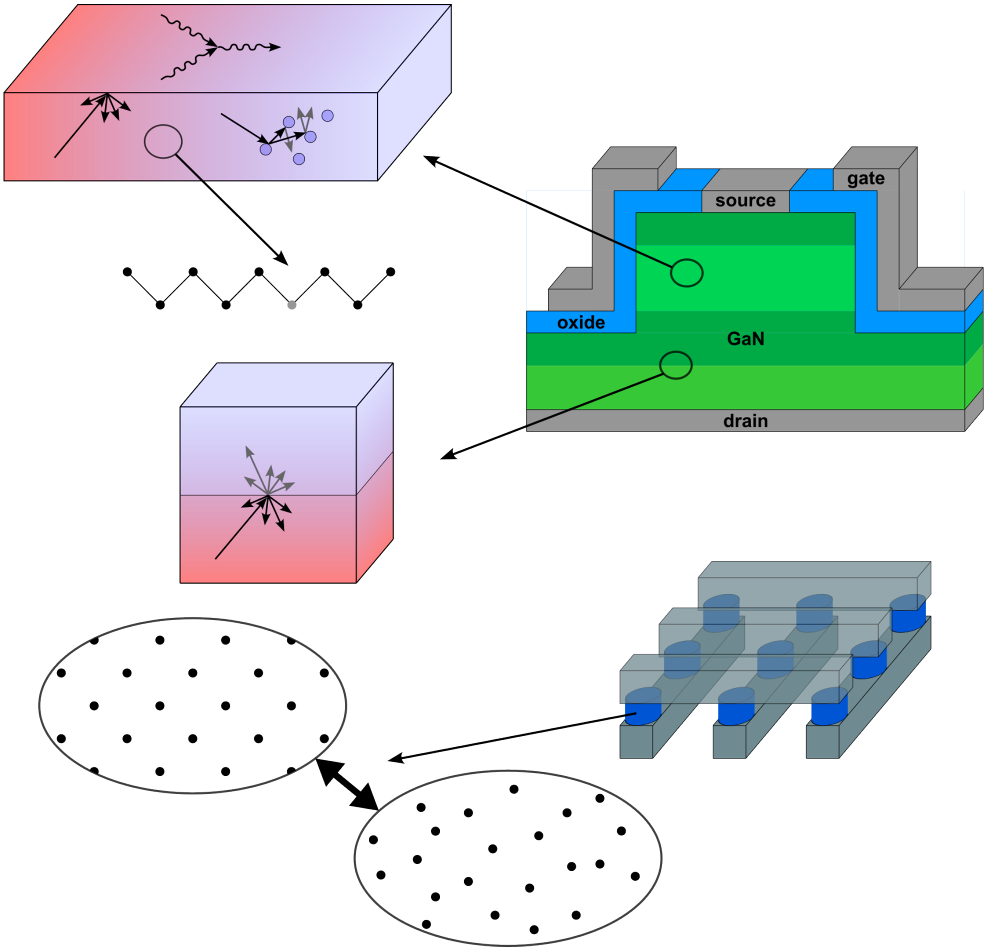

FIGURE 1.1: A high-power GaN transistor is shown (upper right), where the thermal properties of each layer may be dominated by boundary scattering, phonon-phonon scattering, or defect scattering (upper left). Defect scattering can occur on the microscale (e.g., from nanoparticles or voids), or atomic-scale (e.g., from crystalline disorder or impurities). Thermal resistances across interfaces (middle left) may also limit thermal dissipation. Phase change, such as in a phase change memory device (lower right) is also dominated by atomic-scale behavior (lower left).

the behavior of these waves, thermal properties of crystalline materials can be understood, including the effects of interfaces, defects, and other disorder. Many of the principles of thermal transport in crystals can also be extended to semi-crystalline or amorphous materials. This means an understanding nanoscale thermal transport in crystals is a necessary first step before consideration of non-crystalline or defected materials.

1.2.1 Basic theory

To understand phonons, it is easiest to approximate a crystal as a series of masses (atoms of a defined mass) on springs (interatomic bonds, with varying stiffness) [3–5]. Assuming the system begins in a relaxed state (i.e., there is no net force on a given atom), then for a displacement u of a single mass (atom), a restorative force will exist from the stretching and compression of the connected springs (bonds). For a single spring (with a spring constant s) following Hooke's Law, this force can be written as:

$$F = -s \cdot u \tag{1.1}$$

The acceleration of the mass due to this force (assuming Newtonian physics) will be:

$$\ddot{u} = \frac{F}{m} \tag{1.2}$$

which is a simple rearrangement of the traditional $Force = mass \cdot acceleration$, and using the notation where $\dot{u} = \frac{du}{dt}$ and $\ddot{u} = \frac{d^2u}{dt^2}$. If neighboring atoms are also displaced, the force on atom n will also depend on the displacements of adjacent atoms $n-1$ and $n+1$, and the previous expression complicates slightly to:

$$F_n = s_{n-1} \cdot (u_{n-1} - u_n) + s_n \cdot (u_{n+1} - u_n) \tag{1.3}$$

While it may not always be the case, it is useful to make the simplifying assumption that the spring constants between atoms $n-1$ and n and n and $n+1$ are equal ($s = s_{n-1} = s_n$). To solve for the motion of all masses within the system, we thus seek a solution to the system of equations linking the motion of each mass to the forces applied between each mass:

$$m_n \cdot \ddot{u}_n = s \cdot (u_{n-1} - 2 \cdot u_n + u_{n+1}) \tag{1.4}$$

Assuming a plane-wave solution following the form:

$$u_n = A_n \cdot exp(i \cdot k \cdot x) \cdot exp(i \cdot \omega \cdot t) \tag{1.5}$$

where x is the atomic position, k is the wavevector (inverse of the wavelength), and ω is the frequency of oscillation, then:

$$\ddot{u}_n = -\omega^2 \cdot u_n \tag{1.6}$$

and thus:

$$-\omega^2 \cdot m_n \cdot u_n = s \cdot (u_{n-1} - 2 \cdot u_n + u_{n+1}) \tag{1.7}$$

The motion of each atom can then be represented in matrix form:

$$\begin{bmatrix} 2 \cdot s - \omega^2 \cdot m_0 & -s & 0 & \dots & 0 \\ -s & 2 \cdot s - \omega^2 \cdot m_1 & -s & \dots & 0 \\ 0 & -s & 2 \cdot s - \omega^2 \cdot m_2 & \dots & 0 \\ \vdots & \vdots & \vdots & \ddots & \vdots \\ 0 & 0 & 0 & \dots & 2 \cdot s - \omega^2 \cdot m_n \end{bmatrix} \begin{bmatrix} u_0 \\ u_1 \\ u_2 \\ \vdots \\ u_n \end{bmatrix} = 0$$

Considering a system with fixed boundary conditions of n atoms, the eigenvalue solutions yield n values for ω.

For a periodic system (i.e., atom n is the same as atom -1), a slight modification is required. The motion of atom n is the same as atom -1, however there will be a spatial phase shift of $exp(i \cdot k \cdot a)$ where a is the periodicity of the repeated structure. For the periodic system with a “monatomic basis” (i.e., every atom is the same, every spring constant is the same, and a is the interatomic spacing), the matrix reduces to a single cell and we seek solutions for the expression: $-\omega^2 \cdot m = s \cdot (exp(i \cdot k \cdot a) + exp(-i \cdot k \cdot a) - 2)$. For this monatomic case, there are infinitely many solutions for k, with one value of ω for each k. Alternatively, a system with an n-atom basis (repeating every n atoms) can be found using the same procedure, using the modification to the above matrix expression with the periodic boundary condition applied:

$$\begin{bmatrix} 2\cdot s-\omega^2\cdot m_0 & -s & 0 & \dots & -s\cdot exp(-i\cdot k\cdot a) \\ -s & 2\cdot s-\omega^2\cdot m_1 & -s & \dots & 0 \\ 0 & -s & 2\cdot s-\omega^2\cdot m_2 & \dots & 0 \\ \vdots & \vdots & \vdots & \ddots & \vdots \\ -s\cdot exp(i\cdot k\cdot a) & 0 & 0 & \dots & 2\cdot s-\omega^2\cdot m_n \end{bmatrix} \begin{bmatrix} u_0 \\ u_1 \\ u_2 \\ \vdots \\ u_n \end{bmatrix} = 0$$

for which there are n values of ω for any given value of k. Plotting the resultant ω and k values (referred to as "modes") will yield what is referred to as a "phonon dispersion". Two simplified phonon dispersions are included below, showing the frequencies and wavevectors for a monatomic and diatomic 1D chain. Note that the concept of n eigenvalue solutions mentioned previously for finite systems still holds, and the dispersion shown will be discretized. For a system with n atoms along its length, there will be n points along k. In 3 dimensions, this will extent to $3\cdot n$ for motion in 3 directions, i.e., there will be vibrational motion along the direction of the wave (termed "longitudinal") and in the two perpendicular directions (termed "transverse").

Several key observations can be made based on the phonon dispersion. First, the ratio of ω/k for any given mode (units of $rad\cdot s^{-1}$ for ω (or s^{-1} given a 2 π scaling), divided by m^{-1} for k, yielding $m\cdot s^{-1}$) is the phase velocity of the individual mode selected. For several adjacent modes, if there is a slight mismatch in their phase velocity, this will result in constructive/destructive interference and may appear as a "wave packet". The level of interference will depend on the relative velocities of the modes involved, and the velocity of this packet will end up being equivalent to the slope of the dispersion (group velocity).

The effect of mass and bonding can also be explored. Using the math above, one will find that low masses (light atoms) and large spring constants (stiff atomic bonds) will result in higher frequencies of vibration. Diamond is one example of a material with exceptionally high thermal conductivity, resulting in part from the exceptionally strong bonds (carbon-

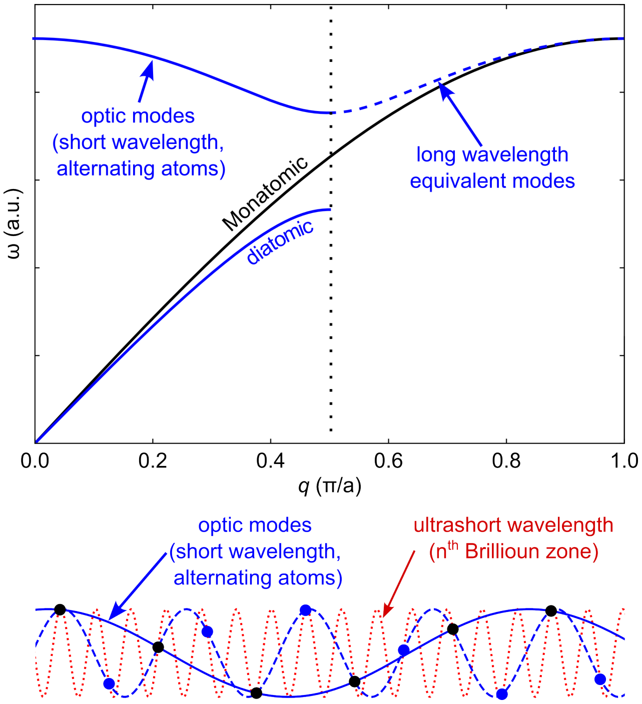

FIGURE 1.2: Phonon dispersions are shown for a monatomic chain (black) and diatomic chain (blue), scaled such that their wavelengths match (and a would denote the interatomic spacing). We typically define the shortest wavelengths present ($k_{max} = \frac{\pi}{a}$) based on the periodicity of the system. The wave is sampled at each atomic site however (and only at the atomic sites). This means long wavelength waves (small k) affecting alternating lattice sites (solid blue) are equivalent to short wavelength waves (large k) affecting every lattice site (dashed blue). This is further equivalent to waves with a sub- interatomic-spacing wavelength (dotted red).

carbon sp^3 bonding) and light atoms, which yield high phonon frequencies and velocities. Similarly, the differences in masses, bonding, or breaking of symmetry will result in the opening of what is referred to as the “forbidden band” or “phonon band gap”.

The motion of specific lattice sites can also be found by plugging each solution of ω and k back into the original expressions. One will find that for the diatomic case, the higher-frequency modes will appear as alternating atoms vibrating out of phase with respect to each other. Considering the frequency/wavelength relationship for light (i.e., all colors of light travel at the same speed, meaning a dispersion would be a line with a slope of $c = 3\times10^8$ m s^{-1}), these higher-frequency out-of-phase modes can directly couple to light, and are thus referred to as “optic modes”.

While the wave only technically exists at the atomic locations, multiple sets of equivalent waves exist. Long wavelength waves (small k) coherently affecting alternating lattice sites (optic modes) are equivalent to short wavelength waves (large k) affecting every lattice site. This allows for a form of “unfolding” of the optic modes. Evidence of this will be shown in my Spectral Energy Density calculations (discussed in depth in the chapter titled “Phonon pumping in MD: Exploring the possibility of switchable Thermal Boundary Resistance"), and a depiction of this is shown in Figure 1.2 above. This unfolding can be taken further as well, where exceptionally-short wavelength waves (far smaller than the interatomic spacing) also match the motion of the atoms. In reciprocal space, the first division of the system periodicity is referred to as the first Brillouin zone (for which the phonon dispersion is shown above), however the phonon dispersion can be unfolded indefinitely into subsequent Brillouin zones. Although it may seem counterintuitive to consider a "vibrational wave of atoms" as having a wavelength smaller than the interatomic spacing (and thus only the first Brillioun zone is typically visualized), these ultra-short wavelength modes still fully satisfy the motion of the atoms, and many interesting phenomena result.

Everything discussed so far is in the context of a classical description of atomic motion ($Force = mass \cdot acceleration$), however phonons are often discussed as quantum particles. In the classical description, the energy contained in a vibration is in the form of kinetic energy (the motion of the atoms) and potential energy (the stretching of springs), both of which are tied to the amplitude of the vibration. A quantum treatment of the same problem will reveal quantization of the energy for each mode (i.e., discrete allowable levels for a single mode's population). Scattering would then be discussed in terms of phonon creation and annihilation (as opposed to changes in a vibrational wave's amplitude). It should be noted that this quantization is a distinctly different concept from the discretization across k (relating to having $3 \cdot n$ modes in a given direction) for a finite-sized system. In Molecular Dynamics, the quantization of energy levels and atomic motion is not captured, and many physical phenomena (phonon dispersions, thermal conductivity, thermal boundary resistance, etc.) can all be accurately described and calculated via the classical description. For this reason, and for the sake of simplicity, I will largely draw on the classical description in this work. The interested reader is strongly encouraged to explore the works of Gang Chen [5] (begining with chapter 3.3.2), Gyaneshwar Srivastava [4] (chapter 2.1.1), or Charles Kittel [3] (chapter 5), in this order. The quantum origin of a given expression may not always be clear, but the presence of Planck's (or reduced) constant should be a clue.

Finally, it should be noted that the phonon dispersion merely represents the available vibrational states within a given material, and that not all states are equally populated. Phonons adhere to the Bose-Einstein distribution, where low-frequency vibrations have a significantly higher amplitude than the high-frequency vibrations of the same system.

1.2.2 Thermal conductivity

For an uninterrupted wave, energy is carried without resistance. This is referred to as "ballistic transport" and for phonons traveling over short distances, this can make up a substantial quantity of energy flow. For bulk materials however, the wave is eventually disturbed, either from something structural (e.g., a boundary or defect) or by other waves within the system (termed "phonon-phonon scattering"). The distance a wave travels before being disturbed (or "scattered") is not a fixed value, but the mean is referred to as the "mean free path", and is proportional to the wave velocity and the scattering rate. Scattering thus determines nearly all macroscopic transport properties attributed to phonons, and an understanding of scattering is required to understand the effects of defects and boundaries. Mathematically, the thermal conductivity of a material can be considered to be the sum of all energy carried by all modes:

$$K = \sum \frac{1}{3} C(\omega, k) \cdot v(\omega, k) \cdot l(\omega, k) \tag{1.8}$$

where each mode (ω, k) contains a set amount of energy $C(\omega, k)$, traveling at a set velocity $v(\omega, k)$ for a finite distance $l(\omega, k)$. This can also be expressed terms of scattering rates:

$$K = \sum \frac{1}{3} C(\omega, k) \cdot v^2(\omega, k) \cdot \tau(\omega, k) \tag{1.9}$$

where $\tau(\omega, k)$ is the time between scattering events ($l = v \cdot \tau$). Considering the mode velocity in the above expressions, and all else equal, these relations would suggest that optical modes ought to have a minority contribution to thermal conductivity (and this is generally true), given the relatively low slope (low group velocity) of optical branches. While discussing the 1D atomic chains in the previous section, I also noted that materials with strong bonding and light atoms will have high phonon frequencies and velocities. These materials will also tend to have the highest thermal conductivities [6] as a result. Low-temperature thermal conductivity trends of crystals can also partially be understood in this context. As more modes are populated according to Bose-Einstein statistics, additional modes are made available to carry heat, and the thermal conductivity increases.

Alternatively, we can consider the effects of scattering from the above expressions. While some modes may not carry substantial amounts of heat, they may also serve to scatter with other modes (reducing those modes' scattering times τ), thereby reducing the overall thermal conductivity. This can help us in understanding high-temperature thermal conductivity trends of crystals: as additional modes are populated, additional scattering channels are made available, which yields a reduction in thermal conductivity as temperature increases. Phonon-phonon scattering also explains why simpler crystal structures tend to yield higher thermal conductivities (e.g., those with diamond cubic structure [6]), while complex structures with many phonon branches will yield lower thermal conductivities despite reasonable bond strengths (as is the case with Ga_2O_3 [7]). Materials with a complex crystal structure will have more branches in the phonon dispersion, presenting greater opportunity for phonon-phonon scattering.

Phonon-phonon scattering is typically broken down into normal and Umklapp processes. In normal scattering, multiple phonons can interact assuming a set of frequency (related to the phonon energy) and wavelength (related to the phonon momentum) matching conditions are met. In the previous section, I also highlighted a form of wavelength equivalency, where long wavelengths (small k) within the first Brillouin zone are equivalent to short wavelengths (large k) within subsequent Brillouin zones, since the waves are only sampled at the atomic sites. For Umklapp scattering processes, the same momentum-matching conditions apply, however modes interact across Brillouin zone boundaries. Considering Brillouin zone folding/wrapping, this appears as a change in total momentum (and Umklapp scattering is often referred to as non- momentum conserving). Umklapp is a dominant form of scattering for optical modes and at high temperatures [8, 9], contributing to a reduction in thermal conductivity.

In additional to phonon-phonon scattering, defects and boundaries may also contribute. Defects are thought to primarily affect waves with similar length scales. Sound waves with frequencies in the hundreds of Hz and wavelengths on the order of a meter, when traveling through the air, are not significantly affect by micrometer-scale dust particles. For this reason, the length scales of defects are often considered, with nanoparticles capable of scattering a majority of modes, and point-defects and impurities scattering only the shortest-wavelength modes. Thin films will also have reduced thermal conductivity due to phonon scattering at the boundaries. By considering the film thickness as the longest distance a phonon can travel before being scattered (i.e., the longest mean free path in the above expression), then a reduction in conductivity of a film can be estimated.

Finally, the shape of the interatomic well (or how closely the realistic bond stiffness matches that of the idealized spring) will affect phonon scattering. As an atom vibrates substantially away from its lattice site, the force is no longer linear with respect to displacement (Hooke's law used in the derivation above), which means each mode is no longer a simple harmonic oscillation. For a harmonic oscillation, a single frequency is present, however the presence of additional adjacent modes (anharmonic frequencies) presents an additional opportunity for scattering.

1.2.3 Thermal boundary resistance

Unlike a localized defect which merely scatters a wave, the phonon populations on either side of an interface between two materials are necessarily different. Energy must be converted between phonons within the two materials (or certain modes may be prevented from directly transmitting energy across the boundary) which results in an additional thermal resistance at an interface (even aside from issues of bonding, poor adhesion, or a reduced contact area due to surface roughness). This resistance goes by many names: "thermal boundary resistance" (TBR), "interfacial thermal resistance" (ITR), or by it's inverse “thermal boundary conductance” (TBC, not to be confused with “thermal barrier coatings”), or “thermal interface conductance” (TIC). When referring to an atomically perfect and abrupt interface specifically, this can also be called “Kapitza resistance” (R_K) [10]. Typically, the wavevector component of the phonon dispersion is neglected (the phonon dispersion above was derived assuming a semi-infinite medium). Instead, the frequencies of atomic vibrations are considered for both materials (termed “density of states”), and a mismatch results in a thermal resistance at the interface [10–12]. In the acoustic mismatch model (AMM) [13, 14], waves either transmit or reflect off an interface, and only the transmitted waves’ portion of energy passes across the interface. This is the same principle by which light reflects or transmits through a surface, or by which an electron wave transmits or reflects off a stepped potential. AMM is applicable at low temperatures (where only long wavelength modes are populated, as per Bose-Einstein), but fails at higher temperatures. Alternatively, the diffuse mismatch model (DMM) [11] suggests *all* modes should scatter at a boundary. This is why the phonon density of states is typically considered instead of the full phonon dispersion (i.e., phonon momentum is not maintained). According to this model, pairs of materials with more overlap in their density of states should see a lower thermal boundary resistance. While AMM limits the transmission of energy to those waves which directly cross the interface without scattering (and may thus over-predict TBR), DMM allows all vibrations to transmit energy (and often under-predicts TBR).

1.3 Thermoreflectance measurements

Several existing thermoreflectance techniques [15–18] are popular for nanoscale thermal measurements. These methods are all fundamentally similar; a pump laser is used to heat a sample, and a probe laser is used to measure changes in reflectivity, which are indicative of changes in temperature. This is typically a surface measurement, with both lasers focused onto the same side of the sample. Thermal dissipation into the sample affects the surface temperature, meaning there is (limited and varying) sensitivity to properties deeper within the sample. A thin metallic coating (transducer) is typically used to isolate the heating to the surface and to provide an optically opaque and reflective surface for the probe. Collected data is fit to an analytical thermal model in order to back out one or more unknown thermal properties, with the type of data collected being dependent on the specific technique used. It should be noted that the changes in reflectivity are extremely small (hundredths or thousandths of a percent [19, 20]), which means a lock-in detection scheme is required. By modulating the pump laser at a given frequency, a lock-in amplifier can be used to detect the pump-induced changes at the same frequency, and extremely small changes in reflectivity can be measured. A lock-in amplifier returns the amplitude of the signal at the designated frequency ("M" in Figure 1.4.b below), and the phase angle between the oscillatory signal and a reference wave ("ϕ" in Figure 1.4.b). Alternatively, the in-phase and out-of-phase signals can be considered (where $V_{in} = M \cdot cos(\theta)$ and $V_{out} = M \cdot sin(\theta)$).

Thermoreflectance experiments can be broken down into three distinct categories. In time domain experiments, the temporal temperature response is recorded. The most popular example of this is Time Domain Thermoreflectance (TDTR) [15] in which a pulsed laser is used. In TDTR, the arrival of pump and probe pulses is temporally offset by adjusting the path length of one of the beams. This is fundamentally a stroboscopic measurement, where the thermal decay is only sensed by the time-delayed probe pulse, and the whole thermal decay is reconstructed by adjusting the time delay. The schematic for the apparatus used and an example dataset are shown for TDTR in Figure 1.3.a,c. Note that while it is commonly referred to as a thermal decay, the ratio of in-phase and out-of-phase signals are typically used for analysis. This means the decay measured is not the decay which would be observed following a single pulse. Analyzing the ratio of V_{in} and V_{out} eliminates the need for normalization of the data however. Another newer technique, Square Pulse Thermoreflectance (SPTR) [18] uses a square-modulated continuous wave (CW) beam, and a periodic waveform analyzer is used to record the temperature rise and decay. The response of the system at varying frequencies can also be recorded (as in Frequency Domain Thermoreflectance - FDTR), using either pulsed or CW lasers [16]. The pulsed-FDTR

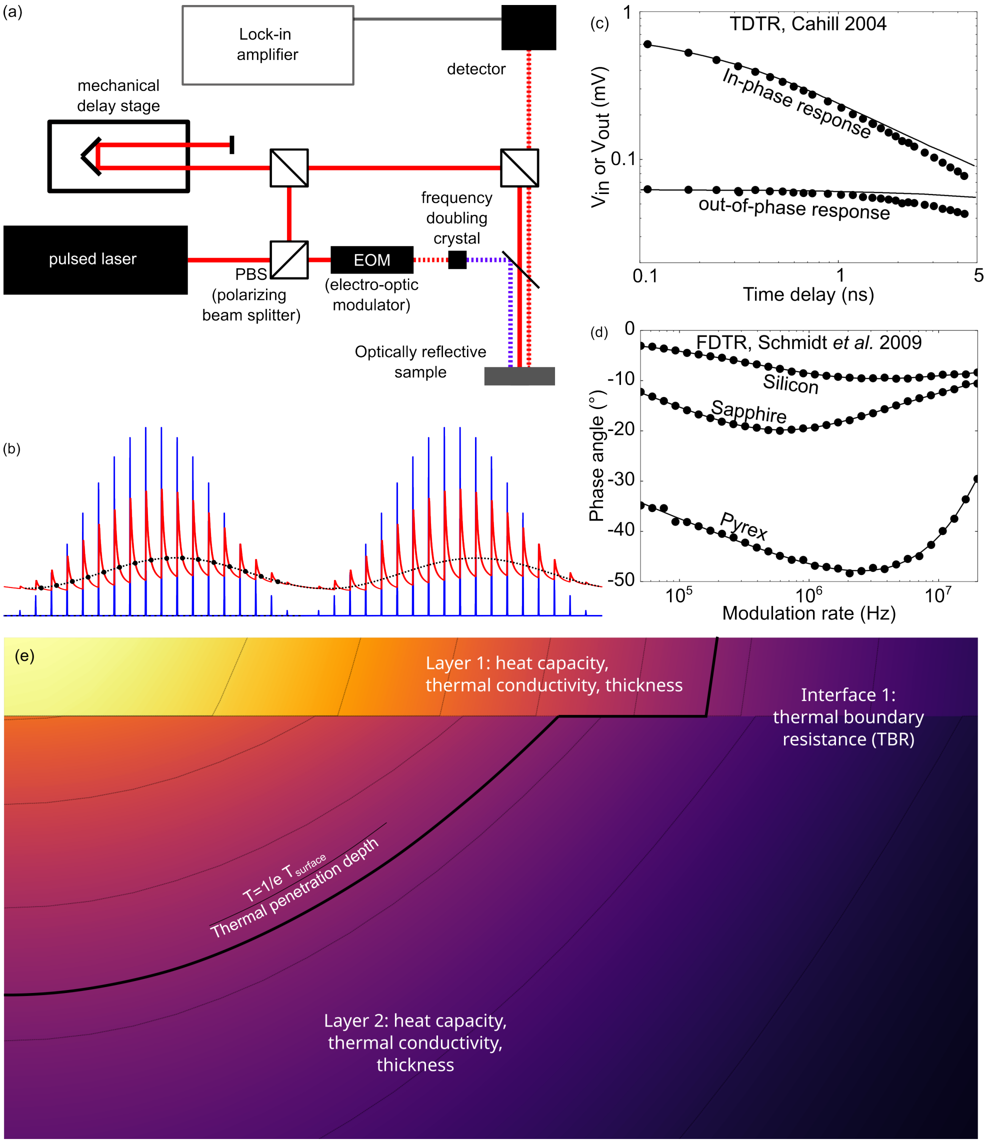

FIGURE 1.3: (a) Schematic of the pulsed thermoreflectance experiments. A retroreflector mounted on a translation stage can be used to adjust the pump and/or probe path length, changing the temporal delay between the arrival of the pump and probe pulses to the sample. (b) The pump waveform is shown in blue (a modulated train of pulses) and a heating waveform shown in red (a slightly-different thermal decay for each pulse). The time-delayed probe samples each thermal decay at the same point, and the lock-in acquires the magnitude and phase of the resulting sinusoidal signal (black dotted). Example datasets are shown as a function of time delay (c) as in Time Domain Thermoreflectance (TDTR), and as a function of modulation frequency (d), as in Frequency Domain Thermoreflectance (FDTR). (e) a multi-layer analytical model is used to fit for unknown thermal properties. Notably, the size of the measured volume (referred to as a thermal penetration depth - TPD) depends on the modulation rate, thermal properties, and/or the pump and probe spot sizes [21, 22]

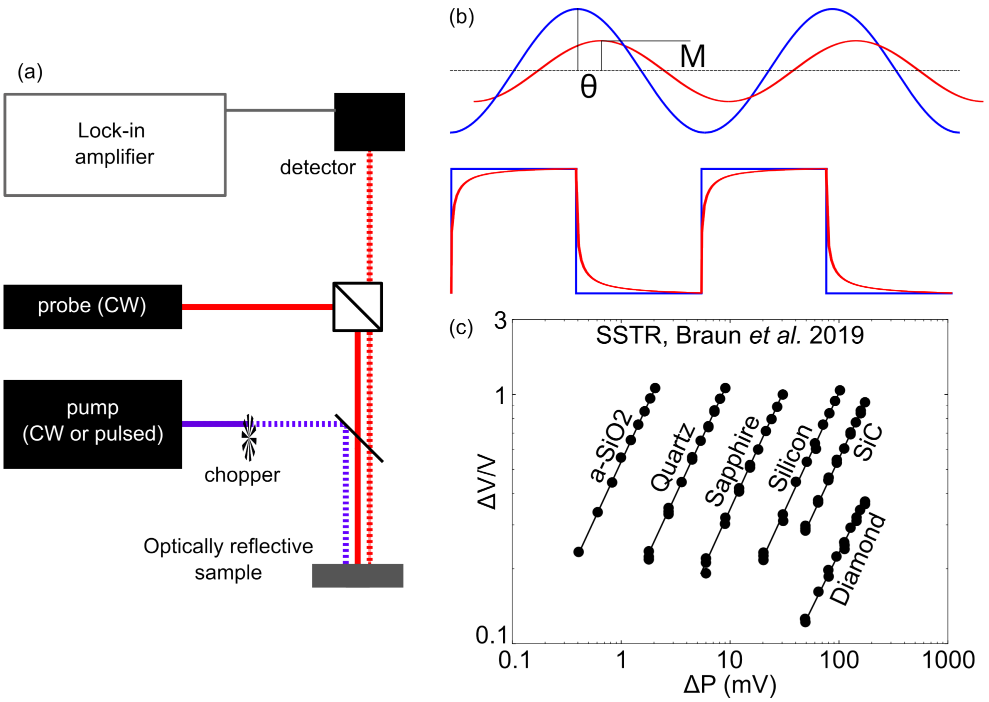

FIGURE 1.4: (a) Schematic of the continuous-wave (CW) thermoreflectance experiments. The CW pump beam is modulated as before, and a CW probe monitors pump-induced changes in temperature. Example waveforms are shown in (b), with thermal information embedded in the phase and magnitude of the thermal response. For Steady State (SSTR) (c) and Frequency Domain Thermoreflectance (FDTR) measurements, the waveform does not matter, as the lock-in amplifier picks up the component of the Fourier series at the modulation frequency. For Square Pulse Thermoreflectance (SPTR), the time-domain square-wave heating is modeled similarly to TDTR, simply by considering the Fourier series for the square wave. An expansion of this enables time-domain analysis on an arbitrary waveform, which my code accurately captures (published on GitHub: https://github.com/ExSiTE-Lab/TDTR_fitting)

apparatus is the same as that used by TDTR shown in Figure 1.3.a, the CW apparatus is shown in Figure 1.4.a, and an example dataset is shown in Figure 1.3.c. Finally, the applied pump power can be varied and the magnitude of the temperature response monitored (as is done in Steady State Thermoreflectance - SSTR) [17]. This uses the same CW apparatus as FDTR (Fig. 1.4.a), but the probe magnitude response as a function of pump power is analyzed (Fig. 1.4.b). When the magnitude of the signal is analyzed in TDTR or FDTR, the signal is normalized, since numerous experimental scaling parameters may be present (e.g., thermoreflectance coefficient, photodetector sensitivity, and optical losses through lenses and mirrors). In SSTR however, a slope scaling term (γ) is calculated from measurements on a known reference sample (known thermal properties, identical transducer) in order to avoid the need for normalization.

It should be noted that each different type of measurement and the experimental conditions (e.g., modulation frequency, the focused spot sizes of both lasers, transducer material and thickness) yield differing sensitivity to the thermal properties of the sample, meaning one's choice of experiment (or the need for multiple) should depend on the sample under consideration. For example, low modulation frequency measurements (as in SSTR) may be insensitive to heat capacity, reducing the number of assumptions required in some cases. Similarly, the effective measurement depth can vary from hundreds of nanometers [21] (as in TDTR at high frequencies) to tens of microns [22] (as in SSTR with large spot sizes). The measurement depth is often referred to as the "thermal penetration depth" which is the depth at which the temperature of the sample reaches 1/e that of the surface. For 1D thermal dissipation (as in TDTR or FDTR at high frequencies), this can be calculated as:

$$d_{thermal penetration} = \sqrt{K \cdot \pi^{-1} \cdot C^{-1} \cdot f_{mod}^{-1}} \tag{1.10}$$

where K is the thermal conductivity, C is the heat capacity, and f_{mod} is the modulation frequency [21]. The measurement sensitivity also follows this expression, as low to negligible modulated heating at depth will yield low to negligible measurement sensitivity. For measurements at low frequencies such as SSTR, the 1D thermal dissipation assumption is no longer valid. It should be obvious that one does not have an infinite thermal penetration depth as f_{mod} approaches zero (one cannot measure the thermal conductivity of the earth's core using this technique). Instead, the laser spot sizes become the limiting factor [22], since the heated profile at steady state is approximately hemispherical with a size on the order of the pump spot size. Similarly, differing measurement depth will be found within confined geometries [23]. Alternatively, if modulated heating below this 1/e threshold is sufficient (e.g., where the order of magnitude of the measured property is of interest, or where all experimental parameters have been rigorously characterized), then deeper sensing may be considered [24].

Numerous variations of these techniques have also been used. The use of spatially-offset [25] or elliptical [26] pump and probe beams has been shown to increase sensitivity to in-plane thermal conductivity. Collecting data at multiple TDTR modulation frequencies [27–31] (also termed "hybrid" FDTR+TDTR), or analyzing TDTR data by both ratio (of in-phase and out-of-phase signal) and magnitude [32, 33], has been shown to reduce uncertainty associated with the measurement. The potential benefits (or lack thereof) of multiple measurements will be discussed in depth in the later chapters "Measurement uncertainty and systematic error" and "An algorithm for multi-measurement data fitting".

The analytical model used is the same for the four aforementioned experiments, and is derived from the analytical solution to the heat equation 1) for a layered structure, 2) under axisymmetric conditions, and 3) solved in the frequency domain [34]. For each layer, the top and bottom temperature and heat fluxes can be related, which means that by linking the temperatures and heat fluxes between layers, infinitely many layers can be considered. For the solution in the time domain, a Fourier series for the heating waveform is calculated (e.g., the sinusoidally-modulated train of pulses for TDTR, or the square wave for SPTR). The temperature response for each component frequency is then found (including both an in-phase and out-of-phase component), and the inverse Fourier transform is used to convert back into the time domain [15, 18]. Note that for both TDTR and SPTR, the analytical Fourier transform is known, however any heating waveform can be used by numerically calculating the Fourier transform and inverse (as will be discussed in depth in the chapter titled "Microscale calorimetry: Measuring enthalpy of phase change"). The cyclic flux and resulting heating waveforms for pulsed experiments are shown in Figure 1.3.d and for CW experiments Figure 1.4.b. In all cases, the analytical model is capable of generating the theoretical curve (assuming all input parameters are known). For fitting thermal properties, the model is passed through a curve fitting or minimization algorithm which adjusts the parameter(s) of interest until a satisfactory fit is reached.

1.4 Simulations

Beyond measurements, nanoscale simulations are often used for either the prediction of properties, or to elucidate underlying phenomena where direct measurement may be difficult. Many tools exist, some of which can directly predict physical properties (including heat capacity, thermal conductivity, or thermal boundary resistance (TBR)), either through calculations of the vibrational populations present, or by "measuring" the property within a simulation. Extreme caution must be taken when attempting to quantitatively predict physical properties however. For example, the selection of the interatomic potential used can affect the properties extracted, as can the simulations parameters (such as the duration of the simulation, number of atoms simulated, or geometry of the bounding box) [35–41]

Where quantitative prediction of properties is not required, toy models may suffice. In these cases, a greatly simplified model is used, which may not be able to quantitatively replicate thermal properties, but may still serve as a valuable tool for the investigation of trends. For example, many toy models use a simplified picture of bonding, by only considering the bonding between pairs of atoms (bond stretch) or triplets (bond stretching and bond angles). A simple analytical expression is then used to represent the bond stiffness (valuing computational efficiency over quantitative accuracy). While the simulated TBR or thermal conductivity within these systems may be incorrect, the ability to easily probe the vibrational behavior (DOS or dispersion) of complex systems is of value. Similarly, these toy systems can serve as a form of virtual laboratory; various changes can easily be made (e.g., changes to atomic mass, bond stiffness, anharmonicity, structure) and the effects can be monitored on an atomistic level. When pursuing quantitative results, extreme care must also be taken. For example, phonons are limited to wavelengths of less than the simulated length within a molecular dynamics simulation (as can be easily tested via SED, listed below). If long wavelengths modes contribute to the thermal property of interest, results are likely to be incorrect. Furthermore, it may be difficult to discern whether size effects are an issue without running unreasonably large simulations. Convergence effects may also cause issues, as highly-harmonic systems (long scattering times) may take a long time to equilibrate.

1.4.1 Lattice Dynamics

Lattice dynamics (LD) consists of finding the analytical solution for the vibrational modes of a system. The eigenvalue problem using the matrix expression shown in the previous section is the fundamental basis of LD, although the eigenmodes of the system are typically solved in 3D and using a more realistic description of the interatomic bonding instead of a simple harmonic spring. Density Functional Theory is capable of calculating the bonding of arbitrary structures and materials and bond types, and is often used in conjunction with LD for predicting phonon behavior. One drawback is that LD is typically performed at zero temperature (i.e., the analytical calculation returns the perfect phonon dispersion based on interatomic forces alone), meaning the interactions of phonon modes within the system at finite temperature may not necessarily be captured.

1.4.2 Molecular Dynamics

In contrast to LD, a molecular dynamics simulation considers a volume of atoms, iterating through a series of timesteps, calculating the instantaneous interatomic forces, and applying the corresponding adjustments to the atomic trajectories at each timestep. This is a strictly numerical simulation of the motion of atoms, which can be computationally demanding, but also extremely versatile. A simulation of two materials with a heat flux applied across them can allow for an “in-simulation measurement” of TBR based on the temperature drop at the interface [38] (this is referred to as “non-equilibrium molecular dynamics, or NEMD). The Green-Kubo formalism [42] uses fluctuation dissipation theorem to evaluate heat flux at equilibrium, and can be used to extract thermal conductivity. Fourier analysis on the velocities of the atoms within the system can return the simulated vibrational density of states (vDOS. Notably, this is not the “phonon” density of states, as amorphous materials can be modeled and non-wavelike vibrations may be present). Similarly, the wavelike nature of the vibrations can be isolated using Spectral Energy Density (SED) [43] analysis. Spectral Heat Flux [44–47] analysis can also be used to find the frequencies of vibrations carrying heat, as opposed to merely the modes which are present (as in vDOS). Modal Analysis [38, 42] methods are also able to provide mode-mode scattering interactions, to determine which frequencies of vibration interact. Note that in classical MD (i.e., using traditional potentials and Newtonian equations of motion) all modes are considered to be populated following the Maxwell–Boltzmann distribution instead of Bose-Einstein.

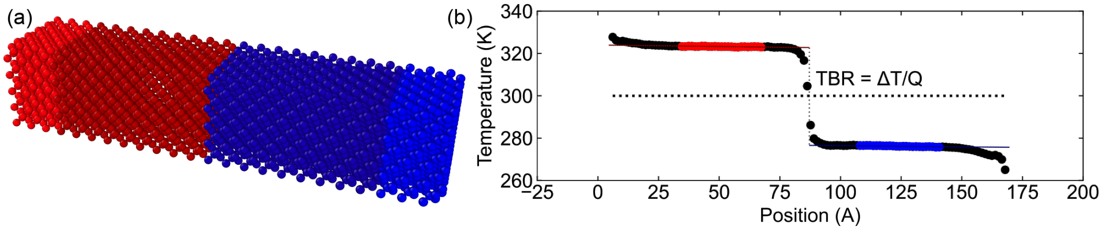

FIGURE 1.5: Within a molecular dynamics simulation, the motion of individual atoms is numerically simulated. In the example shown (a), hot and cool baths are applied to either end of a volume (energy either added or subtracted), and a temperature vs. position profile (b) is extracted. In this case, the temperature drop across the interface is used to find the simulated thermal boundary resistance.

Chapter 2

Measurement uncertainty and systematic error

An understanding of uncertainty and measurement error, including its sources and means of quantification, is critical for understanding what can and cannot be measured. In effect, a measurement technique is only as good as its uncertainty and error, and the ability to accurately characterize these will determine whether inferences can realistically be made from the data. Similarly, accurately characterizing error and uncertainty can prevent the researcher from making erroneous conclusions based on faulty data.

This can be broken down into three distinct concepts: the assumptions required by the analysis (measurement uncertainty), the capabilities and calibration of the experiment itself (systematic error), and randomness (random error). Unfortunately, there remains confusion within the nanoscale thermal metrology community, and no clear standardized way of characterizing uncertainty and error exists. In this chapter, I will explore the sources of uncertainty and error within the thermal measurements we use, and lay out recommendations on how these should be characterized and quantified.

2.1 Propagation of uncertainty

To understand measurement uncertainty, it is necessary to understand the interdependence of multiple thermal parameters within the experiment. For example, consider a measurement of the net thermal resistivity, such as the slope of a SSTR dataset. This measurement will be unable to differentiate between a multi-layer sample with high thermal conductivity and high TBR vs. one with low thermal conductivity and low TBR. Another example would be a measurement of total thermal diffusivity (where thermal diffusivity is the ratio of thermal conductivity and heat capacity, $\alpha = K/C$) which is found in the curvature of the thermal decay in a SPTR dataset. Here, the measurement cannot differentiate between a sample with high K and high C or low K and low C. If one of the interdependent parameters is being assumed in the analysis, then the assumption used for this value (and its uncertainty) will affect the fitted values for the other parameter (termed "measurement uncertainty").

This phenomena is common when films are involved, as changing the thickness of a layer in the sample stack will almost proportionally affect the final fitted conductivity. Similarly, the resistance associated with an interface is often directly interchangeable with the resistance of a film. It is useful to consider the Kapitza lengths associated with thermal interfaces ($l_\mathrm{K} = R_\mathrm{K} \cdot K$), which describes the thickness for which a film would have an equivalent thermal resistance to an interface. For example, a TBR of 5 m^2 K GW^{-1} is equivalent to 0.2 µm of Sapphire (35 W m^{-1} K^{-1}) or 7 nm of an amorphous silicon oxide (a-SiO_2, 1.4 W m^{-1} K^{-1}), meaning even slight uncertainty in the sample thickness and film conductivities can yield large uncertainty associated with a measurement of TBR and vice versa.

There are three ways this effect is typically quantified, and all begin with reasonable assumptions (or measurements) of uncertainty for all input parameters (e.g., layer thicknesses, heat capacities, assumed thermal conductivities, laser spot sizes etc.). In Monte Carlo (MC) analysis, combinations of input parameters are generated based on a normal distribution of each. The fitting is then repeated for each combination, and the standard deviation of the fits is taken as the uncertainty. This is effectively considering a series of "what if" scenarios to explore how potential deviations from each nominal input parameter affects the output (e.g., "what might the real value be if the transducer is slightly thicker than expected").

A simpler (and more computationally efficient) approach is to simply perturb each input parameter individually and refit. I will refer to this as "pseudo-Monte Carlo" or "pseudo-MC". This can be represented mathematically as follows:

$$\sigma = \sqrt{\sum_p \sigma_p^2} \tag{2.1}$$

where σ is the total uncertainty dependent on the deviation of the fitted parameters (σ_p) from input parameter p. Summing squared terms allows combining of effects from each parameter, while those with a negligible contribution (e.g., heat capacity in a measurement where one is insensitive to heat capacity) do not reduce the overall uncertainty.

Note that in both MC and pseudo-MC analysis, we are effectively probing the sensitivity of each fitted parameter to the inputs. The variance-covariance from the experiment can also be computed analytically [48] by calculating the strength of each parameter on each other parameter:

$$\sigma = \sqrt{\sum_p \left[\frac{df}{dp}^2 * s_p^2 \right]} \tag{2.2}$$

where we are interested in the strength of each input parameter p on the output parameter f (i.e., $\frac{df}{dp}$). This affects the degree to which each input parameters' uncertainty s_p contributes to the total uncertainty σ. The expressions are thus the same, as the perturbation of the fitted value as probed by MC or pseudo-MC is effectively:

$$\sigma_p = \frac{df}{dp} * s_p \tag{2.3}$$

In other words, MC is effectively a statistical simulation of the propagation of uncertainty from inputs to the fitted result(s), but is otherwise mathematically comparable. While pseudo-MC does not capture the permutations across the normal distributions of each parameter, it tends to yield similar results, and is typically sufficient.

When analyzing uncertainty in either manner, it is also worth considering independent vs. dependent parameters. In SSTR, a slope scaling term (γ) is calculated from a known reference sample (known thermal properties, identical transducer), in order to account for numerous unknown experimental scaling parameters (e.g., thermoreflectance coefficient, photodetector sensitivity, and optical losses through lenses and mirrors). Since γ is found from a known reference sample, the uncertainty in γ is dependent on the uncertainty in other parameters (e.g., the thickness of the transducer deposited on both the reference sample and sample of interest). It is also common to use four-point probe electrical resistivity measurements to infer the transducer thermal conductivity via the Wiedemann-Franz equation, meaning uncertainty in the transducer thermal conductivity may be directly dependent on the uncertainty in the transducer thickness. In some situations, treating these as independent parameters may overestimate the uncertainty.

Similarly, the shared propagation of uncertainty across a set of measurements may influence whether or not claims can be made on trends. Thinking of MC and pseudo-MC as exploration of "what if" scenarios, if an input parameter affects multiple samples in a series equally, it should not prevent one from establishing a trend. For example, if multiple films are grown on substrates from the same wafer, then uncertainty in the thermal conductivity of the substrate is likely to merely shift the resulting values from each sample up or down. Applying the perturbation to each sample identically will likely find the trend maintained. Extreme caution must be taken before neglecting parameters based on this argument however. If measurements are collected on the same day, one might argue that the spot sizes should be identical. If the focusing of the pump and probe beams are set manually however (e.g., by adjusting the sample position by hand while monitoring the focused spot size in a camera), there may still be variability across measurements.

2.2 Relationship between multiple fitted parameters

When multiple parameters are fitted simultaneously, the effects of their interdependence must also be considered (termed “multicollinearity” in the field of regression analysis; this is a form of systematic error). In the most basic example, one can consider a single SSTR dataset, where the slope is the only meaningful piece of information. For two fitting parameters, infinitely many combinations of values will achieve an identical fit to the data. This is fundamentally similar to problems of overfitting, where too many free parameters can yield to unphysical results despite close fits between model and data. Interestingly, the use of machine learning algorithms in place of traditional least-squares curve-fitting [49] does not alleviate this problem, as the measurement itself fundamentally might not be able to discern between different resistances. This phenomena exists in all experiments, however the interdependence of the fitting parameters (and thus the ability of the experiment to measure multiple parameters) is often non-obvious. For this reason, I recommend that contour analysis be used to explore this effect.

In contour analysis, many permutations of the fitted parameters are tested against the data (model curve generated, residual between model and data calculated). For 2 fitting parameters, the residual as a function of both parameters can be visualized as a contour plot, with pairs of values providing a similar quality of fit enclosed in a contour. All combinations of parameters which yield a satisfactory fit (residual below a chosen threshold) are candidate solutions to the dataset, meaning the extent of the given contour indicates the measurement error.

I have included an example of TDTR data on an 80 nm aluminum / bulk sapphire sample stack in Fig. 2.1 below. Two unknowns might be the aluminum / sapphire TBR, and the sapphire thermal conductivity, both of which are forms of thermal resistance, and some interdependence between these parameters should be expected. I have prepared synthetic (noiseless) data for this sample stack, in order to avoid conflating systematic effects (what the experiment is fundamentally capable of measuring) vs. the effects of noise.

In Fig. 2.1.a, the fitted Monte Carlo K_{Sapphire} and $\text{R}_{\text{Al/Sapphire}}$ values are shown for many perturbations of input parameters. The color of each point denotes the quality of fit, suggesting that some permutations of deviated input values will yield poor fits (e.g., no good fit might be found if 75 nm aluminum thickness is used). This is compared to contour analysis, where the quality of fit across many combinations of K_{Sapphire} and $\text{R}_{\text{Al/Sapphire}}$ is presented as a contour (with no deviations applied to the other input parameters). A region of the K_{Sapphire}, $\text{R}_{\text{Al/Sapphire}}$ parameter space yielding a given quality of fit is enclosed in a contour, and the extent of the contour denotes the systematic error associated with that quality of fit. Differing trends (e.g., the slope of the resulting ellipse) is evidence that MC and contour analysis are testing fundamentally-different phenomena (and that the propagation of uncertainty from input parameters is fundamentally different from the capabilities of a given measurement).

For 2 fitting parameters, the interdependence of fitting parameters can be visualized via contours, however for 3 or more parameters, visualizing the parameter space becomes difficult. Similarly, probing the entire 3D+ parameter space may be extremely computationally inefficient (e.g., $O(n^N)$ computation time for n points in parameter space across each of N dimensions). Instead, a 2D contour plot can be generated by sweeping through pairs of values for two parameters (or 1D, sweeping through a range of values for 1 parameter), fitting for the remaining additional parameter(s) at each location, and recording the residual of the best fit. This is shown in Fig. 2.1.b, where I sweep through values of K_{Sapphire} and fit for $\text{R}_{\text{Al/Sapphire}}$, plotting the residual of the best fit. This is equivalent to a line-scan across the 2D parameter space (dotted red curve: Fig. 2.1.a).

I have not yet commented on what quality of fit one should accept, and numerous researchers have suggested varying values. Typical threshold values range from 1% to 3%, [25, 50] using the residual expression from Feser *et al.* below:

$$residual = \sqrt{\frac{\sum_i [F_i - D_i]^2}{\sum_i F_i^2}} \tag{2.4}$$

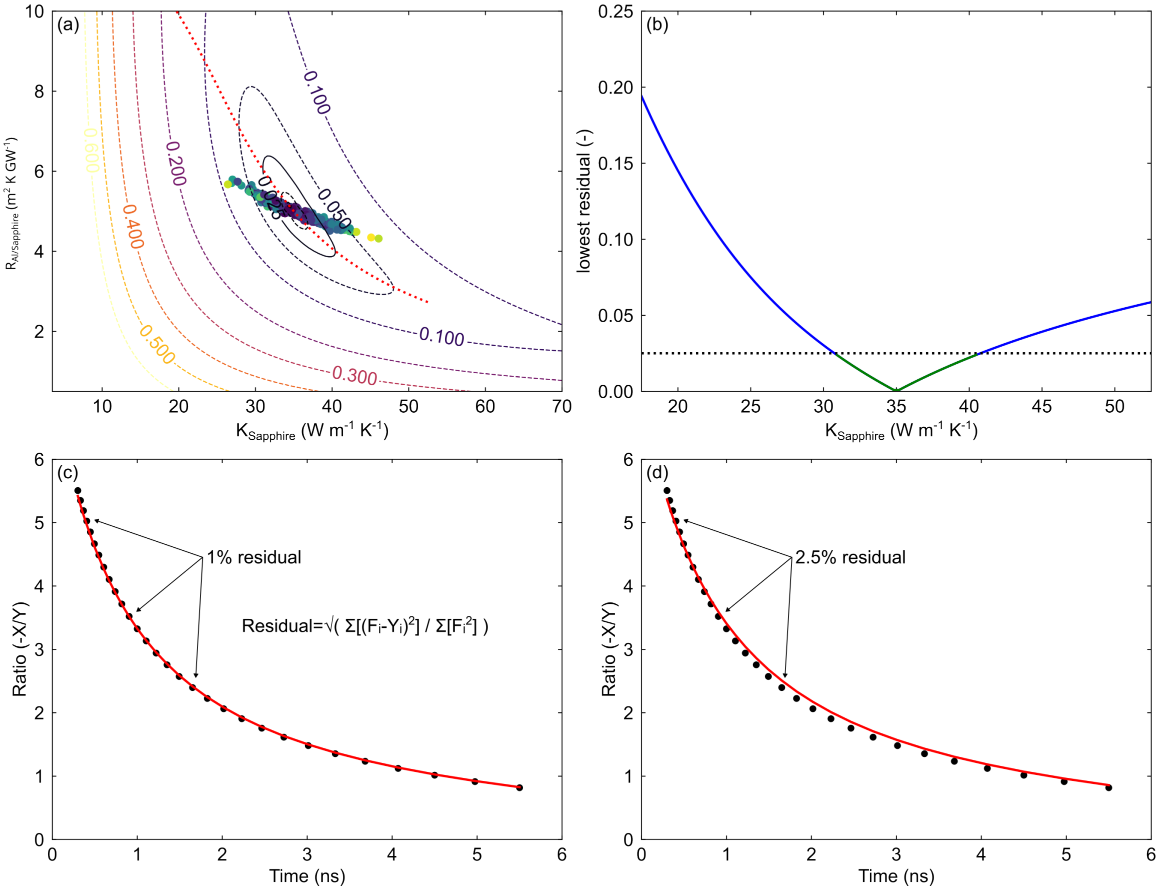

FIGURE 2.1: To compare contour vs. Monte Carlo analysis, I consider TDTR measurements of an Al/Sapphire stack, fitting for K_{Sapphire} and $\mathrm{R}_{\text{Al/Sapphire}}$. (a) 2D contour analysis (dashed ellipses) and Monte Carlo (multicolor dots) yield slightly different results. These are testing fundamentally-different sources of error (Monte Carlo captures propagation of uncertainty from assumed parameters, while contour analysis captures systematic error, e.g., laser misalignment). (b) 1D contour analysis can also be performed, by sweeping through a range of values for one parameter, fitting the remaining parameter(s), and checking the best fits' residual. This is effectively a sweep through the parameter space seen in the 2D contour (red dotted curve in (a)). Example curves (c,d) showing 1% and 2.5% residuals.

where the data points D_i and corresponding points in the model function F_i are compared. This is a slightly different expression from mean-squared error (MSE) in that the result does not depend on the length or scaling of the dataset.

Some have suggested basing this on the noise level within the data (i.e., extremely clean data will allow acceptance of a lower residual, thus reducing one's claimed error). In the following section I will discuss a less-arbitrary means of selecting the residual value. In the mean time however, I have shown the 1% and 2.5% residual to the synthetic data in Fig. 2.1.c-d.

2.3 Apparatus misalignment

It is important to recognize the role of systematic errors originating from the measurement apparatus, as poor system alignment will yield datasets with incorrect trends, yielding inaccurate fits. For example, misalignment of the pump/probe spots by a fraction of a micrometer can easily change the slope of an SSTR measurement by more than 1% (example below in Fig. 2.2). Similarly, misalignment down a TDTR delay stage can cause a shifting of pump or probe beams or a change in focused radii, yielding a decay curve with an incorrect slope (as was highlighted by the inventor of TDTR in the original work [15]). This misalignment-induced offset applied to the data will then yield incorrect results when fitting is performed. Note that the sensitivity to the fitted parameter(s) loosely determines the influence of these systematic errors on the fitted result. If one is attempting to measure a parameter for which the experiment has low sensitivity (i.e., the parameter has little effect on the model or data), the fitting algorithm will need to adjust the parameter quite far in order to "correct" the systematic deviation in the data originating from experimental apparatus misalignment. This means the fitted value may be quite far from the material property's true value. Conversely, for the hypothetical perfect measurement system (which does not exist), there would be no reason to accept anything but a perfect fit, despite potentially low sensitivity to a given parameter.

One's confidence in the alignment of their measurement system thus has a bearing on the confidence in the result, and the rigor with which the system was calibrated determines the confidence in the alignment. I can thus establish guidelines on selection of a contour threshold, based on considerations of the calibration procedure used. Just as MC and pseudo-MC analysis are asking the question "what might the solution be if the input parameters are slightly off", contour analysis is exploring "what might the solution be if the data is slightly off for some uncaught systematic reason". It is common practice to validate a measurement system by measuring a (series of) known calibration sample(s) and confirming that the correct value(s) are found. This means the range of acceptable calibration values and corresponding changes in the model's curve can be used to guide selection of the contour threshold. For an SSTR measurement on an Al / a-SiO_2 system, changing the thermal conductivity of the SiO_2 by 4% will yield a 1% residual. This means if one accepts a fitted SiO_2 conductivity of 1.35-1.45 W m^{-1} K^{-1} during calibrations of their SSTR system (from nominally 1.4 W m^{-1} K^{-1}), then a 1% residual may suffice. In contrast, for a TDTR measurement on Al / Sapphire, a 3% change in the sapphire conductivity yields a 2.1% residual (a range of 33-35 W m^{-1} K^{-1} from a nominal 34 W m^{-1} K^{-1}). This suggests sapphire calibrations alone are unlikely to capture all systematic misalignment errors. The selection of calibration sample thus partially determines the uncaught systematic errors which may exist (and the use of as many as is feasible is recommended). Note that the level of noise in a measurement (or lack thereof) may have little to do with the alignment and calibration of a system, so a low threshold should not be used solely based on the level of noise in the experiment. These deviations can be seen on synthetic datasets in Figure 2.2.

Since contour analysis is intended as a measurement of the interdependence of fitted parameters and the capabilities of a given measurement system, a minor modification is the use of synthetic data in the analysis (as opposed to using real data resulting from a measurement). A noisy dataset (with a higher residual despite being an otherwise accurate fit) should not serve to *reduce* the claimed error associated with a measurement. Instead, if syn-

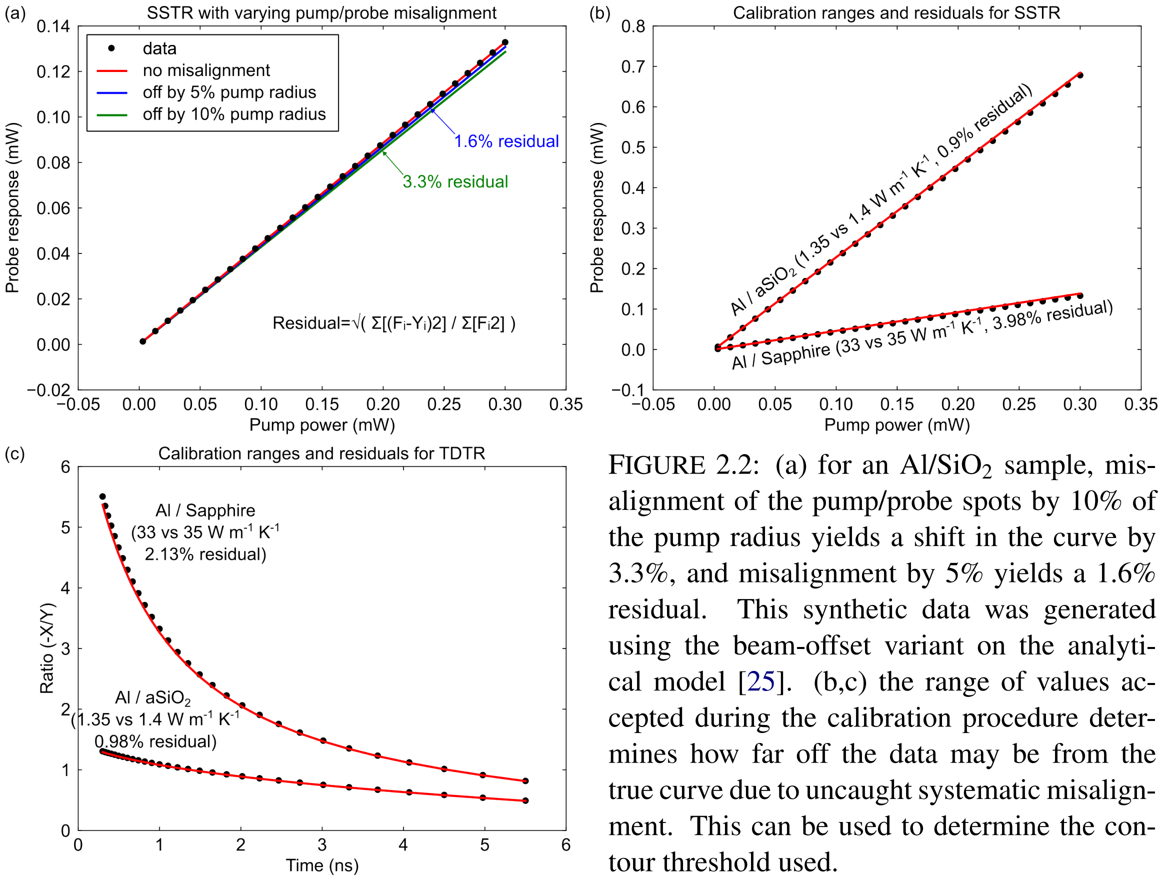

FIGURE 2.2: (a) for an Al/SiO$_2$ sample, misalignment of the pump/probe spots by 10% of the pump radius yields a shift in the curve by 3.3%, and misalignment by 5% yields a 1.6% residual. This synthetic data was generated using the beam-offset variant on the analytical model [25]. (b,c) the range of values accepted during the calibration procedure determines how far off the data may be from the true curve due to uncaught systematic misalignment. This can be used to determine the contour threshold used.

thetic data with zero noise is used for contour analysis, then a more realistic determination of the capabilities of a given measurement will be found (system noise aside).

The relationship between the size of a given parameter's contours and the parameter's sensitivity also minimizes the need for sensitivity analysis. If a measurement is insensitive to a parameter, a large range of values for that parameter may yield a satisfactory fit to the data, and the contours will be large. Sensitivity analysis is typically performed by perturbing a parameter in the model and comparing the resultant curve to the unperturbed model, however it may be difficult to infer from this whether additional parameters can be fitted. Conversely, generating contour plots for a hypothetical scenario means the experimental error can be predicted directly. Furthermore, the benefit (or lack thereof) of alternative analysis schemes (e.g., multi-frequency TDTR or ratio/magnitude fitting of TDTR data) becomes apparent. When two contours (e.g., contours for TDTR at multiple frequencies) are overlapped, only the region shared by both contours yields a satisfactory fit to both datasets [25, 30–33]. In other words, by taking the boolean intersection of multiple contours, a reduction in overall contour bounds may be found. One can perform this analysis prior to the collection of data; by checking the overlapping of contours of multiple prospective measurements, it should become immediately clear if the additional measurements help in reducing the contour bounds. Examples of this overlapping of contours will be shown in later chapters as well.

Understanding contour analysis as a form of "what if" analysis relating to uncaught systematic apparatus errors, we may be able to loosen the restrictions slightly, as we did when considering the propagation of uncertainty. If all measurements within a series are collected on the same day, it may be reasonable to neglect contour analysis when establishing a trend. In other words, systematic apparatus errors (e.g., incorrect slope of TDTR thermal decay curve due to a slight delay stage misalignment) may cause a systematic shift in the data (all fitted thermal conductivity values being slightly too high). This will introduce error into the nominally fitted values, but should not prevent establishing trends or comparison between samples. While this concept has not been rigorously developed as far as I am aware, numerous authors have resorted to qualitative comparison of raw data (simply comparing the slope of a thermal decay or magnitude of a signal) to justify trends. This form of comparison is fundamentally similar, however an understanding of why this may or may not be valid is crucial (e.g., data collected on different days with different alignment, or different systems).

2.4 Failure of Monte Carlo as a stand-in for determining systematic error

In the aluminum / sapphire example, the uncertainty from MC and systematic error from contour analysis yielded similar bounds despite showing different trends. This is not always the case however, since the fundamental sources of error/uncertainty are different. While Monte Carlo captures uncertainty in the end result originating from uncertainty associated with the input values, contour analysis considers the interdependence of the fitted parameters with regard to each other ("multicollinearity"), and the ability (or inability) of the measurement to discern multiple parameters simultaneously.

To demonstrate this concept, I have evaluated the hypothetical measurement of a buried interface (Al / Si / Ge) as semiconductor-semiconductor TBRs are highly relevant in semiconductor device design and manufacturing. Due to surface roughness and cleanliness effects and due to variations in transducer deposition, the transducer / film TBR ($R_{\mathrm{Al/Si}}$) should not be assumed. Similarly, size and crystal quality effects may yield unexpected film thermal conductivities (K_{Si}), so this parameter should also be fitted. Given the final film / substrate TBR ($R_{\mathrm{Si/Ge}}$) as our parameter of interest, we are thus left with 3 fitting parameters ($R_{\mathrm{Al/Si}}$, K_{Si}, and $R_{\mathrm{Si/Ge}}$).

Three unknown parameters means contour analysis must be performed over a 3D parameter space. This can be visualized in 3D (Fig. 2.3.a, inset), or collapsed along a given axis (Fig. 2.3.a, outset). The bounds on the contour region for a chosen threshold denote the combinations of parameters which yield the corresponding quality of fit, which yields the error due to multicollinearity and systematic issues / misalignment. Practically, If one is only interested in $R_{\mathrm{Si/Ge}}$, a sweep through values of $R_{\mathrm{Si/Ge}}$ and fitting for $R_{\mathrm{Al/Si}}$ and K_{Si} at each point can be used to establish bounds for $R_{\mathrm{Si/Ge}}$ (Fig. 2.3.b).

I also repeat this analysis (performing both contour and Monte Carlo analysis) for multiple measurements types and variants (Fig. 2.3.b). In nearly all cases, Monte Carlo analysis underestimates the total error. In some cases, the contour analysis suggests $R_{\mathrm{Si/Ge}}$ cannot be measured, as an arbitrary value for this parameter will yield a good fit if appropriate corresponding values for K_{Si} and $R_{\mathrm{Al/Si}}$ are used. Interestingly, each experiment also has differing contributions from contour analysis and Monte Carlo. This means that one's ability to characterize all input parameters (contributing to Monte Carlo) or the level to which one calibrates their apparatus (contributing to contours) can be used to guide selection of

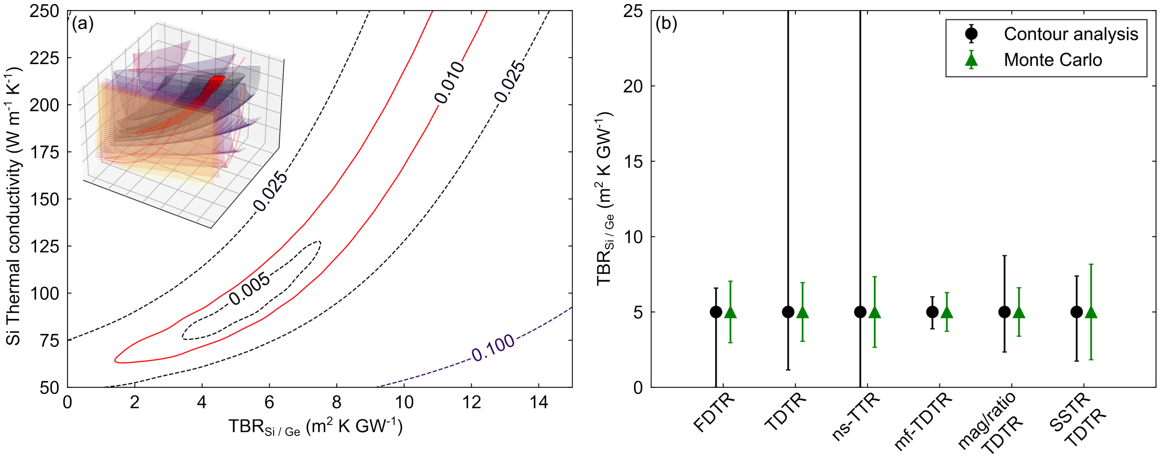

FIGURE 2.3: (a) Considering the hypothetical measurement of the Si/Ge interface ($R_{\mathrm{Si/Ge}}$) within an Al/Si/Ge stack, three unknown parameters means contour analysis must be performed over a 3D parameter space. This can be visualized in 3D (inset, axes are $R_{\mathrm{Al/Si}}$, K_{Si}, $R_{\mathrm{Si/Ge}}$, intended for visualization purposes only), or collapsed along a given axis (outset). For a given quality of fit threshold, the bounds on the corresponding contour region denote the combinations of parameters yielding an acceptable fit between model and data. This is a measure of the error due to multicollinearity and systematic issues / misalignment. (b) I performed contour and Monte Carlo analysis on synthetic data for multiple measurements types and variants. In nearly all cases, Monte Carlo analysis underestimates the total error, and in some cases the $R_{\mathrm{Si/Ge}}$ contour error is unbounded (i.e., an arbitrary value will yield a good fit if K_{Si} and $R_{\mathrm{Al/Si}}$ are adjusted accordingly).

the experiment. Reviewing the literature for measurements on buried interfaces [23, 50–61], the uncertainty reported is likely artificially low in many cases, due to incomplete uncertainty quantification. In other cases, the authors took great care to capture error from various sources, and found they needed to develop new measurement techniques or modify existing ones in order to adequately characterize the interface. This includes measurement at multiple modulation frequencies or with multiple spot sizes [51, 53–55] or fitting of multiple data types [50], development of transducerless measurements [56, 61], the use of unique sample geometries [53] or experimental configurations [23]. In some cases, high TBR values are simply easier to measure (as compared to the aforementioned Al / Si / Ge example), as the experiments tend to be most sensitive to the highest resistance within the system.

2.5 Influence of sample variation and noise

Finally, variation between samples or between data points within a dataset also warrants consideration. It is common to simply calculate a standard deviation across multiple measurements, however it is important to recognize that this does not capture any the above sources of uncertainty or error. Instead, this simply captures the random variation across the sample, across multiple samples, or noise within a given experimental apparatus. This is still important, as some growth or sample preparation techniques may produce highly-variable samples, and understanding the repeatability of an experiment is critical. Each method should be used: Monte Carlo (or pseudo-Monte Carlo, to characterize the propagation of uncertainty), contour analysis (exploring the interdependence of multiple fitted parameters, or "multicollinearity", and exploring the possibility of uncaught systematic apparatus error), and the standard deviation across measurements (capturing random variations). The total error can then be found via the root mean sum (ensuring that a low error from one source does not serve to reduce the overall error).

2.6 Relevant publications

It is exceptionally rare to find works in the thermal measurement community which have characterized all uncertainty and error, and many in the community appear to misunderstand the sources of uncertainty and error. In an effort to correct this, I spent a significant portion of our review article outlining the necessity and intricacies of uncertainty and error quantification. This work was recently accepted in Annual Review of Materials Science. (T. W. Pfeifer, H. B. Schonfeld, H. T. Aller, E. A. Scott, J. T. Gaskins, D. H. Olson, J. Braun, S. Graham, P. E. Hopkins "Limitations and Advances in Optical Thermometry: Nanoscale Resistances, High Thermal Conductivity Materials, and Ultrahigh Temperatures", Recently accepted: Annual Review of Materials Science).

Chapter 3

Measurement of depth-varying thermal conductivity

The analytical model used for fitting thermoreflectance data is based on the solution to the cylindrical heat equation for individual homogeneous layers [15]. Multiple layers can be modeled by linking the bottom temperature of a given layer to the upper surface temperature of the subsequent layer, and similarly asserting that the heat flux exiting the bottom of a layer is equal to the heat flux entering the top of the subsequent layer. This means the model can be applied to a sample composed of arbitrarily many layers, however the layers within the model (and thus the sample) must be effectively homogenous within the measured volume. Some approximations can also be made depending on the sensitivity of the features under consideration: ultra-thin films (< 10 nm) are often treated as interfaces for example [62–64], and superlattices are almost never fitted as dozens of discrete layers, but rather the effective conductivity of the aggregate is considered [65–67]. This means complex sample stacks can be modeled (and thus, measured), with the aforementioned thermoreflectance techniques being used for everything from bulk materials to thin films to superlattices.

3.1 Effects of ion irradiation on thermal properties

In the case of ion irradiated materials, chemical disorder (induced by the implantation of ions) and structural disorder (induced by the passage of ions) can vary by multiple orders of magnitude within the first tens of nanometers to microns of the sample surface [68–75]. This disorder can affect the thermal properties, meaning the thermal properties will also vary within this region [69–71, 76–80].

Despite this problem, the thermal properties of irradiated materials are of great interest both practically (e.g., in the thermal regulation of nuclear reactors [77, 81]) and scientifically (e.g., in gaining a fuller understanding of the effects of structural and chemical defects on thermal conductivity or thermal boundary resistance [69–71, 80, 82]). The properties of irradiated semiconductors specifically are also of interest, as ion irradiation is used in a variety of semiconductor manufacturing processes, from doping to film lift-off [83]. For this reason, I performed a study over a series of silicon samples which had been irradiated with krypton ions. Samples were irradiated with varying doses (10^8-10^{14} ions cm^{-2}) with an energy sufficient to deposit ions $\sim$ 300 nm below the surface (500 keV, predicted via the Stopping Ranges of Ions in Matter (SRIM) [68] software). The aluminum transducers required by thermoreflectance experiments were deposited following irradiation. TDTR has a measurement depth in silicon of $\sim$ 1 μm, meaning the ion concentration and level of disorder varies by several orders of magnitude within the measured volume. Similarly, the depth range over which this damage occurs is on the order of hundreds of nanometers, meaning it would not be appropriate to treat the irradiated region as a separate discrete layer as in the work of Scott *et al.* [79].

3.2 Modifications to the thermal model

As part of the first thrust for my dissertation ("Development of new analysis methodologies for existing measurement techniques"), and in order to address the limitation from the continuously spatially-varying samples, I developed a modification to the fitting procedure for TDTR data. I discretized the sample into numerous finite-thickness layers, and applied a spatially-varying function for the thermal conductivity. I began with the assumption that the resultant defect profile should be approximately Gaussian, which has been observed previously [83–92]. I then assumed that the defect concentration will be inversely proportional to the thermal conductivity, since scattering from irradiation-induced point defects should follow Matthiessen's rule [69]. Matthiessen's rule allows for the summing different types of phonon scattering [3–5], where the effects of varying scattering mechanisms can be estimated as follows:

$$\tau_{total}^{-1} = \tau_{pp}^{-1} + \tau_{boundaries}^{-1} + \tau_{defects}^{-1} + \ldots$$

This means sources of resistivity are additive (inherent from phonon-phonon scattering, added resistivity from defects, etc). By then assuming $\tau_{defects}^{-1}$ is proportional to the defect concentration, a Gaussian defect profile will yield a Gaussian resistivity profile following:

$$R(z) = R_{\text{pristine}} + R_{\text{min}}\, e^{-\dfrac{(z - z_{\text{center}})^2}{2 * w^2}} \tag{3.1}$$

$$K(z) = \frac{1}{\dfrac{1}{K_{\text{pristine}}} + R_{\text{min}}\, e^{\dfrac{(z - z_{\text{center}})^2}{2 * w^2}}} \tag{3.2}$$

This thermal conductivity profile was thus defined by the constants R_{min} (thermal resistivity at its maximum), z_{center} (the location of this maximum), and w (the through-plane spread). This allowed fitting of these individual constants and avoided the need to fit the conductivity of each discretized layer individually. A schematic of this is shown in Figure 3.1 below, showing the ion penetration and sub-surface defected region, along with the discretization of the sample geometry into many layers.

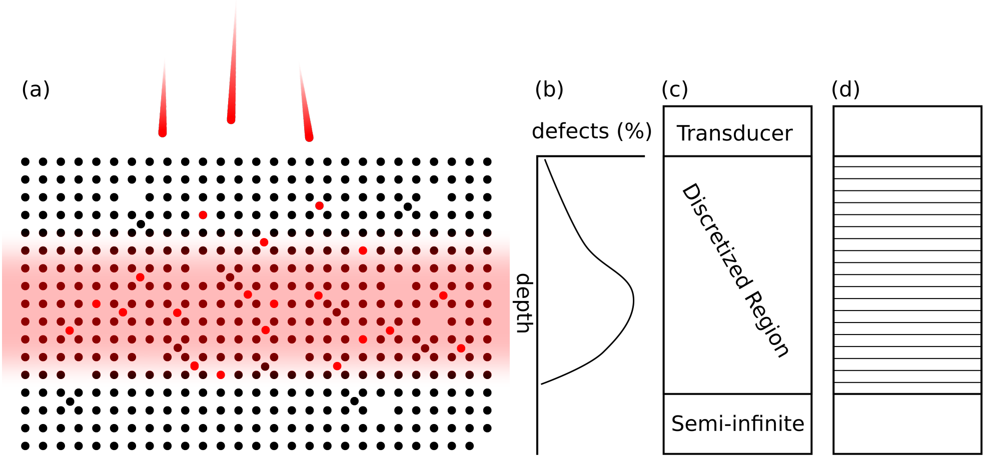

FIGURE 3.1: (a) Schematic of atomic-level defects that arise due to ion bombardment. The host material (black) ends up with voids and self-interstitials, and the ions (red) form interstitial and substitutional defects. There is a gradient of damage (red), centered some depth below the surface. The resulting continuously varying damage profile (b) is modeled by taking a conventional three-layer thermal model (c), discretizing the intermediate layer (d), and fitting for a function for thermal conductivity.

3.3 Circumventing issues of measurement error

This was my initial real-world encounter with the issues of measurement error discussed previously, as TDTR is typically only able to accurately fit 2-3 unknown parameters. If too many unknowns are left free, overfitting issues may arise; a given parameter can be set to nearly any value and adjustments to the remaining parameters can still yield a good fit to the data.

For these irradiated samples, the Gaussian function alone presented 3 unknowns, and the aluminum / silicon TBR was also not known. Since the TDTR modulation frequency is linked to the measured depth within the sample however [21], I collected TDTR data at numerous frequencies, each with differing sensitivities to various portions of the depth-varying thermal conductivity. For two unknown parameters, a 2D contour plot can be used to visualize the interdependence of the parameters, and for 3 parameters, a 3D contour volume can be considered. There is no easy way to visualize the 4D parameter space, so I instead performed a 1D sweep through each parameter independently (fitting for the remaining 3 and recording the best fit residual) to assess error. For the sake of visualization and to observe the benefit of the multi-frequency fitting, I also generated 3D contours (fixing the aluminum / silicon TBR) for each TDTR modulation frequency (Figure 3.2.a-c below). It has been shown for 2D contour analysis that reduced error can be found by taking the boolean intersection across multiple datasets' contours [25, 30–33], since this represents the combinations of fitting values which satisfy all datasets. Stated in the inverse, there may be sets of fitted values which yield a satisfactory fit for one dataset but not another, and these sets of values should not be considered as plausible solutions. This is extendable to 3D as well, where the boolean intersection between 3D contour volumes can be calculated. This is shown in Figure 3.2.d below. While there were relatively large ranges of values for the 3 Gaussian parameters which yielded a satisfactory fit to one-frequency TDTR dataset, only a small subset of these satisfy the data across all frequencies. This approach will continue to be relevant for subsequent projects as well.

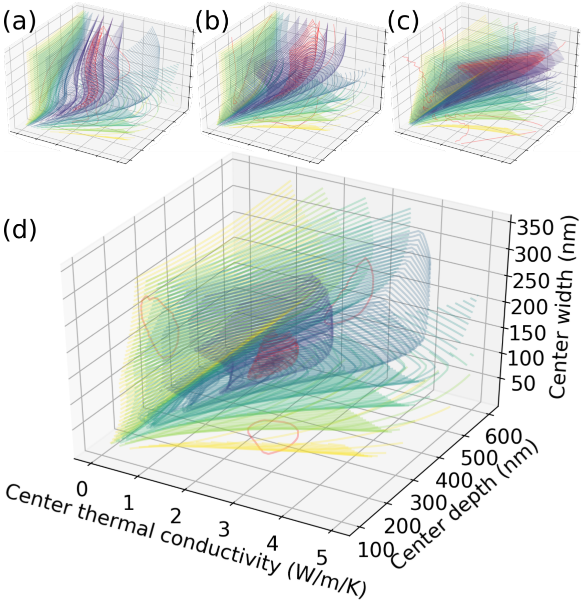

FIGURE 3.2: for 3 unknown fitting parameters, a 3D parameter space is mapped out, with given levels of quality of fit represented as surfaces. This is done for TDTR scans at each modulation frequency (a-c, axes identical to those in d). As these are intended for visualization purposes only, the three axes (gaussian center position, resistivity at the minimum, and gaussian spreading) are left off. By finding the intersection of these 3 volumes however (d), smaller uncertainty is found (beyond what any individual TDTR scan is capable of finding). Note that for true rigorous uncertainty, this analysis should be done in 4D (including the Al/Silicon TBR), or the "collapsed" procedure can be performed (for a single parameter, sweep through a range of values, and perform fitting of the remaining three).

3.4 Results and findings

The fitted Gaussian thermal conductivity profile results for the 10^{14} ions cm^{-1} sample can be seen in Figure 3.3.a, with 2.5% residual and 1% residual threshold bounds shown in shaded gray and pink respectively. All samples showed a similar profile, with varying scaling in thermal conductivity. In the previous section, I discussed basing the contour threshold on the calibration procedure used. A 2.5% threshold is common however, so I presented the data using this more-conservative 2.5% threshold and the more-appropriate 1% threshold.

Notably, the thermal conductivity profile is in qualitative agreement with the irradiation damage and ion insertion profiles predicted via the Stopping Ranges of Ions in Matter simulation package [68]. Pairing the non-destructive thermoreflectance measurements with transmission electron microscopy (TEM), I was able to confirm the presence of a damaged region which qualitatively lined up with the thermal profile measured (Fig. 3.3.b). Selected-area diffraction images also confirmed the (partial) preservation of crystallinity even in this maximally-defected region (Fig. 3.3.d-e).

Looking closer at the area of lowest thermal conductivity, high-resolution TEM showed that the region was composed of amorphous pockets surrounded by a crystalline matrix (Fig. 3.4). The thermal conductivity at this minimum point was measured to be 2.46 ± 0.7 W m^{-1} K^{-1}. In an effort to fully understand how the irradiation affected the thermal properties within this region, I turned to models for analyzing thermal properties within nanoparticle/matrix composites. Within the Effective Medium Approximation model (EMA) [93], the effective thermal conductivity of a composite can be calculated, based on the thermal conductivity of the particles (amorphous silicon in this case) and surrounding material (defected crystalline silicon) and thermal boundary resistance between them. This model also captures the effects of boundary scattering due to the confinement of phonons within the matrix and particles. By using the measured thermal conductivity as the total effective conductivity (2.46 W m^{-1} K^{-1}), approximating the nanoparticle size and density from TEM

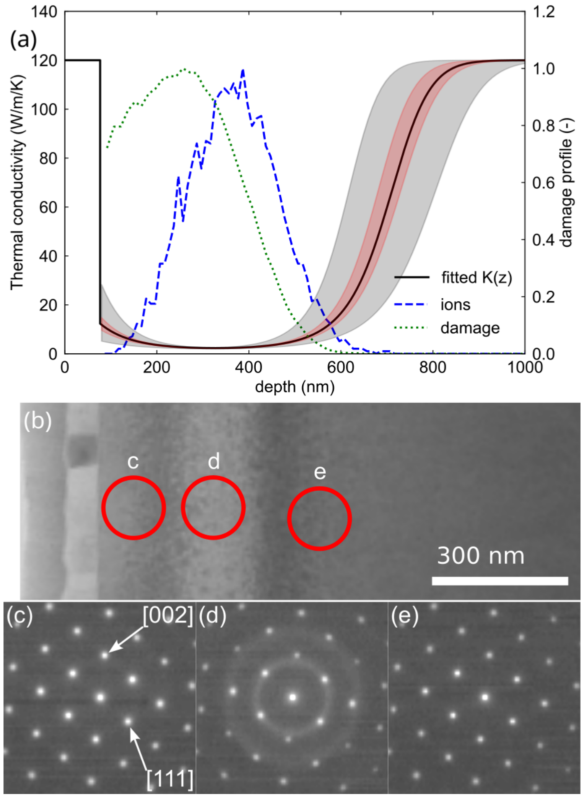

Figure 3.3: TDTR was used to fit a Gaussian function for the spatially-varying thermal conductivity profile (a, black), which qualitatively agrees with the profiles predicted from SRIM (a, blue/green). The range of fitted depth-profiles based on contour analysis are shown for a strict 1% residual (pink) and a looser 2.5% residual (gray). Results were also compared against TEM (b), where a damaged region is visible centered at the point where the lowest conductivity was measured. Selected-area diffraction images (c-e) also provided insight into the structure at various regions. Rings of intensity are seen at intermediate locations, indicating the presence of amorphous silicon, however the crystalline diffraction pattern is seen everywhere, indicating that some degree of crystallinity is preserved throughout the structure. Bragg reflections are labeled for Silicon viewed in [110] in panel (c); note that the forbidden [002] reflection is present, likely due to thickness effects.

images (5-15 nm, and $<$ 30%), and making reasonable assumptions for the a-Si/c-Si TBR and a-Si thermal conductivity, I could thus establish an upper bound on the crystalline silicon thermal conductivity. I estimated the disordered crystalline thermal conductivity to be not more than 10 W m^{-1} K^{-1}, which represents the lowest measurement of disordered (yet still crystalline) silicon to my knowledge.

Understanding why this disordered but crystalline silicon thermal conductivity was so low is also worth exploring. Interestingly, neither mass nor bonding effects should be capable of reducing the thermal conductivity of crystalline silicon to 10 W m^{-1} K^{-1}. Importantly, the effects of boundary scattering were already included by the Effective Medium Approximation. Despite the confined foam-like structure of the crystalline silicon, I could not attribute the 10 W m^{-1} K^{-1} to the nanostructuring. Each of these will be discussed more in depth here.

Mass scattering follows:

$$\Gamma = \sum_i c \left(\frac{\Delta m}{m}\right)^2 \tag{3.3}$$

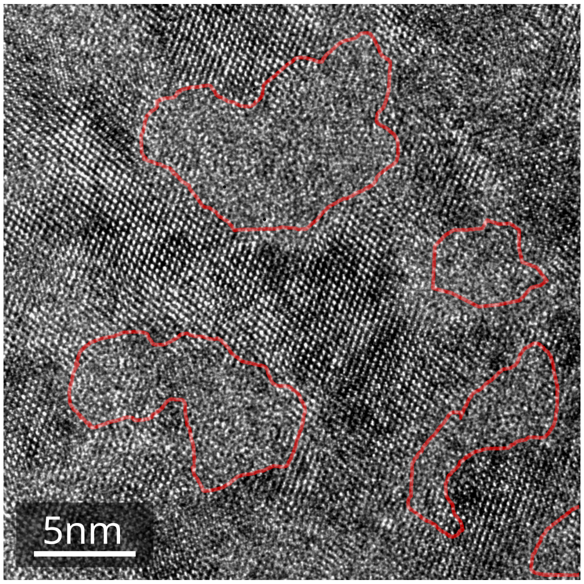

FIGURE 3.4: high-resolution transmission electron microscopy images across the defected sample reveal pockets of amorphous silicon interspersed within crystalline silicon. My thermal measurements represents a first-of-its-kind measurement of a silicon-silicon nanoparticle system. The TEM images in this study were collected by Professor Mark Goorsky at UCLA.

where the scattering rates scale with the square of the mass difference Δm and proportionally to the concentration c [94]. While the mass difference between silicon (28.0855 g mol^{-1}) and krypton (83.798 g mol^{-1}) is high, the concentration of Kr^{+} ions at the highest dose (10^{14} ions cm^{-2}) is still only predicted to be around 0.04% (atomic percent). Lacking a comprehensive study on the thermal effects of alloying of silicon and krypton specifically, I instead turned to literature on the well-studied alloying of silicon and germanium (72.64 g mol^{-1}). In Si-Ge systems studied both experimentally [95] and computationally [96], tenths [95] or hundredths [97, 98] of a percent concentrations of Ge still yielded thermal conductivities above 100 W m^{-1} K^{-1}. Despite the slight increase in mass between krypton and germanium, the ion concentrations in these samples were still extremely low, and I rejected the notion that mass effects could play a significant role in reducing the thermal conductivity of the crystalline regions to 10 W m^{-1} K^{-1} or less.

One might also consider the effects of bond strength, where the bonding between Si-Si or Si-Ge atom pairs is expected to be significantly stronger than the interactions between Si and Kr (a noble gas). Ratsifaritana and Klemens [99] considered the removal of atomic linkages due to vacancies as being equivalent to a point defect with a factor of 2 mass difference. Following the expression from Eq. 3.3, this can be taken as an extreme lower limit for the weakened bonding between silicon and krypton. Even considering this extreme limit, concentrations must be on the order of 1% in order to achieve a thermal conductivity reduction to 10 W m^{-1} K^{-1} [100]. It again appeared that significantly higher ion concentrations would be required in order to attribute the thermal conductivity reductions to these effects.

I next considered the influence of damage to the crystalline lattice structure as induced by displacements and/or cascades due to bombardment. SRIM predicted up to 40% of atoms could be dislocated as a product of irradiation, however this should be taken as an upper bound due to the possibility of recombination of self-interstitials and vacancies during the bombardment process. Furthermore, a level of 30% structural damage can be taken as the threshold for the amorphization of crystalline silicon [73]. Taking the effects of mass point defects as an approximate analogy, and without going into depth as to the specific types of structural defects present, I noted that a 30% concentration of point defects could lead to a thermal conductivity as low as 5 W m^{-1} K^{-1} for bulk. This effect is far more significant than either mass or bond-strength scattering effects alone, as the passage of each individual ion can introduce far more structural disorder than would result from the mere presence of the ion itself. Numerous prior studies have also made similar observations. For example, post-annealed ion-bombarded samples have seen a near-complete restoration of high thermal conductivity [70]. Similarly, studies in which the ion and target were the same material (e.g., silicon bombarded with silicon [69] or diamond bombarded with carbon [71]) have seen large reductions in thermal conductivity, despite the negligible mass difference between ion and target material.

I thus attributed the extreme reduction in silicon thermal conductivity to both structural defect scattering (from 120 W m^{-1} K^{-1} down to 10 or below for the crystalline regions) and interface scattering effects between the crystalline and amorphous regions (from 10 or less down to our measured 2.46 W m^{-1} K^{-1}). While exploring the EMA model, I also found insensitivity to TBR in this regime. This suggests interfacial scattering dominates rather than heat exchange between host and nanoparticles. I also rejected the notion that mass-scattering or differences due to the effect of Si-Kr bond strength play a significant role in the measured thermal conductivity reduction, based on the low concentration of krypton ions predicted.

In an effort to confirm the expected negligible contribution due to mass impurities (Kr^+ ions), I also performed a small annealing study. Samples were annealed to 700 °C, as this should be sufficient to remove structural defects [72, 90] without resulting in migration of the krypton within the silicon (which should not occur until 900 °C [101]). This led to a complete restoration of thermal conductivity to that of pristine silicon (within uncertainty). This served as further evidence for the negligible contribution of mass and bonding effects from the ions to the reduction in thermal conductivity. Instead, boundary scattering (between amorphous and crystalline regions) and defect scattering (where a single ion can create many crystalline defects) were the predominant scattering mechanism leading to the great reduction in thermal conductivity observed.

3.5 Relevant publications

This work served as the first real-world exploration of the concepts developed in the previous chapter "Measurement uncertainty and systematic error", and I developed a novel methodology for handling thermal measurements of samples with spatial variations in properties. It was only though the discretization of the sample, and application of an assumed thermal conductivity function, by which the partially-amorphous / partially-crystalline region could be measured. Similarly, the acquisition of multiple TDTR datasets at multiple frequencies and subsequent overlapping of their contour volumes was required to establish acceptably low levels of uncertainty.

I have published this work in the Journal of Applied Physics, and am pleased to report that it was chosen as an Editor's Pick (T. W. Pfeifer, J. A. Tomko, E. R. Hoglund, E. A. Scott, K. Hattar, K. Huynh, M. Liao, M. Goorsky, P. E. Hopkins; "Measuring sub-surface spatially varying thermal conductivity of silicon implanted with krypton". J. Appl.

Phys. 21 August 2022; 132 (7): 075112. https://doi.org/10.1063/5.0094876). Additionally, my collaborators published a work looking deeper at the annealing effects (K. Huynh, Y. Wang, M. E. Liao, T. W. Pfeifer, J. A. Tomko, E. A. Scott, K. Hattar, P. E. Hopkins, M. S. Goorsky; "Depth-dependent recovery of thermal conductivity after recrystallization of amorphous silicon". J. Appl. Phys. 7 April 2023; 133 (13): 135101. https://doi.org/10.1063/5.0133548).

Chapter 4

An algorithm for multi-measurement data fitting

Having seen the power of fitting TDTR at multiple modulation frequencies, I considered what other measurements might benefit from the combined analysis of multiple datasets. Steady State Thermoreflectance (SSTR) traditionally only measures one single unknown, but could a multi-frequency SSTR approach work as well? Within the original work of Braun *et al.* [17], the authors used a dual- spot size approach, taking advantage of the differing sensitivity to different thermal properties in SSTR with varying spot sizes. This allowed two SSTR measurements to fit for two unknowns, and a two-frequency approach should work as well. A multi-frequency SSTR approach could further expand SSTR and even augment the dual- spot size approach for fitting additional unknowns. I also considered what thermal properties are difficult to measure, e.g., anisotropic samples or the TBR of a buried interface. This was the second project falling under the first thrust of my dissertation: "Development of new analysis methodologies for existing measurement techniques".

4.1 Multi-frequency SSTR

I began exploring multi-frequency SSTR (mf-SSTR) by measuring known calibration samples (a-SiO_2, c-Al_2O_3, and c-Si) in order to understand the capabilities and limitations of such a technique. It should be noted that at high frequency, the measurement is no longer occurring at steady state, however I will continue to use the name "Steady State Thermoreflectance" (SSTR), as the experiment is identical to a traditional (i.e., low-frequency) SSTR measurement in several ways. One might also argue that mf-SSTR is equivalent to FDTR, however several important distinctions should be made. In SSTR, the magnitude of the data is analyzed as opposed to the phase. SSTR also uses a reference sample to find a slope scaling parameter (γ). The reference sample should have an identical surface and transducer to the sample of interest, and the scaling parameter γ captures sample-dependent and system-dependent scaling effects (e.g., thermoreflectance coefficients, photodetector sensitivity, variations in the behavior of different electronic components, and optical losses through lenses and mirrors). For mf-SSTR, I still used a reference sample, as this avoids the need to normalize the data. While a magnitude-based FDTR measurement is possible, normalization of the data (without the use of the reference sample) will lead to high uncertainty. I also found that the magnitude scaling factor γ can differ across frequencies, which will complicate analysis if no reference sample is used. Collecting data at two frequencies also presents the opportunity for dramatic speed improvements over FDTR (where data is collected at many frequencies) and over dual-spot SSTR (where physical replacement of a microscope objective is likely required). As with the dual- spot size approach with SSTR, dual-frequency SSTR was able to measure two thermal parameters at once (e.g., thermal conductivity *and* thermal boundary resistance as seen in Fig. 4.1.a, or thermal conductivity *and* heat capacity, simultaneously).

To understand why this works, we must consider sensitivity of the experiment under differing measurement conditions. If each parameter affects the slope of the data differently under different conditions (modulation frequency or laser spot size), then the two measurements are thus able to solve for two unknowns. This can be visualized by way of contour analysis. For traditional single-frequency SSTR, the slope is the only meaningful piece of data from a given measurement. If two parameters are unknown, there are arbitrarily many solutions. This can be seen in Figure 4.1 for the fit of an 80 nm aluminum / bulk silicon sample, when the measurement of the Al / Si TBR and the silicon thermal conductivity are considered. For a single SSTR measurement (e.g., the traditional low-frequency SSTR measurement, the blue line in Fig. 4.1.a), arbitrary thermal conductivity values will fit the data if the TBR is similarly adjusted to yield the correct net resistivity of the sample (Fig. 4.1.b, blue band). In the previous chapter "Measurement uncertainty and systematic error", we saw ellipses while performing contour analysis for TDTR data, however in the SSTR case, the contours are unlimited and take the form of contour "bands". For *K* and TBR, these bands follow an approximately -1/x trend; a thermal conductivity of 100 W m^{-1} K^{-1} and TBR of 7.5 m^2 K GW^{-1} fits equally as well as a thermal conductivity of 250 W m^{-1} K^{-1} and a TBR of 16 m^2 K GW^{-1} for the 1 kHz modulation frequency measurement, and this relationship extends to a thermal conductivity of zero or infinity. With two measurements performed however, an overlap between these two contour "bands" is found (red and blue bands in Fig. 4.1.b). Interestingly, the overlapped area between these two contour bands yields a smaller range for TBR than TDTR alone. TDTR achieves a smaller range of values for thermal conductivity however. This suggests one's selection of experiment should depend on the specific parameter of interest.

The ratio of sensitivity of the measurement to the given parameters is also seen in the slope of the bands found during contour analysis. If the band were either completely flat or vertical, this would suggest the measurement is insensitive to one parameter (and that the assumption for that parameter would not affect the fit for the other). In this case, neither band is flat or vertical, meaning this assumption would be inappropriate. Similarly, two experiments with similar sensitivity to both parameters will not benefit from the overlapping of their contour bands, and one may no longer be able to measure both parameters.

This is the similar mechanism by which Braun *et al.* [17] fit *K* and TBR simultaneously

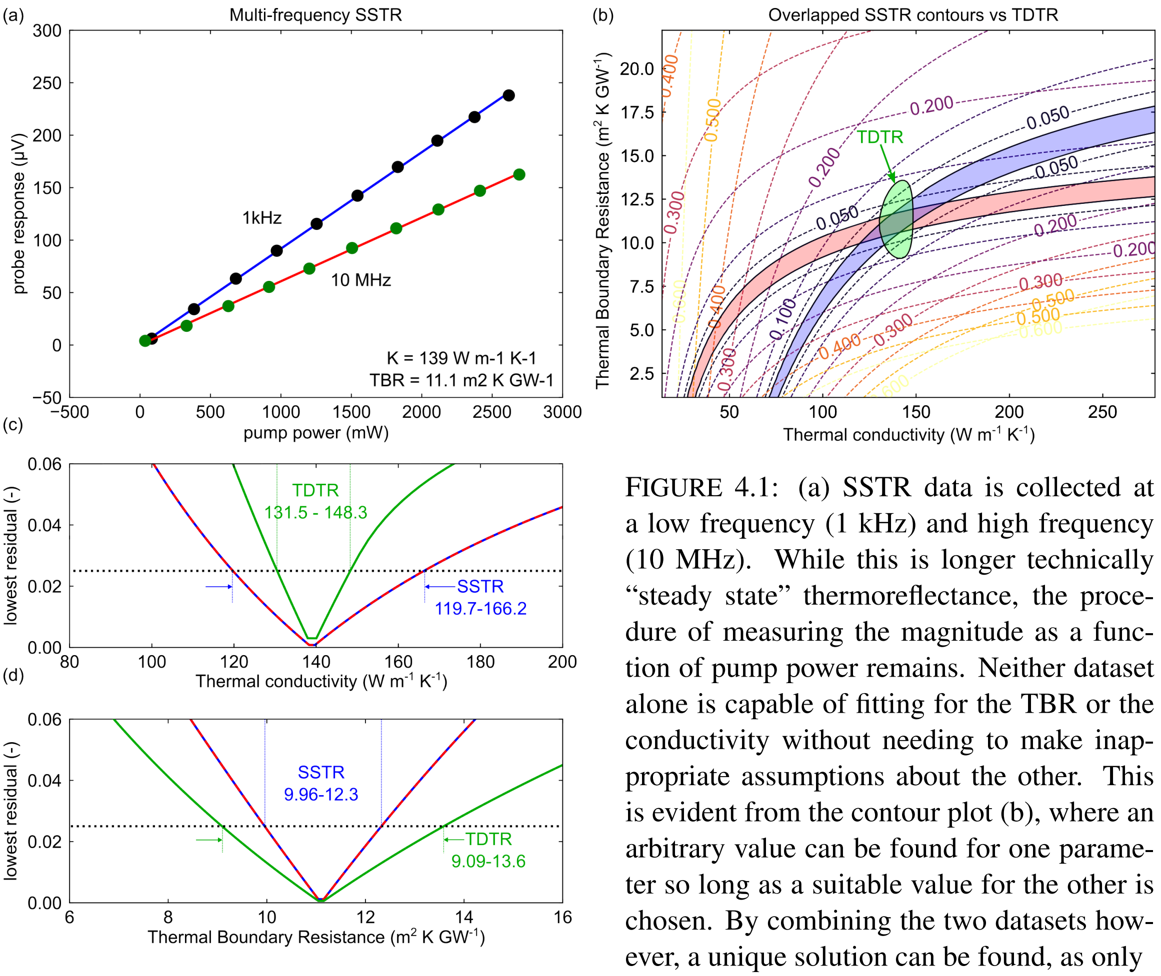

FIGURE 4.1: (a) SSTR data is collected at a low frequency (1 kHz) and high frequency (10 MHz). While this is longer technically "steady state" thermoreflectance, the procedure of measuring the magnitude as a function of pump power remains. Neither dataset alone is capable of fitting for the TBR or the conductivity without needing to make inappropriate assumptions about the other. This is evident from the contour plot (b), where an arbitrary value can be found for one parameter so long as a suitable value for the other is chosen. By combining the two datasets however, a unique solution can be found, as only the overlapped area inside both contour bands satisfies both datasets. Contour results are compared between mf-SSTR (red and blue) and TDTR (green) for both 2D (b) and 1D contours (c). Depending on the parameter of interest, mf-SSTR may yield smaller bounds than TDTR. In this experiment, γ was found via an aluminum/a-SiO$_2$ reference sample. I chose aluminum/a-SiO$_2$ as the experiment has negligible sensitivity to $R_{\mathrm{Al/a-SiO_2}}$. Any uncertainty in reference sample parameters must be propagated through the analysis and will contribute to uncertainty in the final fitted results, as was discussed in the previous Chapter "Measurement Uncertainty and Systematic Error".

using SSTR using data collected with two spot sizes. A key difference between the procedures is the use of contour *bands* with a finite width however, which also lends insight into the limitations of this approach. While it may seem intuitive to expand this: 3 frequency SSTR to fit for 3 unknowns and so on, contour analysis should make it clear why this can not be done.

Beginning with the simplest case, e.g., fitting 2 unknowns using 3 datasets (conceivably in an effort to reduce our measurement error), the contour plot in Fig.4.1 should make it clear why this will not work. Adding an intermediate frequency dataset will add an intermediate band on the contour plot, which may not actually provide any benefit in reducing the extent of the overlapped region.

We can also consider using the 3 datasets to fit for three unknowns. If we first consider merely finding *a* solution in 3D parameter space (e.g., fitting for K, C, and TBR), this can be represented as an infinitely thin contour surface for a single SSTR dataset, where this surface follows the form $z = x^{-1} \cdot y^{-1}$. An example of this is shown in the following section in Figure 4.3.b. Each dataset will find many different combinations of the three parameters, but there will be a single point in the 3D parameter space where these surfaces intersect (a system of three equations can solve for three unknowns). This would suggest one could fit for all three parameters (and nominally, you can). With a finite thickness applied to each surface however, a potentially huge volume might exist within the intersection of the three. In other words, when you are rigorous about experimental error, honest about the capabilities of the measurement system, and honest about the limitations of your alignment and calibration procedure (recognizing that the measured data may deviate from the true expected curve due to a variety of real-world reasons), you will find that the inclusion of additional measurements may not enable endless fitting of additional parameters.

4.2 Hybrid SSTR+TDTR fitting for buried interfaces

With mf-SSTR, the capabilities of the combined fitting of multiple datasets were greater than the sum of each part. I wanted to expand this concept further, exploring the ability to fit multiple different types of data. My collaborators were interested in measuring the TBR between diamond and $Al_{0.65}Ga_{0.35}N$ (STEM image shown in Figure 4.2.a), a material system highly relevant for use in semiconductor devices [102]. Given the extremely high conductivity of single-crystal diamond (> 2000 W m^{-1} K^{-1}), it is also a highly desirable material for use with packaging of devices where thermal management is a concern. Unfortunately however, the extremely high conductivity of diamond is a direct product of the high frequency phonons present within the system (high group velocities within the kinetic equation: $K = \frac{1}{3} \cdot C \cdot v \cdot l$), which means it will fundamentally tend to have a high TBR when used in conjunction with most other materials (poor overlap between vibrational populations). This means TBR is fundamentally a limiting factor when using diamond for devices and packaging, and there is great interest in overcoming this limitation.

Numerous authors have proposed the use of "vibrational bridging" as a mechanism for reducing TBR [103–107]. This consists of adding one or more intermediate (or intermixed) layers at the interface, providing a volume with an intermediate vDOS, allowing easier conversion of heat between the vibrational populations on either side. Multiple studies on diamond specifically have also attempted to achieve a reduction in diamond / film TBR by adding interlayers [55, 108, 109], with promising results depending on the interlayer material and thickness.

In this study, my collaborators wanted to explore the addition of SiC and B_4C, since both of these materials have an intermediate vibrational density of states between diamond and AlGaN. TBR measurements for samples with and without an interlayer could thus be compared to explore these bridging effects. It has also been shown that plasma-assisted microwave chemical vapor deposition (PMCVD) of diamond can cause surface damage to AlGaN, so the use of interlayers in devices are of interest to protect the surface and ensure better mechanical bonding [110]. To study the effects of the interlayers, AlGaN samples were grown via Metal-Organic Chemical Vapor Deposition (MOCVD), interlayers were sputtered, and polycrystalline diamond was grown via PMCVD. An aluminum transducer was deposited via e-beam evaporation, in preparation for thermoreflectance measurements.

These material systems pose a serious challenge for existing measurement techniques however. Size effects and potential crystallinity effects may reduce thermal conductivity, meaning the diamond conductivity can not be assumed. Similarly, given the requirement for a transducer in thermoreflectance experiments, the TBR between aluminum and diamond must also be considered. TDTR alone is unable to measure all three unknowns: K_{diamond}, $R_{\text{Al/diamond}}$, and the $R_{\text{diamond/AlGaN}}$ of interest. This is evident from contour analysis, where the bounds of the contour volume are quite large. The contours are unconstrained in some cases, meaning that *any* value for $R_{\text{diamond/AlGaN}}$ can be chosen and acceptable fits might still be found by adjusting $R_{\text{Al/diamond}}$ and K_{diamond}. This is similar to the buried interface example outlined in the chapter "Measurement uncertainty and systematic error" previously. This situation is not helped through the use of multi-frequncy TDTR either. One strategy might be to select a measurement which is only sensitive to one or two of the parameters, then use a separate measurement for the remaining. For the case of aluminum / diamond / AlGaN however, each measurement considered (TDTR, FDTR, SSTR) remained sensitive to all three parameters, so this was not an option. By performing simultaneous fitting of both TDTR and SSTR data however (seen in Fig. 4.2), and by considering the boolean intersection of TDTR and SSTR 3D contours (Fig. 4.3), the contour error bounds were greatly reduced. We found a $R_{\text{diamond/AlGaN}}$ of 21.6 ± 5.6 m^2 K GW^{-1}, which is quite high, and suggests that the boundary would play a huge role in limiting thermal dissipation if this were to be included in an electronic device. Upon adding a B_4C interlayer however, the TBR was reduced to 3.4 m^2 K GW^{-1}. No lower bound could be established, but contour analysis suggested TBR did not exceed 6.5 m^2 K GW^{-1}. Of note, the inability to establish a lower bound for TBR does not mean the TBR is plausibly zero [109]; it only means the measurement is not sensitive enough to detect exceptionally-low thermal boundary resistances located well-below the surface. This quantitative comparison between the interlayer and non-interlayer samples would not have been possible with existing techniques, as the error would have been too high to allow the drawing of conclusions. Similarly, slight changes in diamond crystallinity (due to potential differences in growth conditions from the presence of the interlayer) also prevented a direct qualitative comparison of data. Using combined fitting of TDTR and SSTR data however, reasonable uncertainty could be established. These measurements also support the hypothesis that B_4C should serve as a vibrational bridge, assisting in the conversion of energy between modes on either side of the interface.

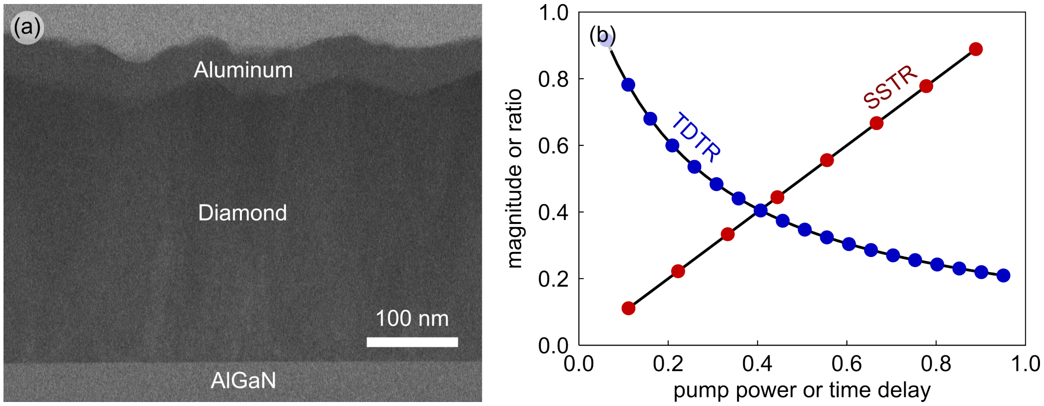

FIGURE 4.2: Measuring the TBR between polycrystalline diamond and AlGaN is difficult, as the transducer / diamond TBR, diamond thermal conductivity, and diamond / AlGaN TBR are all unknown. (a) TEM images are shown of the sample stack. (b) simultaneous fitting of SSTR and TDTR data was the only way to achieve reasonable uncertainty.

4.3 Hybrid SSTR+TDTR fitting for highly anisotropic materials

Having successfully measured the Diamond / $Al_{0.65}Ga_{0.35}N$ TBR, the same collaborators were also interested in the measurement of AlN / $Al_{0.9}Ga_{0.1}N$ superlattices. Superlattices are particularly interesting for their optical properties (e.g., used for LEDs), high carrier density (due to the presence of 2D electron gas at interfaces), and for their fascinating thermal properties (where coherent phonons can exist cross-plane at high interface densities). These particular samples were grown via metal modulated epitaxy (MME), and were expected to be extremely high purity, high crystallinity, and nearly epitaxial. High crystallinity would suggest the samples should have a high in-plane thermal conductivity ($K_{\parallel}$, as scattering from interfaces should only minimally affect the in-plane conductivity). Several samples also had periodicity on the order of single-digit unit cells (often referred to as "digital alloys"). It has been shown that at high interface densities, cross-plane thermal conductivity ($K_{\perp}$) can increase due to coherent transport of phonons [66] (as opposed to lower thermal conductivities due to high scattering rates at intermediate interface densities). Due to these effects (and likely varying effects as a function of interface density), my collaborators and I expected a potentially high degree of anisotropy, and again needed to

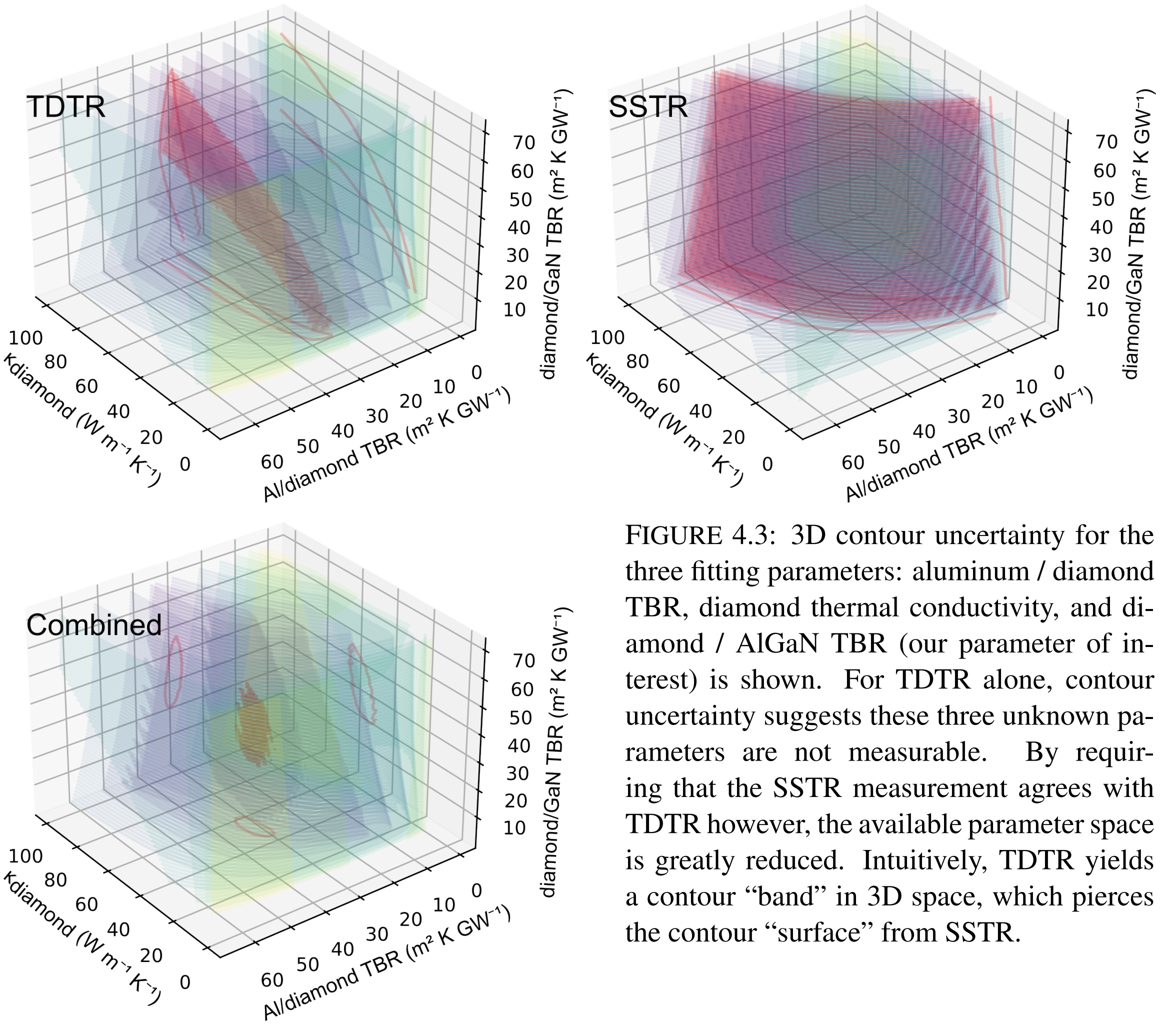

FIGURE 4.3: 3D contour uncertainty for the three fitting parameters: aluminum / diamond TBR, diamond thermal conductivity, and diamond / AlGaN TBR (our parameter of interest) is shown. For TDTR alone, contour uncertainty suggests these three unknown parameters are not measurable. By requiring that the SSTR measurement agrees with TDTR however, the available parameter space is greatly reduced. Intuitively, TDTR yields a contour "band" in 3D space, which pierces the contour "surface" from SSTR.

measure 3 unknown thermal parameters: $R_{\mathrm{Al/superlattice}}$, $K_\perp$, and $K_\parallel$. I again used the hybrid TDTR+SSTR fitting approach, and found the most highly anisotropic sample had a $K_\parallel$ of 39.8 ± 2.1 W m^{-1} K^{-1} compared to $K_\perp$ of 9.6 ± 0.5 W m^{-1} K^{-1}. This is for a sample with a periodicity of ~ 6 nm, which is a relatively high interface density and a high thermal conductivity as well. The incredibly high degree of anisotropy also has significant ramifications for device cooling, as subsequent finite element simulations were able to show that thermal spreading can be used to engineer better thermal dissipation within the device architecture.

4.4 Hybrid fitting algorithm

The precise fitting algorithm needed for fitting datasets of different types warrants discussion. I found two procedures worked well, each with their own advantages. Traditional TDTR fitting is done using least-squares curve fitting: 1) a model function is written which is capable of generating the TDTR decay curve for a given set of parameters (this is the implementation of the math found in Cahill [15], Schmidt [16], or Braun [17]) 2) the function and dataset are fed into a curve fitting algorithm (e.g., python's scipy.optimize.curve_fit or MATLAB's lsqnonlin), and 3) the algorithm iterates through a series of thermal parameters until a match between the data and model is found (quantified via the mean squared error between curve and data points). A naive approach to simultaneous fitting might involve simply appending one dataset (and model function output) to the other, and using the same curve-fitting algorithm. This works well for fitting similar datasets (e.g., multi-frequency TDTR or multi-frequency SSTR). For datasets of different types however, the weighting of the datasets must be considered. The MSE value between a given dataset and model curve depends on the number of data points and the scaling of the values in the dataset. This means the weighting is likely to be different between SSTR (e.g., 10 datapoints, with values of 100 uV) and TDTR (e.g., ≥ 30 datapoints, with ratio values between 1-6 (unitless)). I found two solutions for this problem. First, the datasets (and function outputs) can be scaled before appending one to the other, which mitigates these scaling issues to a degree. Alternatively, a scaling-proof and length-proof residual can be used [25]:

$$residual = \sqrt{\frac{\sum_i [F_i(x) - D_i(i)]^2}{\sum_i F_i(x)^2}} \tag{4.1}$$

where F_i and D_i are values within the function and dataset respectively. Each dataset and function can be compared individually, with one residual calculated per measurement, and the maximum residual (worst fitting) returned to a minimization function instead of the curve-fitting algorithm. This means that at any given point during the minimization process, the worst-fitting dataset will guide the fit, and an equal weighting of the datasets will be guaranteed. If an uneven weighting is desired (e.g., one measurement is trusted more than the other), an artificial weighting can still be applied by simply scaling the residual value. While the latter approach guarantees equal weighting of the datasets, there is an inherent discontinuity in the parameter space which may cause issues. As the minimization function converges towards the correct solution, the dataset controlling the descent may switch, and depending on the algorithm used, this may cause a failure to converge on the best solution available. This is visualized in Fig. 4.4.

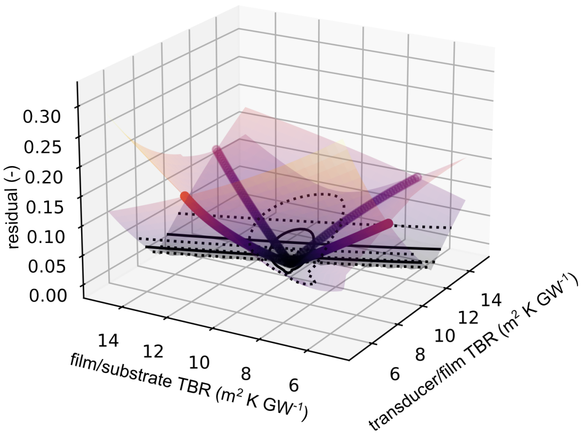

FIGURE 4.4: In one hybrid fitting scheme, the minimization function is passed the highest residual value across datasets. The 2D contour plots we have seen thus far are technically surface plots, where the height of the surface represents the residual of the fit for any pair of the two parameter values. For multiple datasets, the surfaces for each dataset will intersect, and the upper surface represents the worst fit across datasets. The minimization scheme is tasked with "walking downhill" along this upper surface until a local minimum is reached. If steps are taken according to the gradient of the surface, this may result in instability when the crook of a "valley" is reached (bold curves). This discontinuity may cause instability and failure of convergence depending the minimization algorithm used.

4.5 Relevant publications

In all cases (multi-frequency SSTR, or combined SSTR+TDTR), the benefits are clear: in situations where one measurement individually fails to measure a parameter of interest, and making assumptions to reduce the unknowns would be inappropriate, the abilities of the combined measurement may be greater than simply the sum of the two.

The multi-frequency SSTR analysis served as a useful proving ground for the fundamental mechanism by which multi-measurement data fitting can reduce uncertainty and/or allow measurement of additional unknowns. It also demonstrated the limits of these approaches, showing that "two measurements = two unknowns" is not necessarily extendable to "three measurements = three unknowns". Hybrid SSTR+TDTR fitting enabled measurement of both diamond / AlGaN TBR, and the anisotropic thermal conductivity of AlN / AlGaN superlattices. These material systems served as an excellent case study, as both of these were scenarios where the traditional approaches (including multi-frequency TDTR) failed to resolve all unknowns. The contour overlapping procedure demonstrated in both the mf-SSTR and SSTR+TDTR mini-studies can also serve as guidance for proper selection of the correct measurement tool. Running contour (and contour overlapping) analysis on synthetic data (for numerous measurement types or combinations) prior to the collection of data allowed for efficient collection of data using the best measurement tools to minimize error.

Aside from the data processing and conceptual advances, the diamond / AlGaN and AlN / AlGaN mini-studies have great real-world applications. In the case of the diamond / AlGaN samples, I was able to measure the buried interfacial TBR, a parameter that would not be measurable otherwise. Rigorous uncertainty, and maintenance of trends outside of uncertainty also meant we could confidently draw conclusions on the interlayer effects, noting that the growth of a B_4C interlayer was able to reduce the TBR by a factor of 4. We believe this is due to a vibrational bridging effect, where B_4C has a vibrational density of states roughly between the diamond and AlGaN. The AlN / AlGaN digital alloys also represent some of the highest measured thermal conductivity and anisotropy of low-periodicity (high interface density) superlattices to date. The diamond / AlGaN results were recently published in Advanced Materials Interfaces (H. T. Aller, T. W. Pfeifer, A. Mamun, K. Huynh, M. Tadjer, T. Feygelson, K. Hobart, T. Anderson, B. Pate, A. Jacobs, J. S. Lundh, M. Goorsky, A. Khan, P. E. Hopkins, S. Graham, "Low Thermal Resistance of Diamond-AlGaN Interfaces Achieved Using Carbide Interlayers" *Advanced Materials Interfaces* (2024) DOI: 10.1002/admi.202400575), and a manuscript for the AlN / AlGaN results is currently in the final stages of preparation (H. T. Aller, T. W. Pfeifer, A. Chaney, K. Averett, T. Asel, A. Khan, P. E. Hopkins, S. Mou, S. Graham, "Modeling the Impact of

Device Architecture on the Thermal Response of AlN / AlGaN Digital Alloy Field-Effect Transistors”).

Chapter 5

Measurement and simulation of the effects of irradiation on Thermal Boundary Resistance

Having explored the role of irradiation on thermal conductivity, I was also curious to dig deeper into the role these defects play on thermal boundary resistance (TBR). Numerous authors have explored atomic manipulation of the interface, however results have been mixed. Some authors observed an increase in TBR both computationally [111–113] and experimentally [11, 62, 105, 114–116], while others have pointed to the vibrational density of states “bridging” effect to explain a reduction in TBR [103–106]. Interfacial roughening has also been shown to yield a reduction in TBR, either from bridging (where the roughened area is partially comprised of both materials) or through an increase in interfacial surface area [117, 118].

Much of this work has been based on the premise that the overlapping of the vibrational density of states between the two materials controls the TBR, however numerous authors have also pointed to the importance of scattering. Scattering is the mechanism by which heat is converted between two vibrational populations [119, 120], meaning variations in TBR can be explained by calculating the correlations between vibrational modes [121], and

TBR can be reduced by enhancing the scattering across the interface [45, 122]. Scattering within the material adjacent to the interface has also been considered, since differing bulk vs. interfacial vibrational populations will still require scattering in order for energy to be exchanged [121, 123–131].

Due to disagreement within literature on the effects of irradiation and disorder (and due to the many complications involved in directly interpreting experimental results), I designed a study to explore irradiation effects on TBR in GaN. This also offered an opportunity to delve into nanoscale atomistic simulations, and is the first project under my second thrust “Advancements to computational techniques”.

5.1 Experimental design

In this study, Gallium Nitride (GaN) was irradiated with a variety of ions (C^+, N^+, and Ga^{3+}), chosen to allow exploration of whether trends might depend on either the mass of the defects or chemical compatibility with the target material. I selected ion dose and energy based on simulations using the Stopping Ranges of Ions in Matter (SRIM) [68] software. Three doses were used for each ion, chosen such that the highest dose would yield an estimated 2% structural disorder near the interface, as a preliminary study suggested this level of disorder may yield a reduction in TBR. In the interest of avoiding the analysis complications seen in the depth-varying thermal conductivity study (Chapter titled “Measurement of depth-varying thermal conductivity”), I chose irradiation energies such that the predicted ion stopping range would be ~ 3 µm, which is well outside the thermal penetration depth for TDTR. Following irradiation, aluminum transducers were deposited, and the aluminum / irradiated GaN TBR was measured. Aluminum was deposited using two different procedures, to ensure trends were not a product of the transducer preparation. The first sample set used our typical procedure for aluminum deposition, which involved a series of cleaning steps (sonication with deionized water, isopropyl alcohol, acetone, and methanol, drying with air, and O_2 plasma cleaning), followed by e-beam evaporation of the aluminum. The

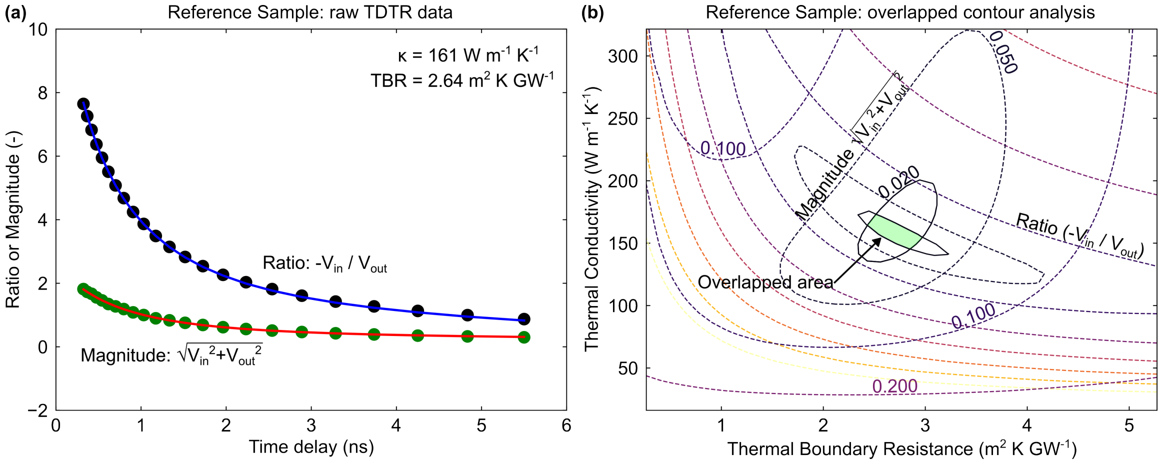

FIGURE 5.1: (a) An example of raw TDTR data is shown, fitting for both the ratio of in-phase (V_{in}) and out-of-phase (V_{out}) data and the signal magnitude. Contours are calculated for both (b), by calculating the quality of fit between data and the model across the full parameter space (all combinations of K and TBR). The overlapped area represents the range of values yielding a satisfactory fit (2% residual) in both ratio and magnitude.

second sample set (prepared by my collaborators in the Doolittle group at Georgia Tech) consisted of an HF surface cleaning, ultra-high vacuum (UHV) heat-treatment, and aluminum grown via Molecular Beam Epitaxy (MBE). I measured all samples using Time Domain Thermoreflectance (TDTR).

In order to achieve acceptable uncertainty, I used a combined ratio (in-phase vs. out-of-phase signals) and magnitude (normalized) fitting procedure for the data to fit for the GaN thermal conductivity and aluminum / GaN TBR. This fitting technique was alluded to in the previous chapter “Measurement uncertainty and systematic error”, and this is an instance where the procedure provides clear benefit. An example of this can be seen in Figure 5.1, where smaller contour bounds are found when both contours for ratio and magnitude are overlapped.

5.2 In-plane spatial variation due to uneven ion irradiation

While measuring the samples with TDTR, I noticed extreme variation in results, even for measurements across the same sample. Typically, a uniform ion dose is achieved by either adjusting the ion beam diameter to cover the entire surface, or by rastering the beam across the sample. If rastering was performed with too much separation between strokes, spatial variation may result, occurring over distances on the order of the beam size (millimeters). The resultant ranges of doses may also vary by orders of magnitude if parts of the sample are only exposed to the edges of the Gaussian beam.

To characterize spatial variation across samples, I took advantage of the low acquisition times of SSTR to perform thermal resistance mapping across the entirety of each sample [132]. Under the experimental conditions used (e.g., 2.8 µm and 3.4 µm pump and probe 1/e^2 diameter at 1 kHz), SSTR is approximately 5× as sensitive to the GaN thermal conductivity (130 W m^{-1} K^{-1}, pristine) as TBR (2.8 m^2 K GW^{-1}, pristine, for the UHV aluminum samples). Based on the assumptions that 1) ion bombardment will reduce thermal conductivity as dose increases and 2) SSTR is much more sensitive to thermal conductivity, I could thus treat the SSTR maps as a qualitative indicator of dose variation across each sample.

By collecting TDTR data at various points around the dose map, I could gain a better understanding of how both thermal conductivity and TBR varied within a given sample. For samples with high variability in dose, I used the fitted thermal conductivity values to filter the measurements. I only used the measurements with intermediate thermal conductivity values for the final total (those within one standard deviation of the mean), as these locations were most likely to be close to the nominal targeted dose. This can be seen in Figure 5.2 below, for two samples with high variability. The measured TDTR locations are identified in green or red, with green denoting the measurements which were kept for the final TBR results.

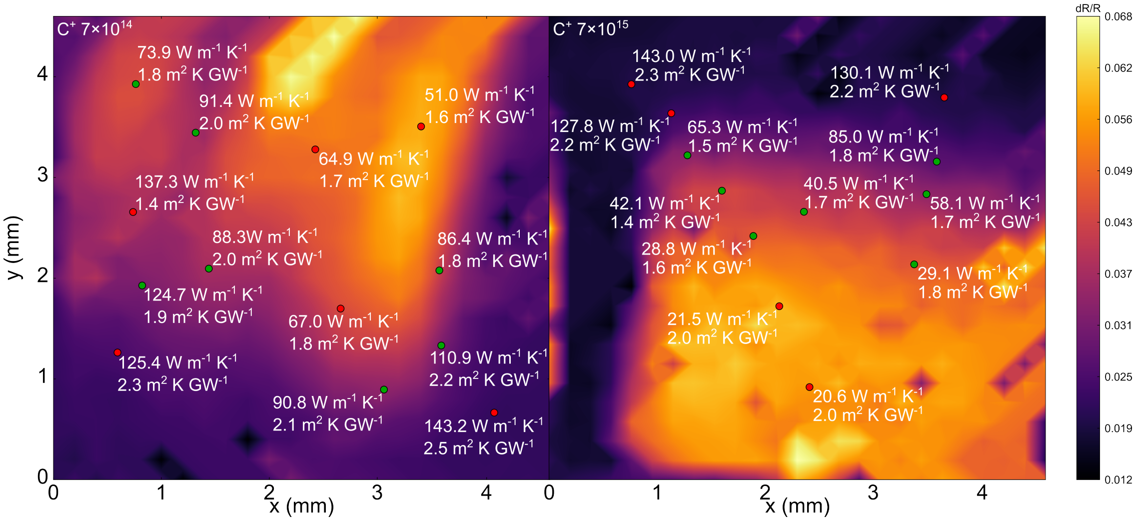

FIGURE 5.2: Higher sensitivity to thermal conductivity meant SSTR magnitude maps could be used as a qualitative indicator of dose variation across a given sample (intermediate and high C^+ dose samples pictured). The heatmap intensity indicates the relative SSTR signal at each point, and the red and green points denote where TDTR scans were taken. If TDTR fitted conductivity fell within 1 standard deviation of the sample's mean, the TBR was included in the final analysis (green), and anything else (red) was excluded.

5.3 Experimental results

For the samples subjected to alcohol cleaning with e-beam deposited aluminum, I found TBR values in the range of 9-13 m^2 K GW^{-1} (Fig. 5.3.a, open symbols), whereas the more thorough ultra-high vacuum (UHV) cleaned / MBE-grown aluminum samples yielded lower TBR values by roughly a factor of 4 (Fig. 5.3.a, closed symbols). Both datasets showed a trend in nominally fitted values, with an increasing dose leading to a reduction in TBR. Once rigorous uncertainty was considered however, only the trend in the latter sample set was maintained. Given that both surface roughness and interfacial mixing have been shown to lead to a decrease in TBR in certain situations [12, 45, 59, 103, 113, 115, 117, 120, 133–136], I performed scanning transmission electron microscopy (STEM) on C^+ irradiated samples from the UHV cleaned / MBE aluminum set (Fig. 5.3.b,c). I found a ~ 2 nm interlayer between the Aluminum / GaN which was present across all samples on which STEM was performed. I also found no discernible differences in surface roughness or crystallinity despite measuring different TBRs. This suggests interfacial cleanliness or crystallinity effects were not responsible for the irradiation-induced reduction in TBR.

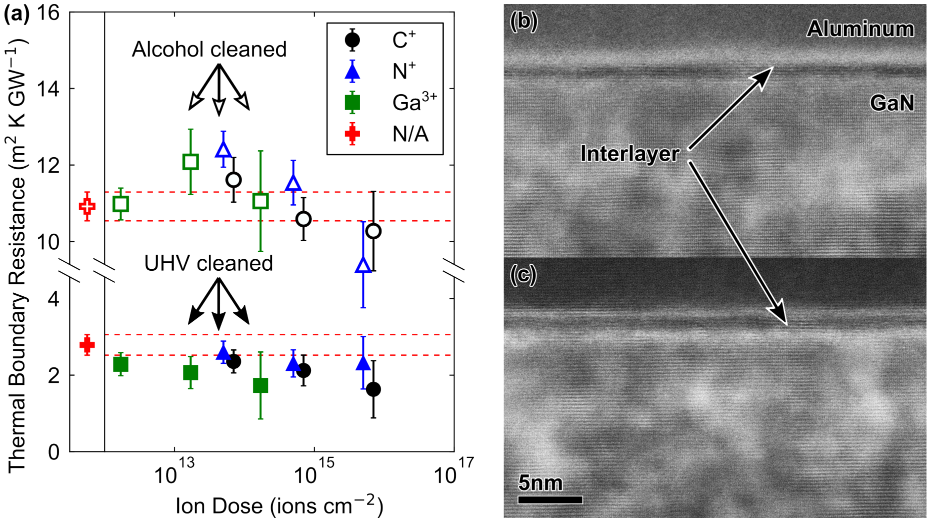

FIGURE 5.3: (a) TBR was measured between the aluminum capping layer and ion-irradiated GaN. Two sample sets were prepared, first using our standard alcohol cleaning / e-beam aluminum deposition procedure (open symbols), and separately using a more rigorous ultra-high vacuum (UHV) cleaning / MBE deposition process (filled symbols). A trend in nominal TBR values appeared for both, with the alcohol cleaned samples showing TBR values roughly 4× higher. Once rigorous uncertainty was considered however (calculated via contour analysis and the standard deviation across multiple measurements) the trend was difficult to establish for the alcohol-cleaned samples. By comparison, a trend was clear with the UHV / MBE samples, with a near-universal reduction in TBR following bombardment. STEM images were taken on low (b) and intermediate (c) doses C$^+$ samples within the UHV / MBE sample set, and no significant qualitative differences were seen at the interface to explain the difference in TBR. Both have a ~2 nm intermediate layer between the Al and GaN.

5.4 Considering depth-dependent properties

While I took efforts with experimental design to ensure the ion stopping depth was beyond the measurement depth of TDTR, a gradient in damage and ion implantation will occur through the entire depth of any irradiated sample. The concept of a discrete measurement depth (where one is sensitive to parameters above, and insensitive to parameters below) is also a bit of a misnomer. In reality, there is a thermal decay through the depth of the sample, and one has a continuously-varying and diminishing sensitivity to properties at increased depths. This thermal gradient is shown in Figure 1.3, where the nominal thermal penetration depth merely denotes the depth at which the temperature reaches 1/e that of the surface.

Both of these factors suggest that TDTR may have a small (but non-zero) sensitivity to deeper regions where the ions came to rest, and I had to ensure a gradient in thermal conductivity for the shallower regions of each sample were not affecting the inferred trend in TBR.

In the previous chapter "Measurement of depth-varying thermal conductivity" I developed a fitting scheme for handling continuously-varying properties though the depth of a sample, and in the chapter "An algorithm for multi-measurement data fitting" I developed a means of combining TDTR and SSTR data. I thus applied a skewed Gaussian distribution to the thermal conductivity profile, now fitting for the aluminum / GaN TBR, and the three Gaussian parameters (lowest thermal conductivity, location of the lowest thermal conductivity point, and the spread). SRIM predictions for the ion and damage profiles (shown in Figure 5.4.a below) appeared more skewed or asymmetric than in the Kr^+-irradiated case. Due to the added fitting parameters, I needed to use both ratio and magnitude information from the TDTR datasets, and the SSTR data from the mapping discussed previously. Once all datasets were included, I was again able to establish the reduction in TBR due to irradiation. 1D contours for the various methods can be seen in Figure 5.4.b below. Using the TDTR data alone (blue curve), the extent of the contours is much larger due to the introduction of the additional parameters. Adding SSTR data to the analysis yields similar ranges to what was seen before.

Not only did this serve to further support the experimental trends observed using the traditional fitting schemes, but this also offered a unique opportunity to better understand the mechanism by why the hybrid TDTR+SSTR fitting approach reduces uncertainty. SSTR is typically considered to only be sensitive to one unknown parameter, however it may be more appropriate to consider it as a measure of the net thermal resistivity of the sample within the measured volume (the net thermal resistivity being proportional to the slope of the dataset). While there may be many combinations of all unknowns which yield acceptable fits to the TDTR dataset (considering both ratio and magnitude information alone),

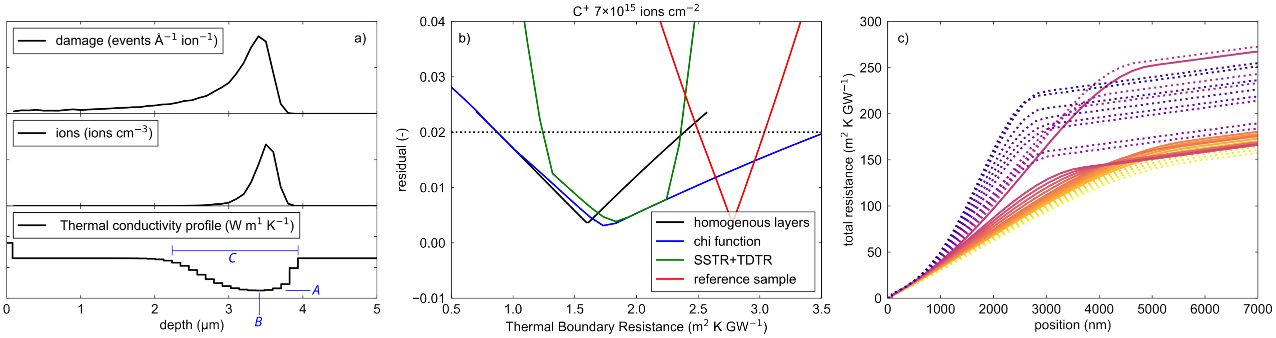

FIGURE 5.4: (a) SRIM predicts a skewed distribution for implanted ions and irradiation-induced damage (top and middle), which I included in the thermal conductivity profile (bottom). On an exploratory basis, I fit for the center thermal conductivity (*A*), location (*B*), and spread (*C*) using the approach I pioneered previously, in addition to the TBR. (b) I performed contour analysis for each method of analyzing the data, showing the best residual (fitting for *A*, *B*, *C*) for a sweep of TBR values. The traditional method of fitting (assuming each layer has homogeneous properties and fitting for TBR and thermal conductivity of the GaN layer) is shown for the highest dose C^{+} irradiated sample (black) and the unirradiated sample (red). Below the chosen quality-of-fit threshold (dotted) the two do not overlap, implying the nominally observed trend (irradiated sample has a lower TBR) was valid. This procedure was repeated with the depth-varying thermal resistance procedure using TDTR data alone (blue) or enhanced by the addition of SSTR (green), showing the trend was maintained with this more experimental fitting method. (c) the depth-varying conductivity functions found by fitting TDTR are shown. Given that SSTR is a measure of the net thermal resistance within a given region, SSTR serves to narrow the range of acceptable functions (solid).

SSTR serves to limit the combinations available. Plotting the total resistance as a function of depth for various combinations of the fitted unknowns (Fig. 5.4.c), many thermal resistance vs. depth profiles can be found (all curves). By limiting the results to those within a range of slopes at low depth (as controlled by SSTR), many candidate solutions can be excluded, and smaller bounds on TBR can be acquired (solid curves).

5.5 Simulation setup

The overlap of both materials' density of states is often considered to be the primary driver of TBR [11], but it was unclear how the addition of defects should lead to an increase in density of state overlap. Seeking to explore this further, I turned to molecular dynamics simulations. I chose to model a simplified toy system of Stillinger-Weber (SW) silicon (28.0855 g/mol) / heavy silicon (72.64 g/mol), as this allowed direct comparison to literature [44, 121, 137]. Using a toy system also allowed me to make more generalized observations, rather than simply replicating the experimental system. Following initialization of the simulation volume, I introduced interstitial / void pairs (Frenkel defects), since one would expect crystalline disorder to be the primary near-interface effect of irradiation [72–75]. Simulation size and computational limitations (tens of unit cell simulations lengths) also prevent the simulation of more complicated structural defect arrangements. These Frenkel defects were introduced by pseudo-randomly selecting and displacing atoms, and I found the defects were stable in SW silicon. This was not the case for other systems, such as those using the more computationally-efficient Lennard-Jones potential, as the system would either amorphize or recrystallize to FCC.

To extract TBR from the model systems, I ran non-equilibrium molecular dynamics (NEMD) simulations using LAMMPS (Large-scale Atomic/Molecular Massively Parallel Simulator) [138]. A long rod of atoms was initialized, comprised of silicon and heavy silicon on either side. A hot and cold temperature bath was applied to either end, and the temperature drop across the interface was used to calculate TBR (as pictured in Fig.1.5). I ran three sets of simulations: a baseline case where no defects were added, and simulations in which I added Frenkel defects to the silicon or heavy silicon sides. I added defects by randomly selecting a set number of atoms in each monolayer (ensuring a uniform defect density through the length of the simulation) and displacing them 2.5 unit cells (minimizing recombination effects). I used a 2% concentration of defects, so as to match the predictions for the maximum near-interface defect density from SRIM. During the initialization, I also performed a pseudo-annealing step, wherein I initialized the system to 1.5× the desired equilibrium temperature and ramped downward using an NVT ensemble. This ensured any defect evolution or recombination would occur at the beginning of the simulation before averaging began (prior to extraction of TBR or vDOS).

I also calculated the spectral heat flux (SHF) between groups of atoms by tracking the velocities of each atom and interatomic forces [44–47, 139–142]. The heat flux can be calculated from the work done by one group of atoms on another, which is expressed as:

$$Q_{A\to B} = \sum_{i}^{A}\sum_{j}^{B} F_{ij}\cdot v_i - F_{ji}\cdot v_j \tag{5.1}$$

for all atoms i and j in groups A and B respectively, where F_{ij} is the force applied to atom i by atom j, v_i is the velocity of atom i, and vice versa. In other words, the net work between atoms i and j is the work done on atom i by j minus the work done on atom j by atom i. To calculate the work in the frequency domain, forces and velocities can either be calculated in the frequency domain via their independent Fourier transforms:

$$F(\omega) = \mathscr{F}F(t) \quad ; \quad v(\omega) = \mathscr{F}v(t) \tag{5.2}$$

$$Q_{A\to B}(\omega) = \sum_{i}^{A}\sum_{j}^{B} F_{ij}(\omega)\cdot v_i(\omega) - F_{ji}(\omega)\cdot v_j(\omega) \tag{5.3}$$

or the convolution theorem can be used (stating that multiplication in the frequency domain is equivalent to the convolution in the time domain):

$$Q_{A\to B}(\omega) = \mathscr{F}\sum_{i}\sum_{j}\langle F_{ij}(t), v_i(t)\rangle - \langle F_{ji}(t), v_j(t)\rangle \tag{5.4}$$

where $\langle\rangle$ denotes the convolution. At the atomic level, the calculation of work between atoms is the heat flow as a function of vibrational frequency, and in some scenarios, this can be quite different from the vibrational density of states (i.e., not all modes present are carrying the same amounts of heat).

The force applied to an atom comes from the slope of the potential energy surface, meaning interatomic forces can be calculated for any pairwise potential by perturbing an atom and computing the potential energy for the pair of atoms:

$$F_{ij} = -\frac{dE_i}{dx} \tag{5.5}$$

For a multi-body potential however (where multiple neighbors are used to calculate the

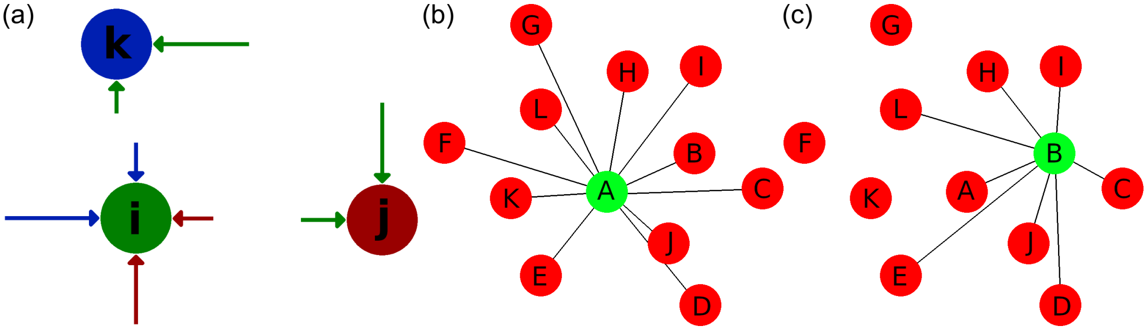

FIGURE 5.5: (a) For a 3 body potential (e.g., Stillinger Weber), by stipulating that $F_{jk} = F_{kj} = 0$, one may extract pairwise force interactions. (b) This is extendable to an arbitrarily-many body potential. While the forces between atoms B and C (for example) may not necessarily be zero, these atomic interactions will be computed later (c) once B is considered as the central atom.

potential energy for an atom), it may be unclear which neighbor is applying a force to an atom. For the Stillinger-Weber potential for example, triplets of atoms are considered, with the bond angle between an atom's two neighbors included. To address this, I made the assumption that the two neighbors do not apply a force to each other.

$$F_i = F_{ij} + F_{ik} \quad ; \quad F_j = F_{ji} = -F_{ij} \quad ; \quad F_k = F_{ki} = -F_{ik} \quad ; \quad F_{jk} = F_{kj} = 0 \tag{5.6}$$

where F_i is the net force on atom i, computed from perturbing atom i, and so on. While this stipulation is somewhat arbitrary, it does not violate the potential energy conditions of the interatomic potential and is thus valid. Other authors [44] have also applied the condition of $F_{ij} = F_{ik}$, however setting inter-neighbor forces to zero is easily extendable to many-body potentials with more than 3 atoms. Forces between atoms j and k may be non-zero, but these will be computed later, when atom j or k are considered the central atom and the identical procedure is followed. A visualization of the interatomic forces for 3-body and many-body is shown in Figure 5.5 as well.

In the calculation of SHF, the direction of forces and velocities can also be used to distinguish between the relative contributions of vibrations parallel and perpendicular to the interface. Note that I do not call these transverse and longitudinal modes respectively, as a phonon wavevector is not obtained by these calculations. While running SHF, I noticed a significant contribution of parallel modes to heat flux across the boundary. For this reason, I made sure the simulation cross-section was sufficiently large so as to not affect these modes.

I also used Procrustes Shape Analysis (PSA) for the quantification of crystalline disorder in a similar manner to Han *et al.* [143]. PSA is traditionally used as a quantitative comparison between arbitrary 3D shapes, and I applied this comparison to the tetrahedrons formed by each atom's 4 neighboring atoms and lattice sites in the diamond cubic crystal. The comparison was performed by first finding the time averaged position of each atom, and the four nearest neighbor atom positions. The Kabsch algorithm was used to calculate the rotation required to align the neighbor atom positions to a regular tetrahedron, and scaling was calculated from the mean squared distance of each point to the center. Once alignment of the neighbor positions to the perfect tetrahedral lattice positions was calculated, the Procrustes distance is calculated as simply the mean squared distance between points. This is a measurement of the local environment each atom sees, and can be used to find atoms of each class (interstitials, neighbors to voids, etc) in low disorder cases.

5.6 Simulation results

In the baseline system with no defects, I found a TBR of 16.2 m^2 K GW^{-1}. By adding defects to the silicon or heavy silicon sides, the TBR was reduced to 5.7 or 7.3 m^2 K GW^{-1} respectively. A comparison of the vDOS of both regions did not explain the difference in TBR. The "bulk" vDOS of both silicon and heavy silicon (calculated from the atoms centered between the baths and interface) did not substantially change following the addition of defects, aside from a slight difference in the sharpness of features (Fig. 5.6.a). When using the atoms in the first monolayer on either side of the interface, a slightly different density of states was observed, but again, no clear differences were seen between defected and pristine cases (Fig. 5.6.b). I also computed the area overlap between both bulk and interfacial vDOS [103, 126], which has been used as a metric to quantify elastic scattering.

TABLE 5.1: In rows 1-3, results for the three systems are shown (pristine, systems with defects added to either region), including the Thermal Boundary Resistance values and vDOS overlap between various monolayers. The values between rows are compared in the last two rows, providing a direct comparison between values for each simulation. Color-coding denotes whether the change in overlap follows the expected trend: green indicates the reduction in TBR is in line with the increase in vDOS overlap, while red indicates the opposite is observed.

	Simulation	TBR ($\mathrm{m^2\,K\,GW^{-1}}$)	Area overlap: (%)		
			±8 ML	±2 ML	±1 ML
1.	Baseline	16.2	42.8	48.2	57.3
2.	Defects in heavy Si	7.3	45.7	49.5	58.2
3.	Defects in Si	5.7	43.4	50.2	57.5
	row 2 - 1	-8.9	2.9	1.3	0.9
	row 3 - 2	-1.6	-2.3	0.7	-0.7

These results are tabulated in Table 5.1, however no clear trends could be seen. In some cases (e.g., monolayers half a unit cell from the interface) the vDOS and TBR followed the expected trend to a limited degree (only a ∼1.3% overlap difference between the baseline and defected heavy silicon cases, despite TBR being less than half). For other cases however (e.g., bulk vDOS or first monolayers adjacent to the interface) the expected trend did not hold (higher overlap when defects were added to heavy silicon vs silicon, despite having a higher TBR). Both of these factors suggested that changes in vDOS overlap from local structure and defects could not explain the reduction in TBR following irradiation.

Calculating SHF across the interface, the results are very similar to that of silicon / germanium, which has been studied before [121, 137]. A large group of modes between 12-13 THz were seen dominating heat flow across the interface (Fig. 5.6.c). This could be seen in all systems, with little variation observable between defected and pristine cases. Interestingly, this did not line up with features in either bulk DOS, however there was a population of modes seen in the interfacial DOS at these frequencies, suggesting these were modes which were largely isolated to the interface. SHF can also be integrated across ω, and plotted as an accumulated heat flux (Fig. 5.6.d). Plotting in this manner, I noted that $\sim$ 30% of the heat was carried across the interface by these interfacial modes in this 12-13 THz range. These modes dominate heat flow, despite these only being a minority of modes in the interfacial vDOS, and despite not appearing at all in either bulk vDOS.

Conversely, there were frequency ranges with substantial vDOS overlap (e.g., 2-7 THz) which did not contribute as substantially as those in the 12-13 THz range. This was the first clue that scattering (not just across the interface, but within either material) may be a factor. Silicon and heavy silicon have optical modes at 15-18 and 9-11 THz respectively, which may scatter to form the 12-13 THz interfacial modes. These modes, being the direct result of scattering, may thus carry an inordinate amount of heat. Meanwhile, phonons may exist within both materials at 6 THz for example, but differing wavelengths will mean scattering is still required for these modes to transmit energy across the interface.

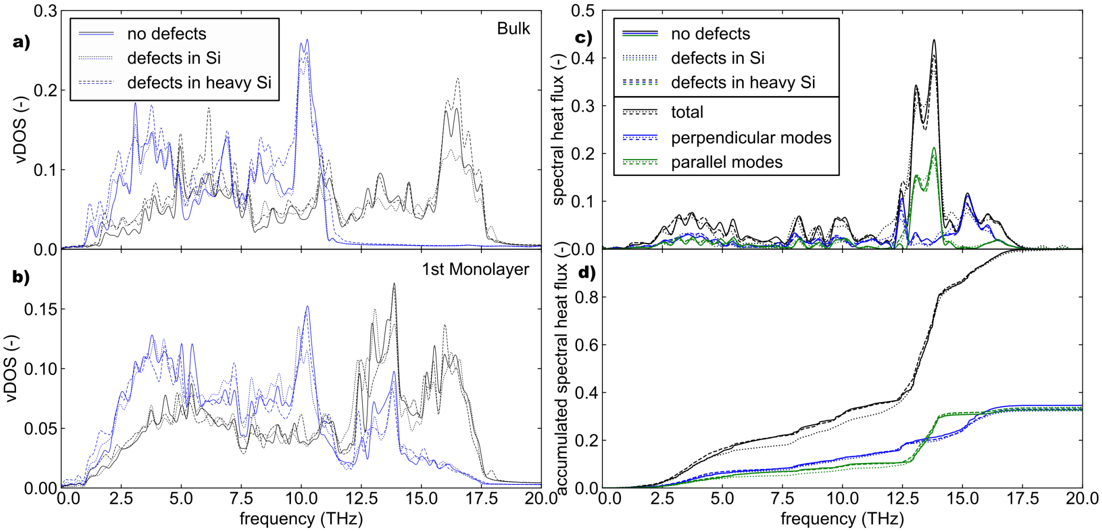

FIGURE 5.6: (a,b) Vibrational density of states (vDOS) describes the vibrations present within the simulation and (c) and spectral heat flux (SHF) describes the vibrations carrying heat across the interface. SHF is often presented as an accumulation (d) to allow determination of which modes dominate heat flow. Note that vDOS and SHF do not agree, suggesting that some modes have a disproportionately high contribution to heat flow. Critically, neither vDOS nor SHF show significant changes following the introduction of defects (solid lines vs dashed or dotted), and thus can not explain the reduction in TBR.

The disagreement between interfacial SHF and DOS (i.e., the modes carrying heat vs. the modes present) can also be explored by plotting the accumulation of both. Since vDOS can simply be calculated via a Fourier transform of atomic velocities, and since work can be calculated between any pair of atoms, both vDOS and SHF can also be calculated at arbitrary points within the simulation. This is shown in Figure 5.7, where I calculated vDOS and SHF in the bulk on either side, and at the interface. Within either material, DOS

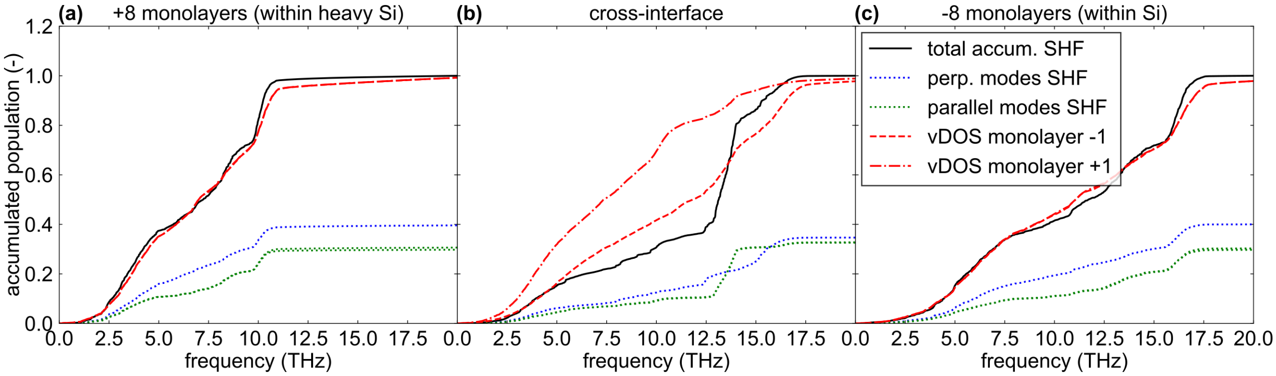

FIGURE 5.7: A direct comparison of accumulated Spectral Heat Flux (SHF) vs accumulated vDOS is shown. Within the bulk (a,c), all modes which are present (vDOS, red) also approximately-uniformly carry heat (SHF, black). The contribution of vibrations perpendicular to and parallel to the interface are also shown (blue, green). Near the interface (b), the SHF does not line up with either vDOS (implying that some modes do not carry heat, while other dominate heat flow).

lined up with SHF (meaning the modes which were present were approximately evenly carrying heat). At the interface however, only a subset of vibrations carry energy.

To explore the spatial variation of vDOS and SHF more rigorously, I calculated both for every pair of monolayers approaching the interface (Fig. 5.8). First examining SHF, I noticed some modes varying in intensity as the interface was approached. For example, modes between 5-15 THz were lower in magnitude on the silicon side as far as 2 monolayers from the interface. For vDOS (Fig. 5.8.b), a direct shifting in frequencies could be observed (e.g., with amplified 15 THz modes appearing adjacent to the interface). This suggests that there is a volume where interfacial modes thermalize into bulk modes. Within this thermalization region, scattering is required to couple the heat-carrying modes between the bulk regions and interface, and the presence of this region was direct evidence that scattering within the medium (not solely across the interface) occurs. If defects serve to enhance this scattering, better mode conversion would be expected, reducing the overall resistance.

I hypothesized that the size of this thermalization region may be related to the scattering rates for the given material. Qualitatively, the SHF transition distance was significantly larger on the silicon side (Fig. 5.8.a), in agreement with the notion that scattering times (or phonon mean free paths) should be higher in silicon. This may also explain the greater reduction in TBR when defects were added to silicon vs heavy silicon; if defects enhance the scattering within the material, enhancing the heat flow across the interface and reducing TBR, then this effect was reduced in heavy silicon where scattering rates are already high.

More quantitatively, I selected a narrow band of modes on vDOS (Fig. 5.8.b), and plotted the amplitude of the mode as a function of position (Fig. 5.8.c,d). The modes between 12.3-12.6 THz specifically showed an alternating behavior, where every other monolayer experiences this vibration, and the amplitude showed a clear decay moving away from the interface. Conceptually, if a standing wave exists with a wavelength of 4 monolayers, monolayers 1 and 3 are vibrating out of phase, while 2 and 4 act as vibrational nodes. This should not exist within bulk silicon, as every monolayer is compositionally and structurally identical; for every vibration moving monolayers 1,3,5,7..., the same mode will affect monolayers 2,4,6,8... and so on. Near an interface however, the interface may serve to amplify some modes while pinning others. This phenomena also appeared across a series of simulations, including differing domain sizes and conditions, and might be an interesting area for further study. This mode had a clear decay moving away from the interface, which I quantified by fitting an exponential function to its amplitude. I found a significantly faster decay in the defected simulations (1.7× decay constant between the baseline and defected silicon cases, Fig. 5.8.c,d), which supports the premise that scattering and thermalization were driving the change in TBR. This comparison of decay rates is possible with other frequency ranges, but few were as dramatic as the 12.3-12.6 THz range (which lines up with the dominant heat-carrying modes from SHF as well). Interestingly, the total heat carried by perpendicular modes was lowest at the interface vs within the bulk (Fig. 5.8.a, right-most intensity). This suggests that not only do the frequencies of heat-carrying modes change, but so does the direction of vibrational motion.

These observations further challenge the premise that the overlap of vDOS controls TBR. Instead, scattering within the material adjacent to the interface allows coupling between bulk and interfacial modes, which is a requirement for interfacial heat flow. Stated differently, just as the requirement to convert energy between bulk vDOS populations results in TBR under the traditional explanation, the additional conversion requirement within either medium results in additional thermal resistances if scattering mechanisms are limited.

In their study of amorphous vs crystalline interfaces, Gordiz and Henry [121] also commented on the somewhat counterintuitive relationship between the short mean free paths (MFP) within amorphous materials (leading to low thermal conductivities), and the low TBR across amorphous materials' boundaries. Within the context of mode conversion within the material adjacent to the interface however, this observation is no longer a surprise; if short MFPs are associated with high scattering rates and better conversion between vibrational modes, short MFPs will result in a lower overall TBR.

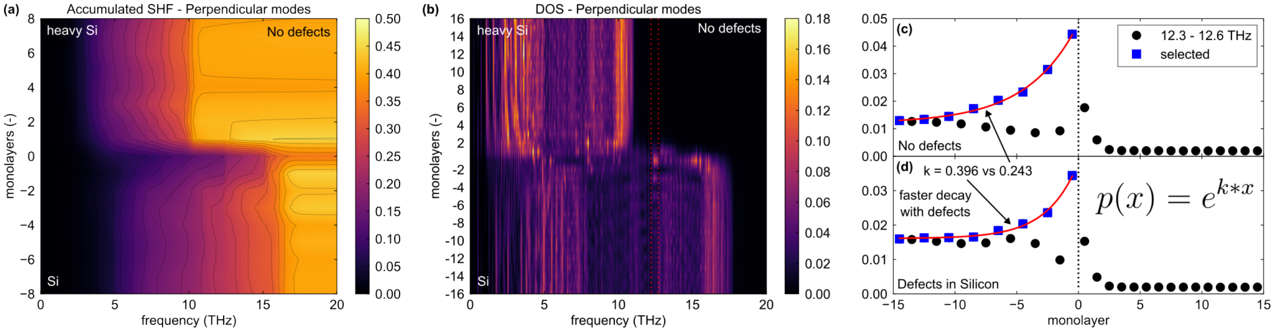

FIGURE 5.8: (a) Spatially-varying accumulated SHF is shown for vibrations perpendicular to the interface for the undefected case. This is effectively the blue curve from Figure 5.6.d, but across multiple imaginary cut planes within the simulation at varying distances from the interface. A "thermalization" region is visible on the silicon side, where the heat-carrying populations do not immediately switch from bulk to interfacial. I propose that the size of this thermalization region is related to scattering rates. In support of this, I noted that the thermalization region was larger on the silicon side as opposed to heavy silicon, as silicon is expected to have longer phonon mean free paths and lower scattering rates. (b) Similar spatially-varying thermalization effects are visible in vDOS, including an interesting standing wave (12.3-12.6 THz) in which every other monolayer appears to be vibrating. This should not exist within a bulk, and is likely a direct result of the interface. (c) I next fit an exponential curve to the decay of this mode moving away from the interface. Following the addition of defects, the decay is much steeper, implying an increase in scattering rates.

Finally, in an effort to understand the nature of the additional scattering as relating to the defects induced, I applied Procrustes shape analysis (PSA) to quadruplets of atoms in the simulation [143]. In PSA, one shape (the tetrahedron formed by a given atom's 4 nearest neighbors in this case) is compared against another (the tetrahedron found in a perfect lattice) via a series of translation, scaling, and rotation steps, with the mean square distance (between neighbor atom locations and tetrahedral vertices) computed. This is a relatively new technique when applied to molecular dynamics simulations, but can serve as a quantification of the localized disorder experienced by a given atom. Tracking the degree of scaling and rotation required to align the atoms to the tetrahedron can also yield insight into longer-range disorder (e.g., if a large number of atoms require a large rotation, this can be indicative of warpage of lattice planes).

Qualitatively, I began by simply visualizing the Procrustes distances for each atom (Fig. 5.9.a). While one would expect a high Procrustes distance (high localized disorder) for atoms immediately adjacent to defect sites, there was also a diminishing Procrustes distance for subsequent neighboring atoms. This implies that there are medium- and long-range effects, where atoms several interatomic-distances away still experience a distorted localized environment resulting from the defect.

More quantitatively, I plotted the distributions of Procrustes distances (Fig. 5.9.b) and the rotation angle (used for aligning tetrahreda, Fig. 5.9.c). For the undefected case (purple curve), all atoms had a Procrustes distance of less than 3×10^{-5}Å, implying a near-perfect crystalline structure. All atoms were where they should have been, the crystal was not strained or deformed, and non-zero Procrustes distances only resulted from the vibrational motion of the atoms. Note that I used the time-averaged atomic positions; thermal atomic vibrations are much larger than 3×10^{-5}Å, and a nonzero Procrustes value was merely the result of averaging over a finite number of timesteps. In the system with 2% defects however, Procrustes distances reached as high as 6×10^{-2}Å, with over 50% of atoms (far more than would be accounted for based on the number of added defects) reaching as high as 1.1×10^{-4}Å (higher than all atoms within the undefected case). This implies there was distortion of the lattice, even at a distance from the introduced defects, confirming the observation made by eye previously (Fig. 5.9.a). Furthermore, the angle of rotation or anisotropic scaling parameters used to align each quartet of atoms to a tetrahedral set of lattice sites were also high compared to the undefected case (Fig. 5.9.c). The pristine case saw a maximum rotation angle of 0.2°, while a 0.5° rotation for atoms was common in

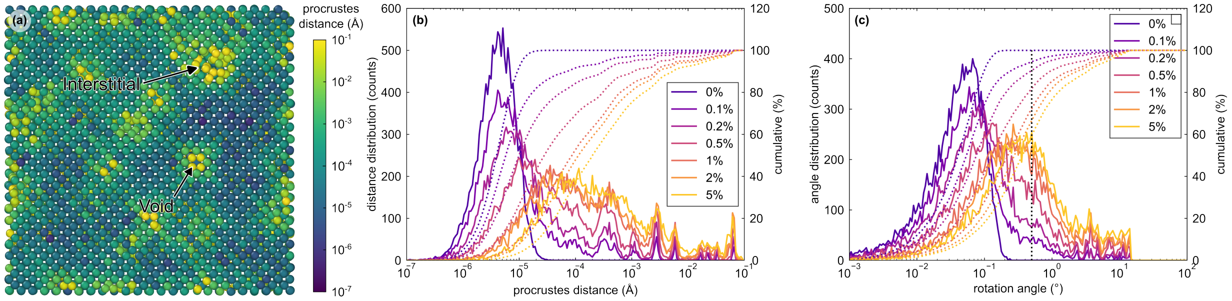

FIGURE 5.9: I computed the Procrustes distances for each atom (used as an indicator of the localized disorder seen by a given atom). (a) A colormap of Procrustes distances for a simulation with 2% added defects shows how Procrustes distances are associated with specific defect types. Voids are the most obvious, as an atom is merely missing. The structure associated with interstitials was far less consistent however, as the relaxation of the system causes multiple atoms to shift out of place. A damping of the Procrustes distance value can be seen for atoms moving away from the void however, indicative of medium- or long-range disorder. (b) A histogram of Procrustes distances is plotted (solid) for varying defect concentrations. All follow a roughly normal distribution, with peaks appearing which are likely associated with specific defect states. I also present the integration across these distributions (dotted). 50% of atoms in the 2% defects case had Procrustes distances of 1.1×10^{-4}Å or more, compared to the undefected case where all atoms were below 3×10^{-5}Å. In other words, a majority of atoms (far more than the nominal density of introduced defects) had a much more distorted local environment. The effects of the (relatively few) defects were not localized to the defects alone, implying the presence of medium- and long-range disorder. (c) rotation angle (used to align tetrahedra prior to computing the Procrustes distance) was also recorded, and similarly shows longer-range disorder effects.

the defected case (applying to $\sim$33% of atoms). This suggests there is warpage of atomic planes beyond merely strain (or anisotropic strain for a confined film). Interestingly, similar results were found for varying concentrations of defects (e.g., a simulation with 0.2% defects still yielded 26% of atoms with Procrustes distances above the 3×10^{-5}Å undefected maximum, or $\sim$10% of atoms with a $>0.5^\circ$ rotation angle).

These observations can further explain the experimental results. While localized defects may result from irradiation, additional short- and mid-range crystalline disorder may also be introduced (e.g., the warping of lattice planes around defects). This disorder may not directly affect the vDOS overlap, but it will increase scattering within the defected medium beyond that caused by the relatively low concentration of defects alone. This result is similar to experimental observations for ion irradiated materials [69], where the thermal conductivity is affected by scattering from the localized strain fields associated with defects, rather than the defects themselves.

Specific defect types can also be observed in the Procrustes distance histogram for the low defect concentration cases. The distribution of Procrustes distances for the undefected case was approximately Gaussian (since non-zero Procrustes distances simply result from atomic motion), however peaks at specific Procrustes distances began to appear as defects were added (or “stair-steps” in the accumulation curves). One would expect that all atoms associated with a particular defect type should have similar Procrustes distances (similar levels of localized disorder), and in theory this could be used to infer the defect concentration within the system (e.g., if defect recombination is occurring). For the case of Frenkel pairs, one would expect that there are $n\%$ interstitials, $4{\cdot}n\%$ interstitial neighbors, and $4{\cdot}n\%$ void neighbors for $n\%$ defects. Calculating the area under each peak does not necessarily yield consistent results however, indicating that at least in this particular case, the disorder environment is not necessarily as simple as one might assume.

Combining all observations, I have built a case for scattering (within the material adjacent to the interface) as playing a critical role in TBR. Considering vDOS alone, the overlapping density of states could not explain the reduction in TBR in the simulations. With interfacial SHF and vDOS, interfacial modes had a disproportionately high contribution of heat flux (and these modes resulted from scattering of optical modes within either system). Several ranges of modes in the bulk and interfacial vDOS also had substantial overlap, but did not significantly contribute to heat flow, suggesting that some other property of these vibrations (such as the wavevector) was prohibiting their transmission of energy without scattering. There was also a gradual evolution of vDOS and SHF approaching the interface, and the size of this region was related to the scattering rates within the system. This can be thought of as a thermalization region, where energy is converted between bulk and interfacial populations in order for heat to be transmitted across the interface. Procrustes disorder analysis also showed that relatively low levels of defects were sufficient to induce substantial disorder throughout the system, with defects affecting atoms many interatomic distances away (medium- and long-range disorder).

5.7 Relevant publications

This work represents an advance in our fundamental understanding of how heat transmits across interfaces, and has ramifications on engineered reductions of TBR via manipulation of crystalline disorder. This could be done via ex-situ irradiation or in-situ growth (e.g., isotopic disorder). The simulation advances (including stabilization of structural defects, spatial analysis, and Procrustes disorder analysis) also offer a path towards exploring the control of short and mid-range crystalline disorder, and could be used in a variety of applications. Using disorder as a mechanism for the control of thermal transport, coupled with the traditional methods (e.g., through vDOS overlap), could also lead to designer interfaces with user-defined phononic TBRs. The observation of the optical standing-wave modes is also exciting, and bears further study. The results from this study were published in Physical Review B (T. W. Pfeifer, H. T. Aller, E. R. Hoglund, E. A. Scott, J. A. Tomko, H. Ahmad, A. Doolittle, A. Giri, K. Hattar, A. J. H. McGaughey, and P. E. Hopkins; "Ion irradiation induced crystalline disorder accelerates interfacial phonon conversion and reduces thermal boundary resistance". Phys. Rev. B 109, 165421, April 2024, https://doi.org/10.1103/PhysRevB.109.165421).

Chapter 6

Phonon pumping in MD: Exploring the possibility of switchable Thermal Boundary Resistance

A key finding from the irradiated GaN study ("Measurement and simulation of the effects of irradiation on Thermal Boundary Resistance") was that scattering appeared to play a strong role in thermal boundary resistance (TBR). In other words, the ease by which one set of vibrational modes can be converted to another (interfacial modes thermalizing to bulk modes for example) controls the overall thermal resistance across the interface. This is in contrast to the traditional explanation, where the overlap between the vibrational density of states of either material (termed "vibrational mismatch") controls TBR. This finding was based on two observations: the addition of defects led to only negligible changes to vDOS overlap, and a minority of vibrational modes carried a disproportionately high amount of heat. For example, both silicon and heavy silicon had vibrational modes at 6 THz, but an insubstantial amount of heat was carried by these modes. I posited that the role of phonon wavevector may be responsible; a mode may exist on either side, but if the wavevectors do not match, scattering is still required to transmit energy across. Conversely, 12-13 THz interfacial modes (which directly resulted from the scattering of optical modes in either material) dominated heat flow, and the defects appeared to enhance scattering of these modes.

While the defects increased scattering rates across the spectrum, a means of increasing the scattering of specific targeted modes may be of value. If selectively increased scattering can be achieved, this might allow a reduction in TBR with only minimal impact to the thermal conductivity. One could either target those modes which did not carry a significant amount of heat previously, or those modes which already carry heat so as to amplify their contribution. Furthermore, if this could be done in a reversible or switchable manner, this could have a range of real-world practical applications.

I hypothesized that targeted increases to phonon scattering could be achieved through the application of an external field (magnetic, or electromagnetic via the application of light) so as to pump specific phonon modes out of equilibrium with the rest of the system, and that this should affect TBR.

To pursue this effect, I set up a series of simulations with an applied force field designed to couple to the phonon modes within the system. I then ran NEMD simulations to study how TBR changed due to the applied field. This is the last project in the second thrust of my work: “Advancements to computational techniques”.

6.1 Theory

When a field couples to a mode, there is a probability that the mode gains or loses energy to the field (or stated in the inverse: the field drives the mode or the field receives energy from the mode). This is the premise for a variety of experiments, including vibrational Electron Energy Loss Spectroscopy, where an electron beam can exchange energy with phonons within a sample, which can be used to measure vibrational populations.

When a phonon mode is selectively excited, it may be driven far out of equilibrium with the rest of the modes in the system. Scattering rates are also tied to a phonon’s population. This means the farther out of equilibrium a phonon is driven, the faster it will scatter with adjacent modes. Higher anharmonicity also results from higher atomic displacements (and this phenomena is responsible for the lowering of thermal conductivity at high temperatures in crystalline materials).

Combining these concepts, if one can apply a force field with an MD simulation, coupling to a specific phonon mode, that mode may be driven out of equilibrium, and scattering may be increased.

6.2 Basic simulation setup and validation

For this study, I chose to continue using the toy Stillinger-Weber silicon / heavy-silicon system so as to allow direct comparison to previous simulations. Phonons in Stillinger-Weber silicon are also well-understood and highly-harmonic (with low scattering rates, well-defined wavevector, and narrow linewidths), meaning targeted increases in scattering would be likely to have a large effect.

I ran two series of simulations for this study. First, I ran an NVE (constant number of atoms, constant volume, and constant energy) series consisting of a cube of 12 × 12 × 12 unit cells of silicon (28.0855 g mol^{-1}), with a singular field applied. The field followed a plane wave:

$$\overrightarrow{F}(x,t) = A \cdot e^{ik\cdot\overrightarrow{x} - i\omega\cdot t} \tag{6.1}$$

defined by the field amplitude A, wavevector k, and frequency ω. Note that the direction of the wave (controlled by position vector $\overrightarrow{x}$) is independent of the field polarization (controlled by the force direction vector $\overrightarrow{F}$). The directions used will affect coupling to phonons: If $\overrightarrow{x}$ and $\overrightarrow{F}$ are parallel, the field should couple to longitudinal phonons, whereas a perpendicular $\overrightarrow{x}$ and $\overrightarrow{F}$ should couple to transverse modes. All simulations were run using LAMMPS (Large-scale Atomic/Molecular Massively Parallel Simulator) [138] for 30 ns (15 million timesteps, with a 2 fs timestep size), and the field was applied via the LAMMPS "swiggle" command.

I also ran a series of NEMD simulations to explore the effects on TBR. These simulations consisted of a rod of atoms, 60 × 5 × 5 unit cells in size, with 30 unit cells of silicon (28.0855 g mol^{-1}) and 30 unit cells of heavy silicon (72.64 g mol^{-1}). Note that I differentiate this from a silicon / germanium system as I used the silicon potential for both materials in order to avoid any potential lattice mismatch effects. In traditional NEMD simulations, an NVE ensemble is used, and a hot and cold bath is applied (through an energy addition and subtraction on either end). The temperature drop across the interface is then used to calculate TBR, however more complicated analysis was required once the field was applied. In preparation for simulations with an applied field, the system was first equilibrated without a field, and a restart file was written. Each subsequent run with an applied field then used the same restart file, eliminating the need for repeated (and computationally expensive) equilibration.

I began by simply demonstrating the coupling between the applied field and phonon modes within the system. A temperature rise (measured as the total kinetic energy of the system in MD) should occur if the added force field couples to and excites a phonon mode. I ran a series of NVE simulations across a range of frequencies and wavelengths (one simulation per ω and k), and monitored the temperature increase (i.e., the energy added to the system), using the temperature increase as an indication that a phonon was present in the system at the selected ω and k. By sweeping through a series of values for ω at fixed k, I effectively probed a vertical slice across the phonon dispersion, and compared the results to the dispersion acquired from SED (Fig. 6.1).

Spectral Energy Density can be calculated using the following expression:

$$\Phi(\omega,k) = \frac{1}{4\pi\tau_f N_T}\sum_{\alpha}\sum_{b}^{B} m_b \left| \int_0^{\tau_f} \sum_{n}^{N} v_{\alpha,n,b}(t)\cdot e^{i\cdot k\cdot \bar{r}_{xyz,n,b=0}-i\cdot\omega\cdot t}\, dt \right|^2 \tag{6.2}$$

where index pairs n and b point to an atom based on the unit cell index (n) and the atom's index within the unit cell (or basis index b). The velocity of an atom at each timestep is thus $v_{\alpha,n,b}(t)$, in a given direction α. $\bar{r}_{xyz,n,b=0}$ denotes the time-averaged position ($\bar{r}$) of the atom's unit cell (n, for b=0) in a given direction (xyz, corresponding to a given Brillouin zone direction). This expression is effectively a coherent sum over atoms within a given basis index b (e.g., all odd atoms for a crystal with a diatomic basis), meaning all atoms at the given index in the basis must agree as to the phase of the wave, and destructive interference may occur if a subset of atoms are out of phase with another subset of atoms. Meanwhile, there is incoherent summing across indices in the basis (odd vs. even atoms for example) and polarizations (the direction of atomic displacements α), meaning the sum is taken after the phase information is removed. There is no phase cancellation between waves on differing basis indices (i.e., if odd atoms and even atoms are vibrating out of phase, as is the case with optical modes, these do not destructively interfere). As a brief side-note, fast computation of the above expression can be performed using fast Fourier transform algorithms (e.g., Python's numpy FFT) by noting the expansion of the exponent:

$$\Phi(\omega,k) = \frac{1}{4\pi\tau_f N_T} \sum_{\alpha} \sum_{b}^{B} m_b \left| \int_0^{\tau_f} \sum_{n}^{N} v_{\alpha,n,b}(t) \cdot e^{i\cdot k\cdot \bar{r}_{xyz,n,b=0}} \cdot e^{-i\cdot\omega\cdot t} dt \right|^2 \tag{6.3}$$

where a Fourier transform is defined as:

$$\mathscr{F}[f(t)] = \int_0^{\tau_f} f(t)\cdot e^{-i\omega t} dt \tag{6.4}$$

therefore the expression for SED can be rewritten via an FFT as:

$$\Phi(\omega,k) = \frac{1}{4\pi\tau_f N_T} \sum_{\alpha} \sum_{b}^{B} m_b \left| \sum_{n}^{N} \mathscr{F}[v_{\alpha,n,b}(t)\cdot e^{i\cdot k\cdot \bar{r}_{xyz,n,b=0}}] \right|^2 \tag{6.5}$$

Interestingly, when the force field was applied to every atom within the system, only acoustic modes appeared. Optic phonons can be thought of as alternating atoms vibrating out of phase with respect to one another, meaning a force which is accelerating (adding energy or amplifying the vibrations) for even atoms will be simultaneously decelerating (removing energy, or suppressing the vibrations) for odd atoms. Optics modes thus appear only when the force is applied to alternating atoms. This same phenomena appears in SED calculations as well. SED can be calculated with the atomic basis is ignored (and all atoms

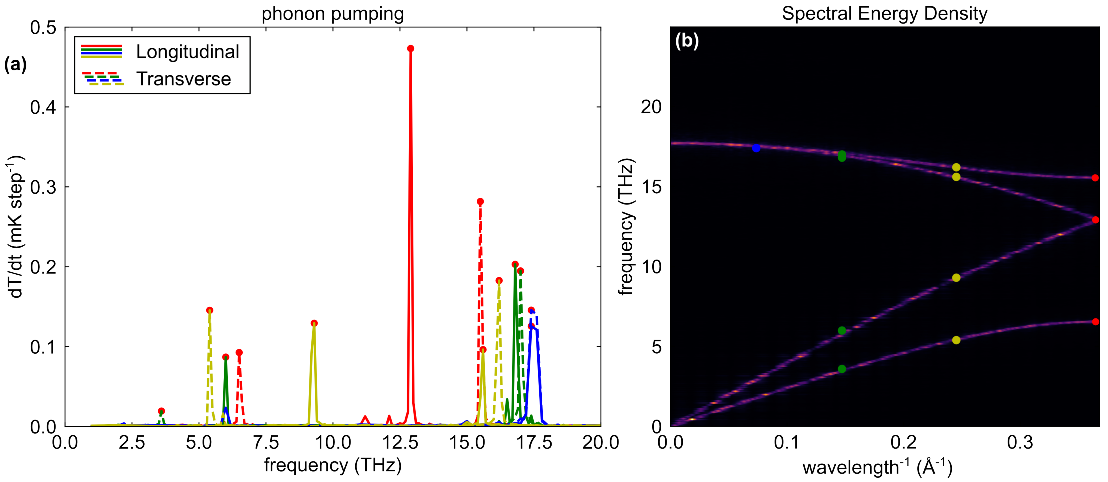

FIGURE 6.1: By applying a sinusoidal force field (in space and time) within a molecular dynamics simulations, specific phonon modes can be excited. (a) a series of simulations are run at four selected wavevectors across many frequencies. The system heats when the applied field is coupled to a phonon mode. Comparison of this to the spectral energy density (SED) calculation (b) can be used as validation that this is the result of phonon coupling.

are summed together, with phase cancellation allowed):

$$\Phi(\omega,k)=\sum_{\alpha}\left|\int_{0}^{\tau_f}\sum_{n}^{N}v_{\alpha,n}(t)\cdot e^{i\cdot k\cdot \bar{r}_{xyz,n}-i\cdot\omega\cdot t}dt\right|^{2} \tag{6.6}$$

with n now simply referring to the atom index. This yields complete destructive interference of longitudinal optic modes in the [100] direction (interference between the modes on alternating bases) within the first Brillouin zone, and partial destructive interference for transverse optic modes. Instead, these LO phonons appear “unfolded” in the second Brillouin zone. This is shown in Figure 6.2. There is also a fading effect for the TA and TO phonons, as there is only partial destructive interference.

As a slight side-note, similar results can be obtained through summing eigenvectors from Lattice Dynamics. For each wavevector k, the eigenvector calculated for each frequency ω and basis index b is a complex 3D vector. This denotes the atomic displacements, in 3D, with the real and imaginary components denoting the phase of the wave. By simply summing the eigenvectors across the basis (across b, allowing cancellation, where the eigenvectors at a given ω,k for the basis indices may be equal and opposite), similar unfolding can be observed.

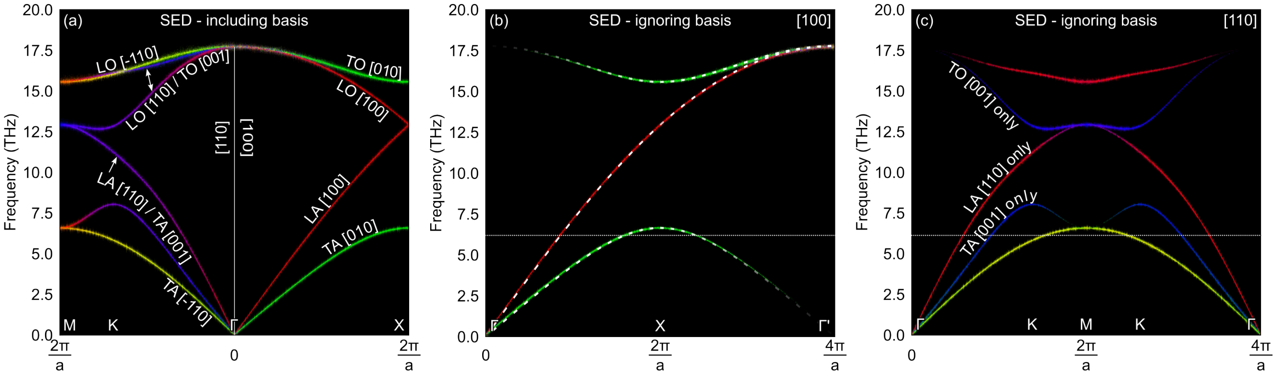

FIGURE 6.2: (a) I performed SED calculations for silicon on a diatomic basis (incoherent summing across the two atom basis) in [100] (Γ-X) and [110] (Γ-K-M) directions. Color denotes longitudinal modes (red), transverse in-plane modes (yellow), and transverse through-plane (z-direction, blue). Color mixing (i.e., blue+yellow=green, or red+blue=violet) indicates degenerate or mixed-polarization branches. When all atoms are summed coherently, an "unfolding" of the phonon branches occurs, shown for (b) the [100] (Γ-X) and (c) [110] (Γ-K-M) directions. Coherent summing in Lattice Dynamics (b, white dashed) shows the same effect.

6.3 Simulation setup for excitation effects on TBC

Having demonstrated the ability to directly couple an arbitrary force field to phonon modes within the system, I next explored the impact of the applied field on TBR. Within the NVE simulations, a continually-increasing system temperature was used as an indication for field-phonon coupling, however a long run at constant temperature is desired for NEMD TBR simulations. Time-averaging is required in typical NEMD, as temperature fluctuations within the system can yield large variations in the instantaneous temperature profile and resulting calculated TBR. The desire for coupling to phonons (thus heating the system) and a constant temperature system (for time-averaging) are fundamentally at odds.

I thus considered three basic simulations configurations. In a traditional non-equilibrium molecular dynamics (NEMD) simulation, TBR is calculated from the temperature drop at the interface and the heat flux across the system according to $R = \Delta T/Q$. The value for heat flux is typically taken directly from the positive and negative energy baths applied on opposing ends of the simulation volume. A linear fit is applied to a portion of both halves of the system (termed “leads”) to avoid error resulting from the rounding-off of the temperature vs position profile at the interface. NVT (typically with the Nose Hoover thermostat) is not typically used, as it can introduce unphysical effects, affect thermal populations and extracted properties, and lead to undesirable temperature fluctuations [144–148]. Since heat would be added to the system by the force field however, I attempted a series of simulations using NVT temperature baths, effectively pinning the bath temperatures in place and allowing removal of the field-generated heat. I included a “buffer” layer in the system, comprised of a thin slab of the opposing material, in an effort to insulate the system from any unphysical effects from the baths (shown in Figure 6.3.a).

In an alternate configuration, I simply removed the hot bath and corresponding buffer layer and applied heat using the field alone. In this scenario, the field was only applied where the bath was previously (Fig. 6.3.b). Since the heating rate and thus the heat flux is directly tied to the coupling to the phonons however, it was a challenge to obtain a reliable flux across the system once ω and k were varied. A similar issue occurred with the previous method as well, as excessive heat flux could mean heat flowed “backwards” in the lead into the hot NVT bath. Thermal resistance across the buffer layers also meant a large temperature differential was needed.

Instead, I simply ran traditional NEMD simulations and adjusted the applied field amplitude so as to minimize the temperature rise. I targeted an average temperature of 300 K with a $\pm$ 5% temperature drop across the interface (285-315 K). For the phonon-pumped simulations, results were excluded if the maximum temperature in the system exceeded 400 K (over the span of 10 ns: 5M timesteps at 2 fs each). If a larger temperature rise was observed, I either reduced the applied field amplitude or excluded the runs from the results. I was also primarily interested in the effect of the applied field on the scattering and thus the TBR, so I did not wish to simulate a highly out-of-equilibrium system. While simulations of the effects of instantaneous excitation on TBR would be interesting [149], I considered these to be beyond the scope of the study.

I also used several strategies for selecting ω and k for the excitation field. I began by

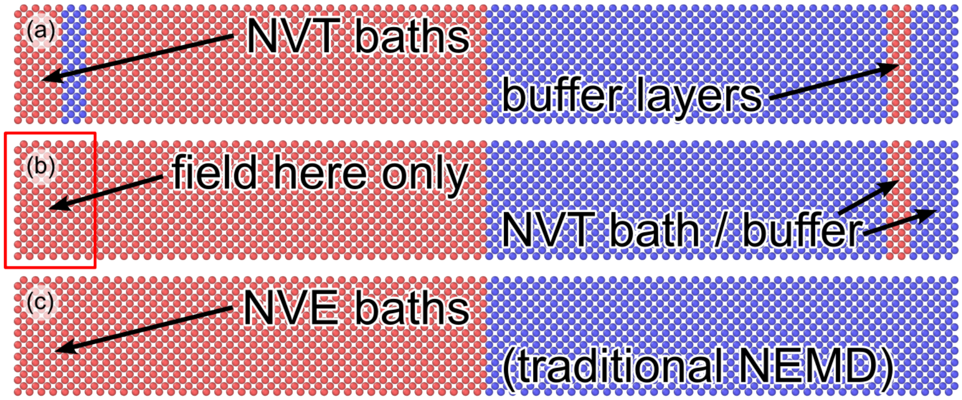

FIGURE 6.3: To manage the temperature rise resulting from the sinusoidal field / phonon interactions, (a) an NVT ensemble can be used to pin the traditional NEMD temperature baths at a fixed temperature. Buffer layers are added to mitigate any potential unphysical effects from the thermostat. (b) The field itself can be used instead of the hot NVT bath. (c) traditional NEMD with an NVE ensemble can also be used, assuming the field amplitude is low enough to minimize the temperature increases.

running SED and SHF on the initialized structure (seen in Figure 6.4). Since the wavevector resolution is dependent on the simulation dimensions, the SED dispersion is not as crisp as those seen in Figure 6.2, however this is representative of the modes present in the system (3N modes along a given Brillouin zone direction for N atoms in that direction). Both silicon (upper) and heavy-silicon (lower) dispersions can be seen, along with a stripe across all values of k around 13 THz. Non-wavelike modes (random vibrations) or modes which are highly localized (only existing at a specific location) will appear as poorly defined in k. Notably, the degree of localization will also affect the spreading in k. By including or excluding specific unit cells near the interface for the analysis, I confirmed this stripe was due to semi-localized interfacial modes near the interface. The gradient in intensity across k may simply be indicative of the degree of delocalization (e.g., low-k long-wavelength modes being poorly defined for a highly-localized region) or may be due to the absence of low-k optical modes in silicon and heavy-silicon for scattering. This band of localized modes also lines up with the dominant heat-carrying frequencies in SHF, confirming that these interfacial modes play a key role in heat exchange across the interface.

I tested several strategies to enhance scattering to drive thermalization between bulk

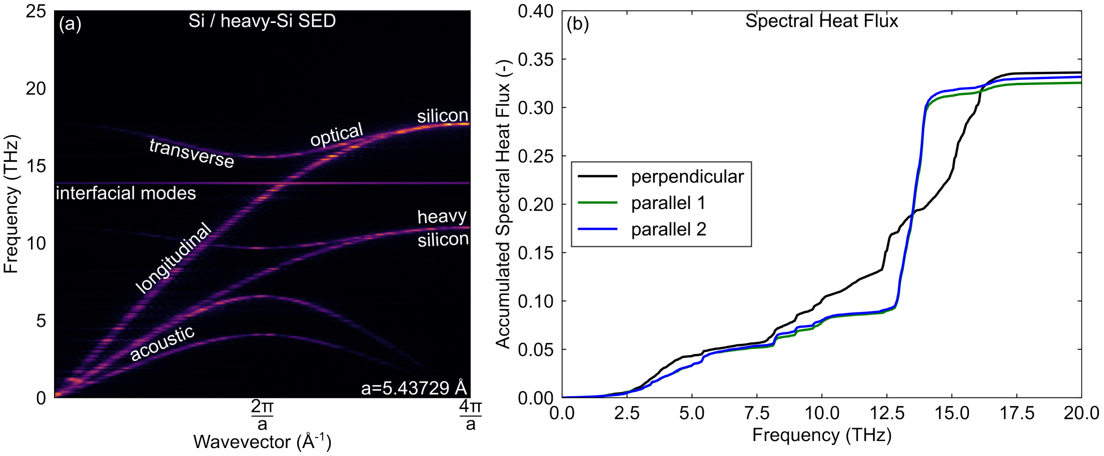

FIGURE 6.4: (a) SED calculations over the entire silicon / heavy-silicon system detect interfacial modes across all k around 13 THz, which lines up with the dominant heat-carrying frequencies in SHF (b). SED and SHF was used to guide the selection of modes to excite: individual modes in either (or both) materials can be targeted, or a phonon bridges might hypothetically be established by exciting at many ω,k values between pairs of branches

and interfacial modes. In the simplest case, one could select a single ω and k to target bulk or interfacial modes. This can be done either directly (at the ω and k of an existing phonon), or by selecting ω,k immediately off-branch (inside the line-width of the branch). One might also set up a series of simultaneously-applied fields to excite a range of ω,k values, either running along a branch or between branches. Exciting a branch may serve to increase scattering for the entire branch (as opposed to pumping a single mode far out of equilibrium), while a range of modes between branches might serve as a form of phonon "bridge" to encourage the conversion of energy between branches. When attempting to excite a range of modes, I considered three strategies for managing the maximum temperature rise during the course of the simulation. If the temperature was found to increase too quickly, the modes closest to the branches (most likely to contribute to excessive heating) could be excluded. Alternatively, the field amplitude at all ω,k could be uniformly reduced, or a non-uniform reduction could be applied based on proximity to the branch. I ran numerous simulations for the single-ω,k and ω,k sweep conditions, however an exhaustive search was computationally prohibitive.

6.4 Analysis methods

In traditional NEMD, the temperature drop across the interface is measured, and the heat flux (known from the energy applied to the baths) is used to calculate the TBR according to $R = \Delta T/Q$. A system in which the field applies a net heat flux to the hot or cold side may yield a larger or smaller temperature drop respectively, solely due to the changing heat flux across the boundary. In other words, if the temperature of the cold side is elevated by the applied field, a smaller ΔT will be observed. This means the traditional method of extracting TBR is insufficient.

Instead, I began by computing the flux applied by the force field as a function of time and position (Eq. 6.7). The work applied to each atom is simply the force field intensity vector $\overrightarrow{F}(x,t)$ dotted with the velocity vector for each atom, $\overrightarrow{v}_a$, and work can then be summed over all atoms a at each position (or within a chosen spatial window).

$$q_{applied}(x,t) = \sum_a \overrightarrow{F}_a(x,t) \cdot \overrightarrow{v}_a \tag{6.7}$$

Once the applied energy is calculated as a function of position (Fig. 6.5.a), the flux across any arbitrary slice plane (including across the interface) can be found from the sum of flux added to all previous points, i.e., from the integral of applied energy:

$$Q(x,t) = \int q_{applied}(x,t)dx \tag{6.8}$$

and the discretized resistance between arbitrary monolayers can be calculated from the temperature distribution (Fig. 6.5.b):

$$R(x,t) = \frac{dT}{dx}\frac{1}{Q(x,t)} \tag{6.9}$$

The resistance associated with an interface typically exists over a finite region near the interface (note the round-off temperature drop region adjacent to the interface in Fig. 1.5). This appears as a region of differing layer-wise resistances using the approach outlined here (and can be seen in Fig. 6.5.c). Similarly, the treatment of nanoscale resistances on a continuum basis is imperfect (note the presence of negative local resistivity values in Fig. 6.5.c). For this reason, TBR should be found by summing over the resistance associated with multiple monolayers. The size of the region selected may affect the resultant TBR (just as selection of the region to perform a linear fit for both regions will affect the TBR in traditional NEMD), so consistency is required for comparing across multiple simulations.

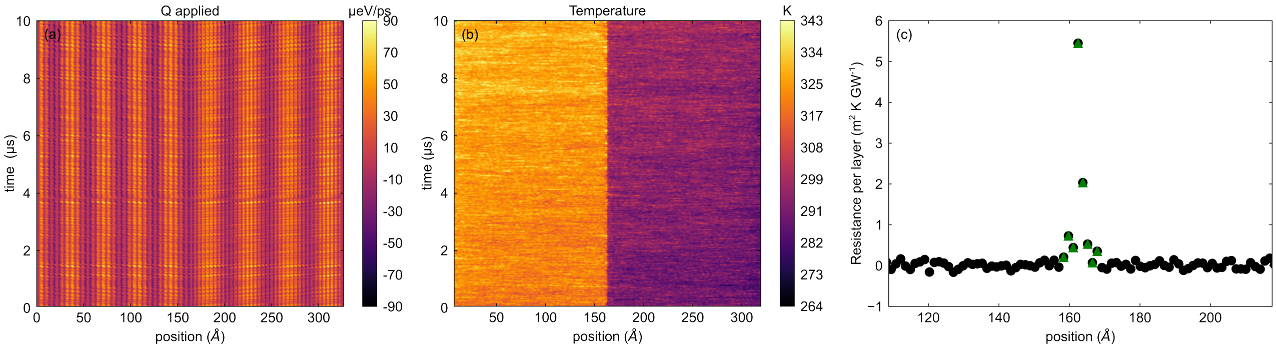

FIGURE 6.5: (a) The spatially- and temporally-varying energy flux, as applied by the sinusoidal force field, was calculated based on atomic forces and velocities. (b) The spatially- and temporally-varying temperature was logged during the MD simulation. (c) These were used to calculate a layer-wise resistance, which enables the extraction of the TBR.

6.5 Results and discussion

A subset of all scenarios explored is shown in Figure 6.6.a. None of the situations explored conclusively showed a substantial reduction in TBR which could be attributed to selectively increased scattering. The baseline case (without an added field) saw a TBR of 10.24 ± 0.20 m^2 K GW^{-1} (with the standard deviation calculated across multiple simulations with differing velocity initialization seeds). Most values for TBR with the added field were within this range. Several simulations showed lower TBR values (e.g., a reduction to ~ 7 m^2 K GW $^{-1}$ for those bridging between LA or LO branches), however these simulations rose to ~400 K over the course of the run. A similar reduction was found by merely elevating the system to 400 K (Figure 6.6.b), implying that this reduction was not from selectively enhanced scattering from the phonon pumping, but merely an overall increase in temperature. Another simulation showed a reduction to 5 m^2 K GW $^{-1}$ (optical modes near the traditional Brillouin zone edge), however this came with a temperature increase to upwards of 1000 K.

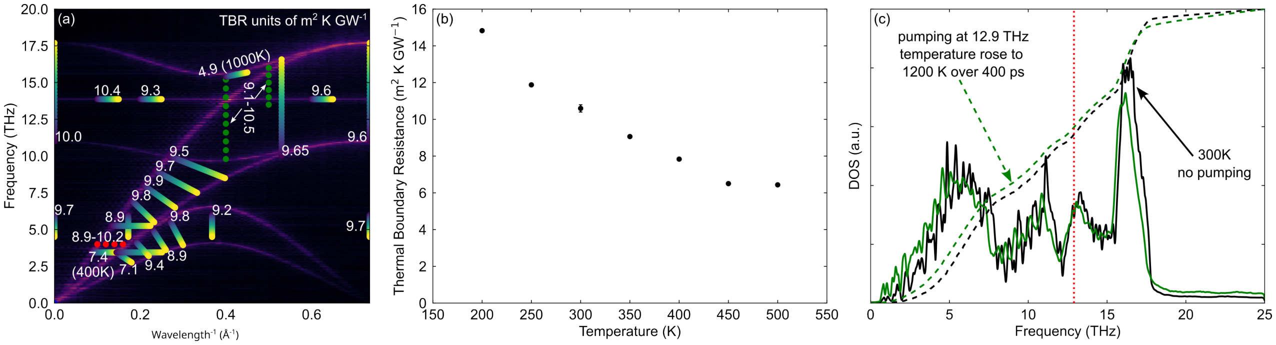

FIGURE 6.6: (a) The results for a selected subset of phonon pumping simulations are shown overlaid on SED. Graded lines denote simulations where a range of ω,k were excited, along or between branches. Red and green points denote excitation at a singular ω,k, with the force applied in x and y directions respectively, so as to excite longitudinal vs. transverse modes. (b) Traditional NEMD was also performed at elevated temperature to avoid conflating pumping effects vs simple heating effects. (c) Vibrational density of states is compared for non-pumped and pumped cases (solid). To avoid effects of noise in the signal, the integrated density of states (dashed) is also shown. No detectable increase in out-of-equilibrium population can be seen at the pumped frequency (12.9 THz, red dotted), and the only effects are from the increase in temperature. This was the simulation with the highest temperature rise (highest point in Fig 6.1).

In hindsight, these results should come as no surprise, as there are fundamental problems with the premise of this study. While I successfully showed the coupling between the applied field and specific phonons within the system, these over-pumped phonons quickly equilibrate with other phonons within the system. Phonon-phonon scattering times are typically on the order of picoseconds. We see this during an ultrafast laser experiment; while electrons may selectively couple to specific phonon modes, the phonon population is considered to be in thermal equilibrium within tens of picoseconds, and a two-channel thermal model (capturing electron and phonon temperatures) can often show satisfactory agreement with data [150–152]. Despite the field coupling to specific modes, the end effect was simple heating of all phonons within the system, no different from an applied energy flux or a simulation at elevated temperature. In fact, when the vibrational density of states was compared between field-pumped and non-pumped systems, no non-equilibrium differences could be observed. In Fig. 6.6.c, I show the vDOS for the NVE simulation with the highest temperature rise (corresponding to the 12.9 THz longitudinal peak in Fig. 6.1). No features in the vDOS (or integrated across ω, dashed lines, to avoid the influence of noise) can be seen at 12.9 THz. Instead, the only differences were from broad-spectrum thermal effects; the system was simply hotter. If the field was able to push specific modes out of thermal equilibrium, features in the vDOS should be visible for the out-of-equilibrium mode, but this is not the case.

While I was unable to simulate quasi-steady-state (slow temperature rise) out-of-equilibrium phonons (where specific modes are over-excited), the simulations run and lessons learned may yet serve to guide future simulations. Transient simulations (where the system is rapidly pushed out of equilibrium and then allowed to relax) may be of interest in a variety of fields. Electron energy loss spectroscopy simulations can be performed by considering the electron wave's propagation through a thermally-populated MD system, however the electron's effect on the thermal population is neglected. Similarly, electron beam damage is dominated by thermal effects (where highly-localized rapid heating can cause breakdown of a sample), and simulations of these phenomena would be interesting. Finally, researchers have performed "tuning fork" experiments where a wave packet is introduced into a system. These are typically done at low or zero temperature, with instantaneous displacements applied, to allow for observation of the propagating resultant wave. A similar procedure could be performed to map scattering pathways: a strong force field might briefly overexcite a phonon mode, and time-dependent SED analysis might be used to observe the evolution of the populated dispersion afterwards.

Chapter 7

Using thermoreflectance to detect surface defects

Having expanded the realm of measurements using existing thermoreflectance techniques, and with irradiation-induced damage fresh in mind, I next explored whether thermoreflectance could be used as a detection tool for defects. Focused Ion Beam (FIB) milling is a process in which a high energy ion beam is directed at a sample, and material is removed through a sputtering process [153, 154]. This is used in the preparation of Transmission Electron Microscopy (TEM) samples, or for the creation of fiducial marks on samples. One might expect a small area of damage surrounding the milled region to occur however. Several authors [155–157] have looked at redeposition effects, where the expelled material may return to the sample and coat any exposed surfaces with a thin layer of amorphous target material. Amorphization of the TEM sample is also a concern, as the glancing-angle irradiation from the ion beam will cause structural damage (knock-on damage within the sample) [158, 159], and similar damage may also occur in the original sample from which the TEM sample was cut. Similarly, the introduction of gallium from the ion beam has also been studied [160–162].

In a series of samples received from collaborators however, I observed inconsistent results in thermal measurements at distances of $>$100 µm from FIB-milled fiducial marks.

For the mechanisms mentioned, only the gallium contamination has been identified as affecting the sample to this extent. This gallium contamination was also identified via Secondary Ion Mass Spectroscopy (SIMS) [160], which is a destructive measurement.

I thus sought to understand 1) the exact nature and cause of the FIB damage observed on the preliminary sample set, and 2) if thermoreflectance experiments might be capable of detecting damage in a non-destructive manner. If the concepts from thermoreflectance experiments can be used for the detection of these surface effects, this would present an opportunity for greatly accelerated characterization of damage from FIB or other processes where sample damage may be a concern. This is the first project under the third thrust: "Development of new experimental metrologies".

7.1 Experimental design

I designed a study in which a series of 10×10 µm square holes were Focused Ion Beam (FIB) milled (Helios UC G4, dual-beam, using 30 keV Ga^+ ions) into single-crystal silicon wafers (University Wafer, [100] orientation, nominal RMS roughness of < 5 nm). One sample set was milled with constant current / varying dose (by varying the exposure time), and another was milled at constant dose / varying current (by increasing the exposure time as the current was decreased). Duplicate samples were prepared for some irradiation conditions, to allow measurement of samples with and without the aluminum transducer. Note that while the ion beam can be used for imaging the sample (similar in operation to a Scanning Electron Microscope (SEM)), this was avoided, as I did not want to conflate the irradiation effects of imaging vs. FIB milling. Following milling, aluminum was deposited on some of the samples in preparation for thermoreflectance measurements. Prior to aluminum deposition, our usual cleaning procedure was used (sonication in DI water, isopropanol, acetone, and methanol for 5 minutes each, drying via compressed atmospheric air, and O_2 plasma cleaning for 10 minutes). For samples measured without the transducer, measurements were performed both before and after surface cleaning.

7.1.1 Thermoreflectance

I performed TDTR on all samples with aluminum, in order to assess the effects of irradiation damage on thermal properties. I considered the possibility that FIB milling could affect both the bulk thermal conductivity of the substrate (via deeper irradiation effects) or the thermal boundary resistance between aluminum and silicon. Note that TDTR is somewhat insensitive to the the exact location at which a resistance occurs, meaning the resistance of films of up to tens of nanometers are often lumped into the TBR [163, 164]. This means the TDTR measurements of TBR could be sensitive to surface effects (contamination or bonding at the Al / Si interface), redeposition effects (a thin film of expelled material on the surface of the substrate), or near-surface irradiation effects (shallow disorder affecting the near-interface thermal conductivity).

I also collected SSTR data over the samples, again taking advantage of the low acquisition times of SSTR to collected maps [132] extending > 1 mm from each hole. For the uncoated samples, the magnitude of the pump-induced changes in reflectivity can not be directly correlated to temperature changes, as electronic carrier effects can also contribute [27, 165–167]. For this reason, the ability to analyze thermal properties will depend on the magnitude of the temperature vs. free-carrier reflectivity response, along with the relaxation times of these excited carriers [27]. Instead, I simply explored whether the raw reflectivity (R) and reflectivity-normalized pump-induced changes in reflectivity (dR/R) could qualitatively monitor surface changes. This also provides a comparison of the sensitivity of photo-modulated reflectivity measurements vs. reflectivity measurements, for detecting changes in crystal quality and defects.

7.1.2 Electron microscopy

In an effort to understand the effects of possible crystalline and chemical disorder introduced by the FIB processes, I collected atomic-resolution Scanning Transmission Electron Microscopy (STEM) images, and used Energy-Dispersive X-ray Spectroscopy (EDX) to gain insight into the chemical composition. All images presented are High Angle Annular Dark Field (HAADF), where the brightness of the image is proportional to the atomic mass of the species present. Note that since preparation of the TEM samples involves the use of a FIB, care must be taken to separate the effects of the initial milling (the goal of the investigation) vs. any effects from the TEM sample preparation. Even when a platinum protective layer is deposited prior to milling, laterally straggling ions can still enter through the face of the milled cut, perpendicular to the ion beam. For this reason, it is common for TEM samples to contain small amounts of gallium [168] regardless of the original sample composition. I thus consider all STEM and EDX results to be comparative in nature; no conclusions may be drawn from a single milled sample (e.g., from the presence of gallium or disorder), and the samples should instead be evaluated against each other.

7.1.3 Profilometry

In order to explore the effects of FIB milling on the surface topology (e.g., if expelled target material redeposits on the sample surface), I used stylus profilometry to map the surface near one of the milled holes. I used a Bruker DektakXT profilometer with a 6 µm radius spherical tip, which affects the resolvable minimum feature size. Due to environmental vibrations present, noise appeared in the profilometry signal at a higher spatial resolution than physically measurable given the radius of the tip. To account for these effects, data was smoothed using a 1 µm wide ($1/e^2$ radius) Gaussian blurring function prior to quantifying the surface roughness. Spatially-varying surface roughness was then calculated using a rolling 20 µm window, starting at 30 µm from the center of the FIB hole.

7.1.4 Time of flight secondary ion mass spectroscopy (TOF-SIMS)

Finally, time-of-flight secondary ion mass spectroscopy (TOF-SIMS) was performed to quantify the surface concentrations of gallium present. TOF-SIMS is a destructive measurement technique wherein the sample is irradiated, secondary ions are ejected from the sample surface, and the time of flight to a detector is recorded. The time of flight is roughly proportional to the mass of the ejected molecule and inversely proportional to the charge. Under ideal cases, TOF-SIMS is capable of measuring ppm or hundreds of ppb concentrations, however the presence of sample contamination (e.g., complex hydrocarbons with a similar mass to the species of interest) may complicate analysis [169]. These measurements use Bi^+ ions as the primary ion (30 keV energy, 30 nA current), with a beam diameter of $\sim$ 5 µm, and milling to a depth of $\sim$ 5 nm per pass. A calibration is required to relate the number of collected ions (for a given time-of-flight, related to a given mass and charge) to the concentration of that species, so I used EDX data on gallium concentration from the FIB-adjacent measurements to obtain approximate concentrations from TOF-SIMS. Multiple consecutive TOF-SIMS measurements may also be stitched together, however care must be taken to note the order in which the measurements were taken. Since TOF-SIMS is destructive, surface features may be missing in subsequent measurements.

7.2 Results and discussion

7.2.1 Profilometry

Profilometry showed no significant differences in surface roughness of the samples between pre- and post- FIB milled samples, regardless of location with respect to the FIB marks (all $<$ 5 nm RMS). The only measurable surface feature is a small raised rim surrounding the FIB hole, as high as 60 nm and tapering back down over a distance of $\sim$ 30 µm. (Fig. 7.1). This suggests there may be a small amount of redeposition, where expelled material may return to the surface of the sample (in approximate agreement with the findings of Vermeij *et. al.* [157]). This occurs over a limited area however (or is below the measurement capabilities of profilometry beyond this 30 µm region).

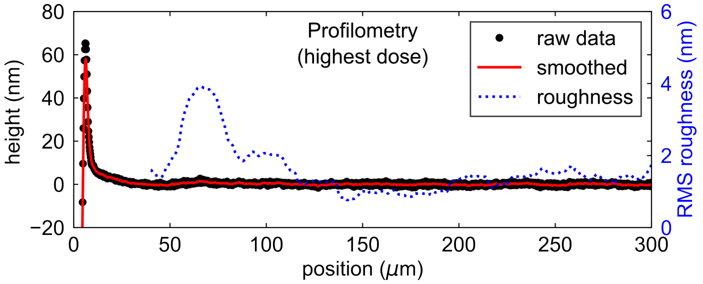

FIGURE 7.1: Profilometry shows the presence of a small rim around the FIB hole (60 nm tall by 30 μm wide). There is also a small secondary feature at ∼ 60 nm from the center, however this only registers as a ∼ 4 nm RMS surface roughness, which is in line with other regions of the sample.

7.2.2 Pump-Probe Thermoreflectance

Collecting TDTR data at varying distances from the FIB-milled holes, the fitted Thermal Boundary Resistance (TBR) between the Al transducer and Si substrate appears to be affected out to ∼ 300 μm in the highest-current / highest-dose case (9.3 nA, 17 nC, 3 minutes exposure). The fitted thermal conductivity of the substrate was also affected, but this was much more localized to the area immediately surrounding the milled hole, suggesting the primary longer-range effects are surface-level or near-surface. Interestingly, changing the exposure time (thus changing the dose) appeared to marginally affect the magnitude of TBR changes, but had little effect on the spatial distribution of measured TBR. For samples milled at a lower current (430 pA) but with a comparable dose (requiring significantly longer exposure times), a significantly smaller region was affected. These results can be seen in Fig. 7.2. Uncertainty was calculated via contour analysis [25] in order to separate effects of changing thermal conductivity and changing TBR, however the nominally-fitted values maintain the trend out to ∼ 300 μm.

Using SSTR on the highest-dose sample (9.3 nA, 17 nC, 3 minutes exposure), I found an affected region of a similar size (Fig. 7.3.a,b), although no fitting was performed (since irradiation has the potential to change both the silicon thermal conductivity and aluminum / silicon TBR, and SSTR traditionally fits for one unknown). Agreement between TDTR and SSTR with the aluminum transducer is expected however, as both techniques are largely sensitive to variations in the thermal boundary resistance between the aluminum and silicon.

Examining the corresponding uncoated sample (same current, same dose) via optical

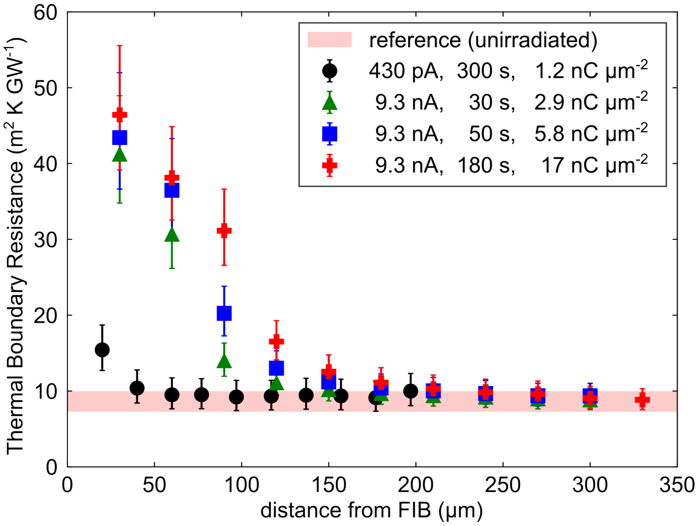

FIGURE 7.2: Silicon was FIB milled, an aluminum transducer was deposited, and the Al/Si TBR was measured at varying distances from the FIB hole. Three samples were milled at the highest beam current (9.3 nA) for varying durations (green, blue, red). These samples showed a similar damage profile extending away from the milled hole, with the dose affecting the magnitude of damage to some degree. Another sample (black) was milled at a lower current (430 pA) for significantly longer, reaching a dose of nearly half the lowest high-current sample. The resulting damage profile was quite different, with damage isolated to immediately adjacent the FIB hole.

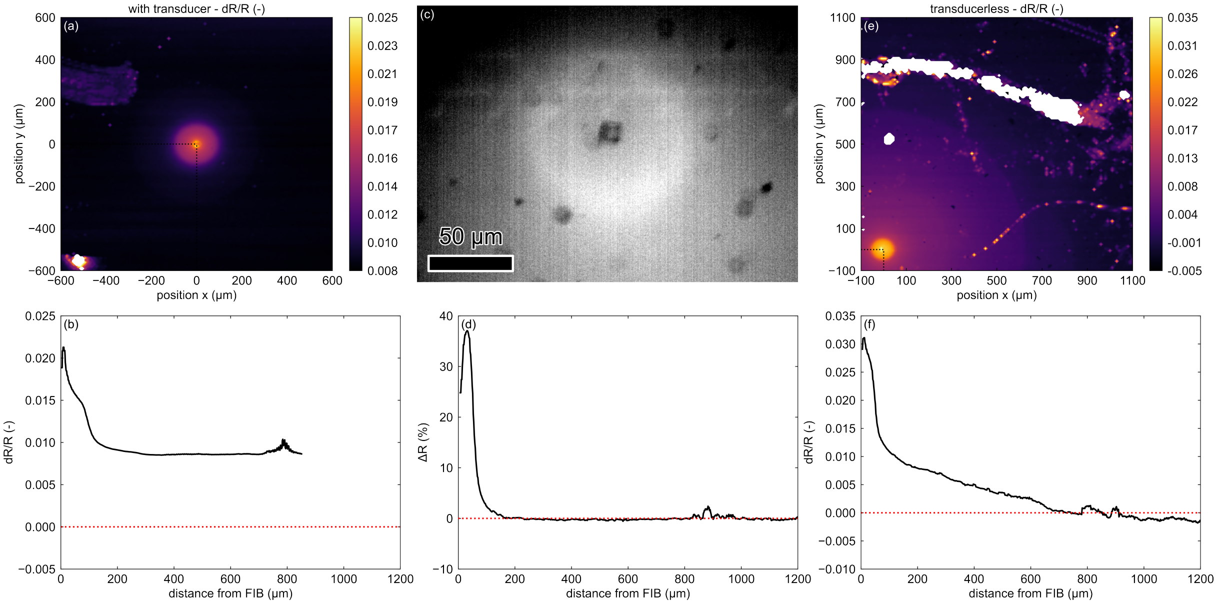

FIGURE 7.3: SSTR maps were collected on the area surrounding a 10 µm square FIB hole. (a) I mapped the raw SSTR thermoreflectance signal on the aluminum-coated sample, and (b) present a linescan of the signal magnitude. The largest effects are $<$ 50 µm away, however the thermoreflectance signal does not level off until $\sim$ 300 µm. (c) Optical microscopy on an uncoated sample shows an affected region out to $\sim$ 50 µm, meaning optical microscopy is insufficient for observation of these longer-range effects. (d) The raw reflectivity signal on the same sample is in agreement with the optical microscopy. (e) The map of the raw SSTR thermoreflectance signal on the uncoated sample and (f) linescan both reveal irradiation effects beyond $\sim$ 1 mm.

microscopy, an ion-affected region was only visible out to 50 μm or less (Fig. 7.3.c). Using SSTR, the raw reflectivity signal shows a similarly-sized region as well (Fig. 7.3.d). This suggests that optical microscopy is insufficient for finding irradiation-induced defects or surface damage, given the far larger region where the thermal properties are affected. Considering the pump-induced changes in reflectivity (*dR/R*) on the uncoated sample however, milling effects can be seen out to $\sim$ 1 mm. This is significantly farther than expected (Fig. 7.3.e,f), and was consistent before and after surface cleaning.

In the case of TDTR and SSTR (with transducer), the experiment is well-enough understood so as to attribute the changes (out to $\sim$ 300 μm) to deviation in thermal properties. The thermoreflectance signal is indicative of temperature changes, and can either be directly linked to thermal properties via thermal modeling (as with TDTR), or qualitatively linked to thermal resistivity changes (for SSTR in the case of too many unknowns). In the transducerless experiments however (with changes in the signal out to $\sim$ 1 mm), this is not the case. The signal is not purely thermal, as pump and probe photons directly interact with the electrons in the silicon, since the bandgap of silicon (1.12 eV) is less than both the pump and probe wavelengths (1.84 and 1.58 eV respectively, or 637 and 785 nm wavelengths). A transition between a thermally-dominated and electronic-effects -dominated regimes may also explain the change in the sign of the dR/R signal (seen in Fig. 7.3.f) [27, 170]. While these photon-electron interactions occur in aluminum as well, excited electrons equilibrate within tens of picoseconds. This is due to the metallic electronic structure of the aluminum and resulting high electron-phonon coupling that is typical in metals relative to non-metals. This means the electronic-effects can be safely ignored at these modulation frequencies when the transducer is used [167]. The transducerless measurements should also be considered to be volumetric, due to the finite optical penetration depth in the silicon by the pump and probe beams (637 and 785 nm wavelengths respectively).

7.2.3 Electron Microscopy

While the thermoreflectance results showed changes to the sample beyond the 50 µm region visible by eye, the exact nature of these changes was still unclear. In order to explore this further, I performed high-resolution EDX and atomic-resolution STEM imaging on the highest-dose highest-current sample (9.3 nA, 17 nC, 3 minutes exposure) at varying distances from the FIB hole.

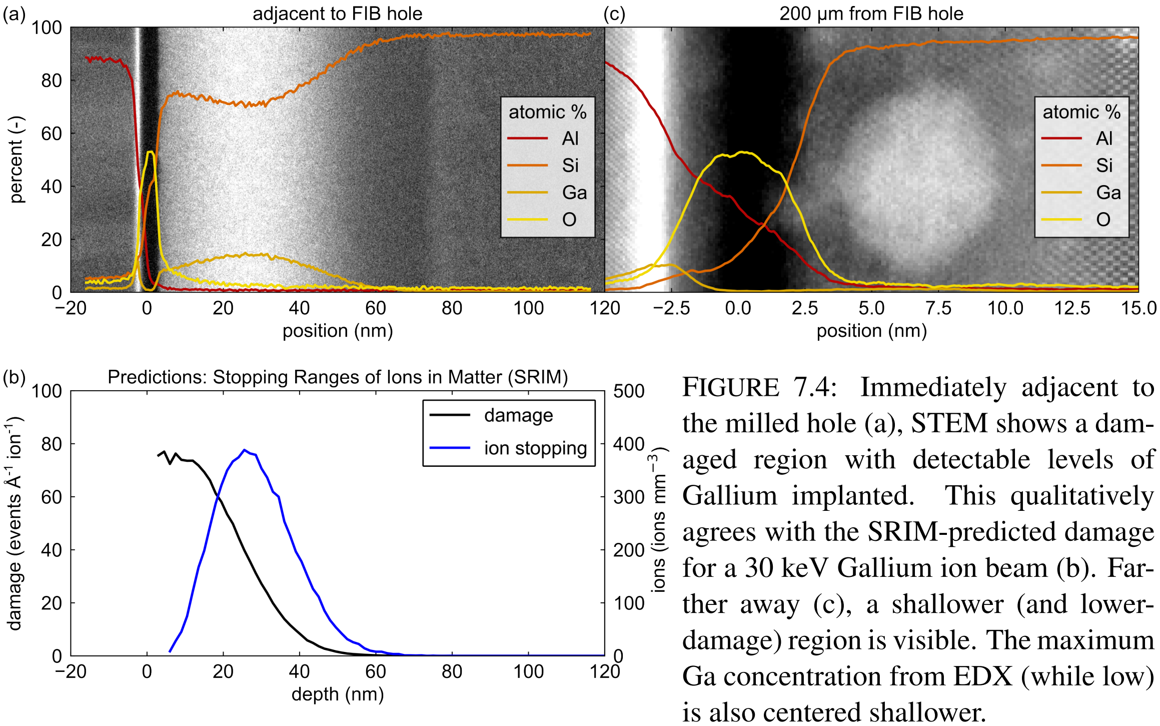

FIGURE 7.4: Immediately adjacent to the milled hole (a), STEM shows a damaged region with detectable levels of Gallium implanted. This qualitatively agrees with the SRIM-predicted damage for a 30 keV Gallium ion beam (b). Farther away (c), a shallower (and lower-damage) region is visible. The maximum Ga concentration from EDX (while low) is also centered shallower.

Immediately adjacent to the hole, a 70 nm deep region of disordered silicon was visible (Fig. 7.4.a). This is in qualitative agreement with predictions of irradiation damage (Fig. 7.4.b, using the Stopping Ranges of Ions in Matter (SRIM) simulation software [68]) for Ga^+ ions at 30 keV, suggesting that ions were straying outside of the focused beam itself and beyond the milled region. Farther from the hole (∼ 200 µm), a shallower disordered region (∼10 nm) was found, with less disorder (Fig. 7.4.c). A native silicon oxide / aluminum oxide layer is also present between the aluminum and silicon, although this is observed on unirradiated silicon as well. Similarly, there is an accumulation of gallium between the aluminum and silicon, but this is a normal result of TEM sample preparation, where gallium atoms are expelled from aluminum. Note: in Fig. 7.4.c, the large bright-intensity region in the middle of the image is likely copper contamination resulting from TEM sample preparation (as the TEM specimen is mounted on a copper grid), which is also common in TEM/STEM experiments.

The presence of shallower disorder farther from the FIB hole suggests exposure to lower energy ions, and the lower level of disorder suggests a lower dose. Within a beam of charged particles (ions), the particles should repel each other, resulting in a natural tendency for the beam to spread. Similarly, if there is a spectral distribution of ion energy within the beam [171–173], one might expect the lower energy (slower) ions to be spread to a greater degree. This hypothesis is also supported by the initial TDTR results (Fig. 7.2). With fewer ions in the beam at any one time at 430 pA vs. 9.3 nA, less beam spreading should be expected. Indeed, even with a proportionally longer exposure time (so as to achieve a comparable dose), the size of the affected region was dramatically reduced when milling was performed at the lower current.

With crystalline disorder visible in TEM at 200 µm from the FIB mark, the thermal results were thus far understood; crystalline disorder affects the near-surface thermal conductivity (and potentially the TBR). The question remained however, whether this crystalline disorder extended farther out, and why the irradiation effects were only measurable by directly pumping/probing the silicon.

Additional TEM samples were prepared at $\sim$ 500 µm and $\sim$ 1 mm from the FIB mark. There were no discernible differences in the images (Fig. 7.5), with no detectable loss of crystallinity, and EDX was unable to differentiate between the samples. Some ions and crystalline imperfections may still be present, but they are below the detection limit for STEM+EDX. For STEM, this may be understood by considering the viewing of atomic columns in transmission; a void in a column of 100 atoms would appear as only a 1% change in intensity in the image, and a lone interstitial would have 1/100th the intensity of an atomic column. EDX also requires the collection of a sufficient number of x-ray

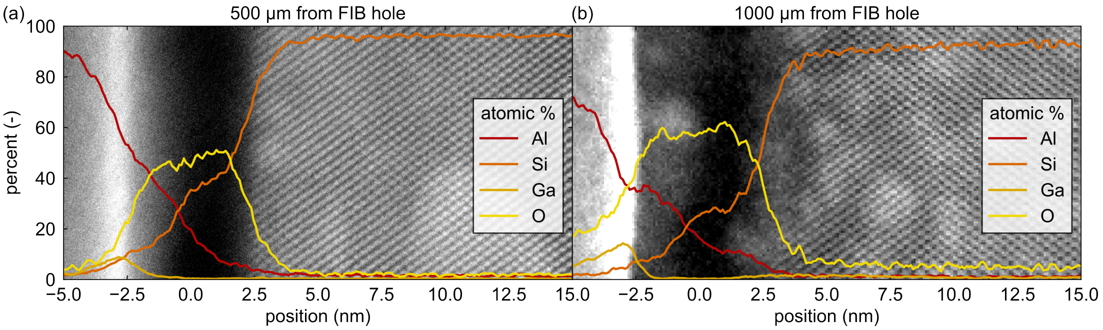

FIGURE 7.5: STEM+EDX is shown ∼ 500 µm and ∼ 1 mm away from the FIB hole. In the 500 µm case, no clear evidence of irradiation is found in the STEM+EDX data, despite clearly being present in the thermoreflectance data. Comparing the 500 µm and 1 mm images, there is no clear difference that would indicate one was subjected to a higher level of irradiation. I believe irradiation-induced doping effects are responsible for the pump/probe signal seen out to ∼ 1 mm.

scattering events to form a spectrum, and differentiating atomic concentrations of less than 1% would require prohibitively long collection times.

Considering the possibility of doping effects however [165–167], it should be noted that extremely low concentrations of dopants are able to have a substantial effect on the electronic properties of semiconductors. As a point of reference, doping concentration of 1×10^{17} dopants cm^{-3} is enough to affect the electron mobility by a factor of two [174], despite this translating to only a thousandth of a percent dopant atoms (based on the atomic density of silicon of 5×10^{22} atoms cm^{-3}). This level of dopants would be impossible to see via STEM or EDX, and would not be enough to affect the thermal properties [70]. We can however expect that slight changes in carrier concentrations in the material would affect both the pump absorption and the pump-induced reflection [175, 176]. If the intensity profile of an ion beam can be considered approximately Gaussian, then even if the ions in the Gaussian tails are of low energy and incredibly low in number, a direct optical-pumping optical-probing measurement may still be able to detect them.

7.2.4 TOF-SIMS

Finally, time-of-flight secondary ion mass spectroscopy (TOF-SIMS) was performed to quantify the surface concentrations of gallium present. An initial series of scans was

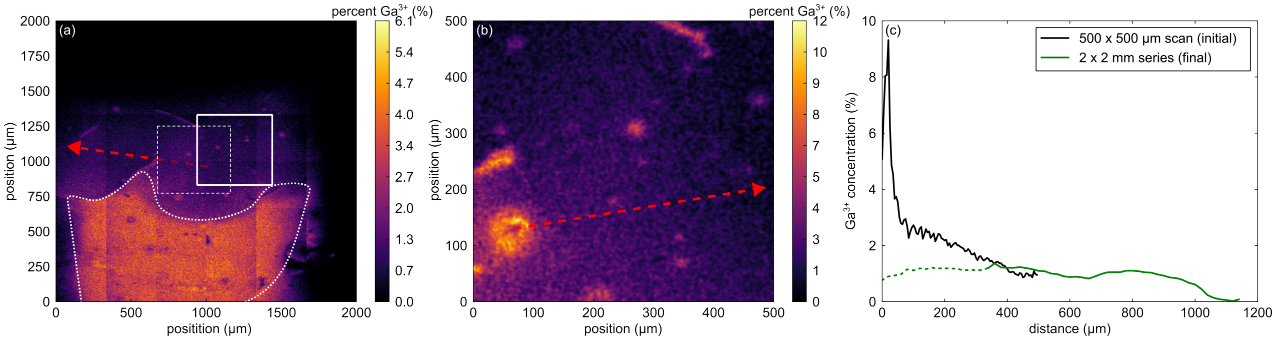

FIGURE 7.6: TOF-SIMS was performed over several 500 × 500 μm scan regions, and subsequently over a 2 × 2 mm field of view through a series of smaller acquisitions. The 2 × 2 mm field of view is shown in (a), and the preliminary smaller scans are shown in white and white dashed. A large region of contamination is also visible (dotted white), which complicates analysis. For the initial 500 × 500 μm area (b), a clear gradient in concentration of Ga^{3+} is visible leading away from the FIB mark. Using the FIB-adjacent EDX data to provide an approximate calibration, I estimate a $\sim$ 1% concentration at 500 μm from the FIB location (c). Using the 2 × 2 mm field of view sample, I estimate this Ga^{3+} extends out to at least 1 mm before reaching the sample edge

collected, rastering an area of 500 × 500 μm, and I used the FIB-adjacent EDX Ga^{3+} data as a calibration for ion concentration. Data was subsequently collected over a 2 × 2 mm field of view through a series of smaller scans. This data can be seen in Fig. 7.6. In the initial 500 × 500 μm scan (Fig. 7.6.b), a decaying Ga^{3+} signal is observed, reaching concentrations on the order of 1% at 500 μm from the FIB milled hole (Fig. 7.6.c). This trend qualitatively matches the results from the transducerless pump-probe experiments, confirming the spreading of ions during milling. Within the 2 × 2 mm field of view scan series (Fig. 7.6.a), the decay in the Ga^{3+} concentration near the original FIB hole is no longer visible. Since TOF-SIMS is a destructive measurement, and since these scans were taken later, one can infer the Ga^{3+} detected by earlier scans was primarily isolated to the surface (e.g., first $\lesssim$ 10 nm). For data outside of the areas previously measured, the Ga^{3+} decay continues out to or beyond 1 mm before reaching the sample edge. Analysis of TOF-SIMS data is also complicated slightly by the presence of mobile surface contaminants [169]. Areas of suspected surface contamination are shown dotted in Fig. 7.6.a. Surface contamination is expected here, as these samples were exposed to atmosphere for several months between fabrication/pump-probe measurement and the acquisition of TOF-SIMS data.

Combining the findings from the various measurements, I showed that the FIB milling process introduced defects in samples over a far larger region than expected (out to ~ 1 mm), and evidence points to this being due to spreading of the ion beam itself, with lower energy (slower) ions being pushed the farthest outside of the beam. This can be seen in the comparison of thermal data under varying-dose and varying-current conditions, noting that low ion current milling did not produce as dramatic an effect. STEM and EDX also showed a shallower affected region in STEM images at intermediate distances, supporting the premise of lower-energy ions in the beam tails. The farther-range effects are not visible in STEM or EDX, nor are they detectable thermally, however a direct pump/probe scheme was able to detect them. TOF-SIMS was also able to confirm the presence of Ga^{3+} ions extremely far from the milled holes. The ability to detect these concentrations through optical pump-probe experiments is likely due to doping effects from the low-dose irradiation, allowing measurement of the "tails" of an approximately Gaussian beam profile.

7.3 Relevant publications

These finding have ramifications on the use of FIB milling in sample preparation, either for milling or creating fiducial marks, as the surface of the sample is affected far beyond what might be expected or optically observable. Care should be taken to avoid taking measurement too close to a FIB mark or trench, as these measurements might be unreliable if the surfaces modifications noted here impact the measurements performed or properties of interest. The current-dependence of beam spreading also provides actionable recommendations on mitigating irradiation-induced damage with FIB, if irradiation effects are a concern.

The ability of the established thermoreflectance techniques to detect irradiation damage is also noteworthy, as the relatively simple CW pump/probe lock-in detection scheme may be a useful tool for qualitative measurement of surface-level defects. This measurement scheme shows a detection threshold that exceeds other techniques, and is also non-destructive (a benefit over other tools such as secondary ion mass spectroscopy).

The results from this study are currently under review in the journal Advanced Engineering Materials (T. W. Pfeifer, E. R. Hoglund, Anton V. Ievlev, and P. E. Hopkins; “Thermoreflectance detection of point defects resulting from focused ion beam milling”. Submitted January 21st 2025).

Chapter 8

Microscale calorimetry: Measuring enthalpy of phase change

So far, I have shown the use of (and variations upon) the traditional thermoreflectance techniques - TDTR [15], FDTR [16] and SSTR [17] - to determine properties that would otherwise be difficult to measure. These projects have all related to thermal transport however (thermal conductivity and thermal boundary resistance). The measurement of latent heat associated with a phase change represents a major gap in the world of nanoscale thermal metrologies.

The measurement of latent heat (e.g., enthalpy of fusion for a solid-liquid phase transition, h_f) is critical for the development and study of phase change materials, but is traditionally performed on mg to µg samples using Differential Scanning Calorimetry (DSC) [177]. In these measurements, two chambers are slowly heated (one containing a sample, one left empty). The energy input and temperature are carefully monitored, allowing extraction of heat capacity and latent heat. At high temperatures, analogous measurements can be performed using rapid electrical discharge [178, 179] or inductive heating [180]. In these experiments, thermal isolation of the sample is critical, as any substantial (or unquantified) conductive or radiative heat flow during melting will lead to error in the calculation of h_f. Electromagnetic levitation [181, 182] has thus been used to mitigate the effects of conductive heat flow.

The ability to measure the latent heat associated with phase changes on the micro- and nano- scales will be key for materials development where bulk synthesis of new materials may not be feasible however. Similarly, while size effects have been well-studied in the area of nanoscale heat transfer (e.g., boundary scattering affecting the phonon thermal conductivity), little research has been done to exploring size effects on latent heat, despite nucleation effects having a clear impact on the onset of solidification [183–185].

To address this gap, I have developed the analysis tools necessary for extraction of latent heat from laser-based non-contact optical pump/probe experiments. This is part of the last thrust of my research "Development of new experimental metrologies".

8.1 Principles of operation and basic theory

For a sample under constant heating or cooling, a phase change may be observed as a brief thermal arrest (i.e., there is a brief period of time where the material is at an approximately constant temperature as the material transitions between phases). If the sample environment is fully insulated, the heating contributes solely to changes in the internal energy of the sample (i.e., enthalpy, h). Before or after the phase change, the temperature rise defines the heat capacity (neglecting thermal expansion, $C = \frac{dh}{dT}$). During the phase change however, increasing the internal energy instead contributes to the rearrangement of atoms, and the change in internal energy between states is the latent heat. For a transition between liquid and solid states (i.e., melting or solidification), the latent heat is also termed the "enthalpy of fusion" h_f. In this chapter, I primarily focus on melting and solidification, however the principles discussed may be applicable to any phase change, assuming adequate measurement sensitivity can be achieved.

When using lasers for heating, the laser induces a localized transient temperature rise, leading to melting. Subsequent removal of the laser heating (or lowering its intensity) will then yield a resolidification and thermal arrest. Qualitatively, the duration of this thermal arrest is related to the latent heat associated with the phase change, with a high latent heat resulting in a longer thermal arrest. With accurate thermal modeling, one should theoretically be able to account for radiative and conductive thermal transport, thus mitigating the requirement for thermal isolation of the sample (and minimizing its associated uncertainty), and allowing the extraction of the enthalpy of fusion. The use of laser heating eliminates the need for a crucible or other form of containment of the melt, allowing measurements of the enthalpy of fusion at high temperatures (e.g., self-contained measurements of tungsten up to 4000 K) or measurements at microscales (e.g., thin films).

At high-temperature, pyrometry can be used to monitor the changes in temperature, and numerous high-power laser-pumped pyrometry experiments [186–189] have shown data capturing the melting/resolidification signature. Most authors use the resolidification plateau as a calibration to link the measured temperature ($T_{radiance}$), emissivity (at the pyrometer wavelength, $\varepsilon(\lambda)$), and the melting temperature (T_{melt}). Manara *et al.* [186] used the melt signature to characterize the enthalpy of fusion, by tracking the melting temperature as a function of pressure. A single dataset should be adequate to extract this information however, based on the size of a single resolidification plateau. Certain features of the published datasets also remain unexplained, such as why the melting signature (upon the initiation of laser heating) is often not visible whereas the resolidification plateau is obvious (upon removal of laser heating). I thus developed and applied an analysis scheme to pyrometry data collected on the same apparatus used by Manara, Barraza, and Milich [186–189]. I examined data on bulk tungsten (T_{melt} = 3695 K) and bulk molybdenum (T_{melt} = 2896 K), demonstrating the extraction of enthalpy of fusion (and other experimental parameters) from existing data.

At low temperatures, lock-in detection is required to account for low magnitude pyrometry or thermoreflectance signals. In SSTR, the magnitude of the locked-in thermoreflectance signal is proportional to the temperature rise, meaning temperature changes can be inferred (with scaling factors applied based on physical phenomena such as photodetector sensitivities, losses through optics, and the thermoreflectance coefficient of the sample surface). I have thus modified an SSTR apparatus at UVA to achieve higher temperature perturbations, in order to acquire melting data. I used this apparatus for proof-of-concept measurements on a wax-based PCM, with aluminum on a glass slide serving as the transducer.

8.2 Experimental Setup

8.2.1 Pyrometry

In the pyrometry-based experiments [186–189], a 2 kW laser (1064 nm wavelength) was used to heat a sample inside an enclosed environmentally-controlled chamber (1.5 bar argon, to mitigate oxidation effects), while pyrometers were used to record the temperature rise as a function of time. The laser was focused to a $\sim$ 3.5 mm diameter beam with an approximately top-hat intensity profile (uniform intensity across the area of the beam). A high-speed pyrometer (collecting at 663 nm wavelength) collected temporal data over a 0.8 mm field of view in the center of the sample. Relatively large laser spots were used (as compared to typical thermoreflectance experiments, with spot size on the order of microns) in order to avoid steep temperature gradients within the sample (leading to mechanical strain, and affecting the pyrometer measurement). Multiple experiments were performed until repeatable results were obtained. This avoided effects due to evolution of the sample or apparatus over consecutive measurements (e.g. oxidation of the sample, changes in sample surface following resolidification, evaporation of metal vapor onto the viewing window, etc). The schematic for this apparatus and an example data set are shown in Figure 8.1.

Two strategies are available to convert from the radiance temperature (measured) to the true temperature of the sample. In the simplest case (used for the tungsten data discussed below), well-known emissivity values ($\varepsilon(\lambda)$) at the pyrometer wavelength (λ) can be taken from literature [189]. Known features in the data (such as the melting/resolidification temperature) can also be used to calculate the emissivity.

Alternatively, a multi-channel pyrometer can be used to acquire a wavelength-dependent

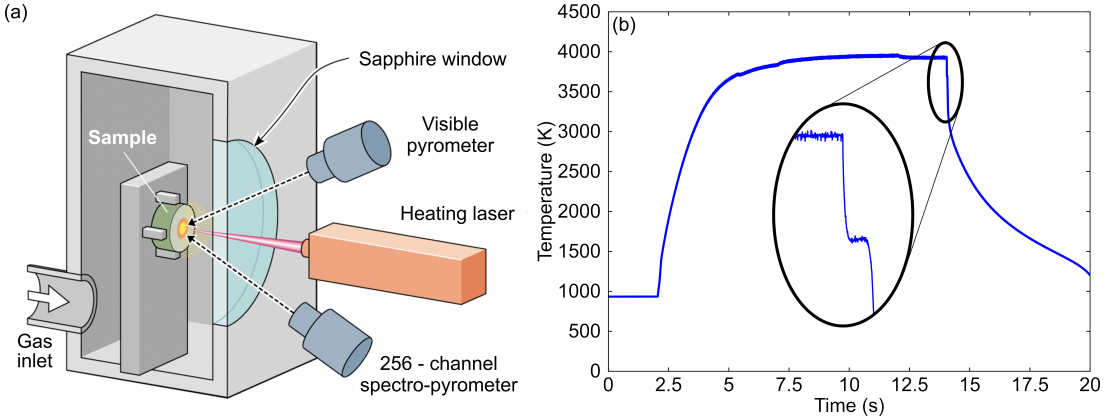

FIGURE 8.1: (a) A schematic of the apparatus used for pyrometry for measurement at high temperature and (b) the temporal thermal signal acquired. The resolidification plateau (b, inset) is analyzed to extract the enthalpy of fusion.

radiance temperature $T_r(\lambda)$ over the same field of view. For the data on bulk molybdenum, the pyrometer collected the radiance from the sample over a wavelength range of 500-1000 nm. Note that while many materials exhibit a highly-varying wavelength dependence for emissivity (and $\varepsilon(\lambda)$ is not necessarily a smooth function), it has been observed that molybdenum exhibits a linear emissivity relationship $\varepsilon(\lambda) = A \cdot \lambda + B$ in certain wavelength regimes [190, 191]. This means the $T_r(\lambda)$ data can be used in conjunction with Wein's approximation to determine the emissivity at the fast pyrometer wavelength [190, 192]. This is expressed as:

$$\frac{1}{T_{true}} = \frac{1}{T_{rad}(\lambda)} + \frac{\lambda}{C_2} \cdot ln\left[\varepsilon(\lambda, T) \cdot \alpha(\lambda)\right] \tag{8.1}$$

where C_2 is Planck's second constant (0.014388 m K), λ is the wavelength, $\varepsilon(\lambda, T)$ is the emissivity, and $\alpha(\lambda)$ is the transmittance of the window into the environmentally-controlled chamber. With the assumption that emissivity is linear, we thus seek a solution to the expression:

$$\frac{1}{T_{rad}(\lambda)} = \frac{1}{T_{true}} - \frac{\lambda}{C_2} \cdot ln\left[(A \cdot \lambda + B) \cdot \alpha(\lambda)\right] \tag{8.2}$$

where $T_{rad}(\lambda)$ is the raw variable-wavelength emissivity data (different values at each wavelength) and we seek values A and B which yield a constant T_{true} across all wavelengths. An example of this is shown in Figure 8.2 for the highest temperature molybdenum measurement.

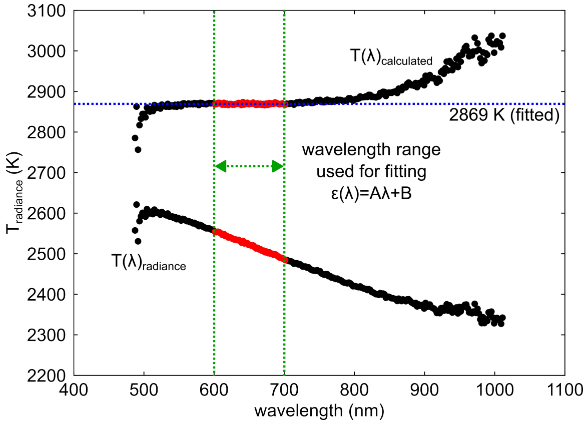

FIGURE 8.2: The pyrometer collected a radiance temperature, which varies with wavelength ($T_{radiance}(\lambda)$) as the emissivity varies ($\varepsilon(\lambda)$). The linear approximation for emissivity $\varepsilon(\lambda)$ may only be applicable across a narrow range of wavelengths [191], so the 600-700 nm range was used.

Note that in this work, I primarily refer to emissivity (the intrinsic emissive properties of the material), however it is important to differentiate this from emittance (the total emitted radiation including extrinsic effects). Emissivity is often a function of temperature, and emittance is changed as a function of surface roughness (where microscale texturing can result in multiple scattering events or increase the effective surface area, increasing the overall absorption or thermal emission of a surface). These may be difficult to separate in a pyrometry experiment, and both concepts are often combined, for example with literature measurements highlighting changes the apparent emissivity due to surface roughness [191, 193].

Since apparent emissivity is a function of temperature and surface roughness, it is important to perform the emissivity estimation on the sample around the temperatures at which measurements will be performed. Care must also be taken to avoid changes in specularity during the experiment (e.g., the sample should be polished, or the multi-channel data should be collected after melting has occurred).

8.2.2 Thermoreflectance

The second experiment was built upon an existing SSTR apparatus, which consists of a digitally modulated 100 mW laser (637 nm wavelength), serving as the pump and a second

70 mW laser (785 nm wavelength) serving as the probe. Both beams are focused onto the sample through a microscope objective lens (20x Mitutoyo), yielding spot sizes of approximately $\sim$ 3 μm diameter. The reflected probe beam is directed to a photodetector which is connected to a lock-in amplifier, allowing the pump-induced changes in reflectance to be recorded. Both pump and probe paths are fiberized until they reach the microscope objective, meaning minimal alignment is required and beam profiles and spot sizes remain consistent day to day.

For melting, I added a 5 W laser (532 nm wavelength, Spectra Physics Milennia eV), which was mechanically chopped at frequencies ranging from 100 Hz to 10 kHz. Since the melting or resolidification plateau is the key feature of interest in the data, long rise/fall times associated with the modulation may interfere with the measurement. As the rise/fall time is dependent on the size of the beam passing through the chopper (similar in principle to a knife-edge measurement [194] of the beam size), I thus focused the laser through the chopper using spherical lenses, achieving rise/fall times of $\lesssim$ 5% the cycle time. This 5 W laser was not fiberized, but was collimated with the fiberized pump and probe lasers immediately prior to entering the microscope objective, with a focused diameter of $\sim$ 9 μm at the sample surface. These aspects of the apparatus are shown in Figure 8.3. A lens pair was also used upstream to adjust the beam size entering the microscope objective, which allowed for a limited degree of independent control of the melting beam's focused spot size.

I used a Zurich Instruments UHF Lock-in amplifier to monitor the probe response, locking in to the same frequency at which either the pump or 5 W melting beam was modulated. For SSTR, the AC component of the probe response is monitored, as any changes in reflectivity of the sample occurring at this frequency can be considered to be solely due to modulated heating. For enthalpy of fusion measurements, the waveform of the probe response was monitored using the periodic waveform analyzer (PWA) function, allowing capture of the periodic temperature rise / melting curve.

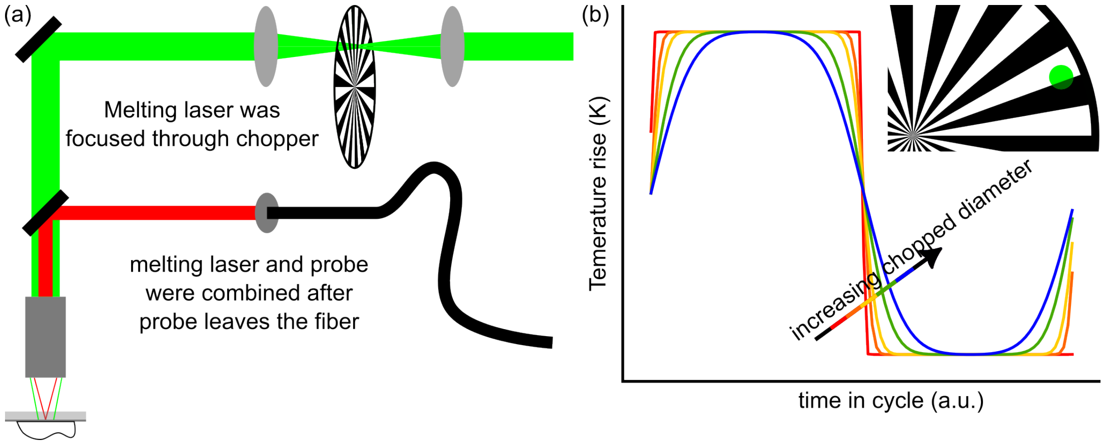

FIGURE 8.3: (a) a 5W free-space CW laser was added to an existing fiberized SSTR system. The sample consisted of a glass slide with an aluminum transducer deposited. The PCM was melted onto the surface of the aluminum, and the lasers were focused through the glass onto the aluminum. This allowed use of a transducer with partially-liquid samples. (b) The 5 W laser was focused through the chopper, with smaller focused beam diameters yielding more-abrupt laser intensity rise/fall times. This is visualized in the inset, where the beam may be partially-blocked by the chopper blade at a given instant in time, meaning the laser intensity reaching the sample does not go to zero instantly.

8.2.3 Numerical modeling and validation

No analytical model appears to exist for the time-dependent 3D (or axisymmetric) melting case [34], so numerical modeling was required. I developed a 2.5D thermal model (3D, cylindrical coordinates, axisymmetric in θ) written in Python, which captures phase change (h_f), radiative heat transfer (from the total hemispherical emissivity, ε_t), and conductive heat transfer. The model also includes the option for temperature-dependent properties: $K(T)$, $C(T)$, $\varepsilon(T)$. By considering the sample in cylindrical coordinates ($T(r,z,\theta)$) and considering the system to be axisymmetric (about z, i.e., no variance across θ), the system can be reduced to 2D ($T(r,z)$, shown in Fig. 8.4).

My implementation is a forwards-difference finite element scheme, where the temperature difference between elements is used to compute the conductive heat flux at a given timestep via Fourier's Law:

$$\Delta T(r_i,z_j)_{floor} = \frac{T(r_i,z_{j+1}) - T(r_i,z_j)}{\frac{1}{2}(\Delta z(r_i,z_j) + \Delta z(r_i,z_{j+1}))} \tag{8.3}$$

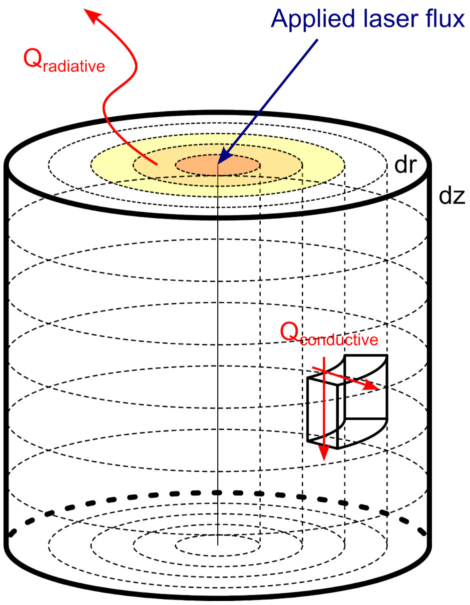

FIGURE 8.4: My finite element modeling captures conductive and radiative transport, temperature-dependent thermal properties, and melting. Conductive heat flux is calculated between elements based on each elements' temperature, thermal conductivity, and geometry, while radiative heat flux is calculate based on element temperature, radiative emissivity, and surface area. Q is calculated and temperatures are updated, for a series of timesteps.

This expression is analogous to $\frac{dT}{dz}$ in the heat equation based on the temperature difference between elements (denoted by indices i and j) and the average heights (Δz) of the elements. The heat flux is then calculated from $\Delta T(r_i, z_j)$ as:

$$Q(r_i,z_j)_{floor} = -\frac{1}{R_z(r_i,z_j)}\Delta T(r_i,z_j)_{floor} * A(r_i,z_j)_{floor} \tag{8.4}$$

analogous to Fourier's law $Q = -K \cdot A \cdot \nabla T$ expressed in terms of thermal resistivity R instead of conductivity K. The through-plane thermal resistivity between the two elements $R(r_i, z_j)$ is calculated as:

$$R_z(r_i,z_j) = \frac{1}{2}\left(\frac{\Delta z(z_j)}{K_z(r_i,z_j)} + \frac{\Delta z(z_{j+1})}{K_z(r_i,z_{j+1})}\right) \tag{8.5}$$

calculated from the elements' heights and through-plane thermal conductivities ($K_z(r_i, z_j)$). I use $1/R_z$ in lieu of the thermal conductivity and average element heights to ensure accurate tabulation of energy throughout the system (e.g., avoiding energy loss as energy moves between elements of high vs. low thermal conductivity). interfacial resistance can also be captured by adding the TBR to the elements' thermal resistance, without the need for an additional interfacial element. A similar treatment is applied to the walls between each element in the radial direction:

$$\Delta T(r_i, z_j)_{wall} = \frac{T(r_{i+1}, z_j) - T(r_i, z_j)}{\frac{1}{2}(\Delta r(r_i, z_j) + \Delta r(r_{i+1}, z_j))} \tag{8.6}$$

$$Q(r_i, z_j)_{wall} = -\frac{1}{R_r(r_i, z_j)} \Delta T(r_i, z_j)_{wall} * A(r_i, z_j)_{wall} \tag{8.7}$$

$$R_r(r_i, z_j) = \frac{1}{2}\left(\frac{\Delta r(r_i)}{K_z(r_i, z_j)} + \frac{\Delta r(r_{i+1})}{K_z(r_{i+1}, z_j)}\right) \tag{8.8}$$

The surface area of elements is calculated as follows:

$$A(r_i, z_j)_{floor} = \pi \cdot (r_{i+1}^2 - r_i^2) \tag{8.9}$$

$$A(r_i, z_j)_{wall} = 2 \cdot \pi \cdot r_{i+1} \cdot h(z_j) \tag{8.10}$$

where r_i and z_j refer to the inner and upper coordinates of the given element.

Radiated energy flux is calculated following Stefan-Boltzmann law:

$$Q(r_i, z_j) = \sigma \cdot \varepsilon_t \cdot A \cdot (T(r_i, z_j)^4 - T_{surroundings}^4) \tag{8.11}$$

where σ is the Stefan-Boltzmann constant (5.67×10^8 W m^{-2} K^{-4}) and A is the element upper/lower/wall area. It is useful to scale temperature prior to this calculation (e.g., using units of centi-Kelvin, and a Stefan-Boltzmann constant or 5.67 W m^{-2} cK^{-4}) to avoid over-flow errors due to the T^4 terms.

Once heat flux is calculated ($Q = Q_{conductive} + Q_{radiative}$, summing heat flow through all walls and horizontal surfaces, at r_i,r_{i+1},z_j,z_{j+1}), the temperature change of each element for the timestep is calculated:

$$T(r_i, z_j)^{n+1} = T^n(r_i, z_j) + \frac{Q(r_i, z_j) \cdot \Delta t}{C(r_i, z_j) \cdot V(r_i, z_j)} \tag{8.12}$$

which is analogous to the $\frac{dT}{dt}$ term in the analytical heat equation.

Latent heat of fusion is captured separately by tracking a melt state (between 0 and 1, for fully solid vs. fully molten). For the idealized case where melting occurs precisely at a given temperature, a temperature adjustment can be made any time the temperature exceeds the melting point assuming the melt state is not 1. The maximum allowable temperature adjustment is $\Delta T_{max} = h_f(r_i, z_j)/C(r_i, z_j)$, but should not exceed the overage temperature (i.e., the temperature adjustment should return the temperature to the melting point, but not below). The melt state is then updated based on $\Delta T \cdot C \cdot h_f^{-1}$. For the more realistic case where a phase transition occurs over a range of temperatures, a Gaussian error function determines the maximum melt state for a given temperature. This allows for the initiation of melting at temperature below the nominal melting point, and limits the temperature reduction at points above the nominal melting temperature. This can be understood visually via Figure 8.5.

By capturing enthalpy of melting in this way, I avoid needing to track enthalpy directly (instead tracking melt progress during melting only), which automatically accounts for temperature-dependent heat capacity. It also provides an intuitive equivalence relationship between heat capacity and latent heat of fusion: $T_{effective} = h_f/C$. This represents the equivalent temperature rise a material might experience if the phase transition had not occurred (noting the relationship between enthalpy in units energy per volume (e.g., J m^{-3}) and heat capacity in units energy per temperature per unit volume (e.g., J m^{-3} K^{-1})). This also negates the need for repeated scaling by the element volumes. I have formalized the expressions for this below.

$$\Delta T(r_i, z_j)_{max} = \frac{h(r_i, z_j)}{C(r_i, z_j)} \tag{8.13}$$

$$\Delta T(r_i, z_j)_{over} = min[\Delta T(r_i, z_j)_{max} \cdot (1 - m(r_i, z_j)), T(r_i, z_j)^{n+1} - T(r_i, z_j)_{melt}] \tag{8.14}$$

which captures the possibility of a previously partially-molten state ($m(r_i, z_j)$) and avoids reducing the temperature to below the melting point. The melt state is also updated accord-

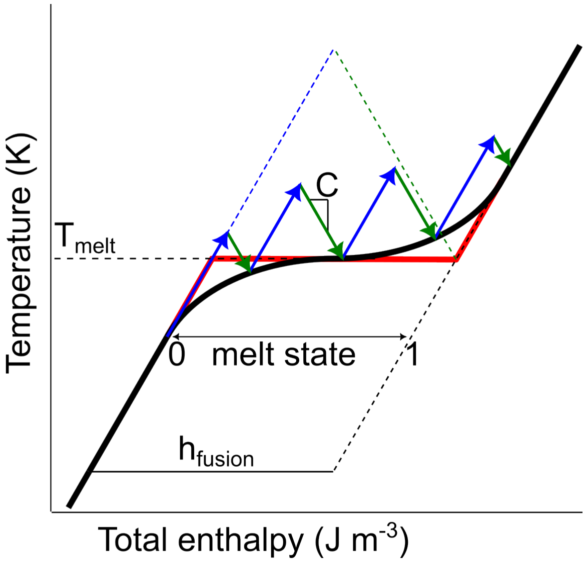

FIGURE 8.5: The energy flow code may add temperature and enthalpy to a given element (blue arrows), however if the temperature exceeds the melting point, an adjustment to the temperature and melt state must be made. In the idealized case of perfectly-abrupt melting (red plateau), the temperature adjustment is simply the overage temperature until a fully molten state is reached. For the case of non-abrupt melting, a Gaussian error function guides the maximum melt state as a function of temperature (black). In either case, the temperature is brought back down and the melt state is updated (green arrows) based on the instantaneous heat capacity. This can be understood as an effective temperature $T_{effective} = h_f/C$ which describes the energy contributing to the phase change as opposed to a temperature rise. It can be seen that the length of the green arrows (for the non-abrupt melting case) matches the length of the dashed green line (showing the total enthalpy absorbed by melting). In other words, the temperature range over which melting occurs should not change the total measured enthalpy of fusion (i.e., the horizontal offset between solid/liquid portions of the curve).

ingly:

$$m(r_i,z_j)^{n+1} = m(r_i,z_j) + \frac{\Delta T(r_i,z_j)_{over}}{T(r_i,z_j)_{effective}} \tag{8.15}$$

For resolidification, all steps are similarly performed, with an increase in temperature applied when an element dips below the melting point.

To determine the probe response (or pyrometer temperature response) of the system, the surface temperature is weighted by the probe intensity as a function of position, and the result is integrated (or weighted uniformly over the viewed area for the pyrometer). This is identical to the procedure used in the analytical calculation for thermoreflectance experiments [15–18].

I validated the above model in a number of ways. To begin, I considered the non-radiative and non-melting case, and compared the temporal response under square-wave heating against the analytical model (capable of finding the exact solution) for an a-SiO_2 sample (1.4 W m^{-1} K^{-1}, 1.63 MJ m^{-3} K^{-1}) under periodic heating (1 kHz, 10 µm diameter pump and probe spot sizes). This is shown in Figure 8.6.a below, and I found satisfactory agreement assuming sufficient discretization was used (small enough Δr, Δz, and Δt). While a maximum timestep size (Δt) is required for stability, a smaller timestep will also affect the accuracy of the results (I use $\Delta t \simeq \frac{1}{12} \cdot C \cdot \Delta x^2 \cdot K^{-1}$, which is based on a slight reduction from the maximum stable timestep size based on Von Neumann stability analysis). Also of note: instability may still occur at this level if radiative transfer is large at high temperatures, as the Von Neumann stability analysis is performed for conductive transport only. The required Δr and Δz depend on the spatial features of the experiment. Large spot sizes may not require a small Δr, as the expected radial temperature gradient will be small (I used Δr = 0.5 µm, i.e. 10 elements inside the 1/e^2 beam radii). In contrast, the use of a transducer may require small Δz due to the abruptly changing properties simulated (I used Δz = 50 nm for the first 200 nm of the sample). While the analytical solution captures semi-infinite boundary conditions by default, I also found the size of the numerically simulated volume affected the results, as thermal accumulation within the volume can lead to a continuous temperature rise over multiple cycles.

Slight deviations in the magnitude of the signal appear, however the normalized signal (101.5% scaling) lines up almost exactly. For a PWA signal (e.g., using the thermoreflectance apparatus), normalization is performed during the analysis, so this should not be a concern.

To validate radiative and melting effects, I also modeled the tungsten sample using Ansys Fluent, comparing the results against the finite element code. I began by comparing the steady-state temperature distribution across the surface under identical simplified input conditions (2 mm thick by 10 mm diameter disk, 0.02 mm mesh size, K=90 W m^{-1} K^{-1}, ρ=19254 kg m^{-3}, C=260 J kg^{-1} K^{-1}, h_f=285 kJ kg^{-1}). Within Ansys Fluent, a heat flux boundary condition is incompatible with an emissive radiation boundary condition on the same surface, so I applied a 50 MW m^{-2} flux across the 3.5 mm beam spot diameter, with ε_t=0.38 applied elsewhere. The steady-state comparison is shown in Figure 8.6.b below. A slight deviation existed, which also yielded a difference in melt pool size (Fig. 8.6.c,d). A larger melt pool will take proportionally longer to resolidify, so to prepare for transient analysis, I adjusted the applied surface flux (laser power) until the melt pools were of approximately equal size at steady state. I then ran transient simulations, initialized using the steady state temperature and melt distributions. Upon removal of the constant energy flux boundary condition in Ansys Fluent, I could re-enable the ε_t=0.38 radiative boundary condition for the beam area, and I made a similar change in the numerical Python code. I set the melting temperature to 3695 K in both models (a range can also be set in Ansys Fluent via the $T_{solidus}$ and $T_{liquidus}$ parameters). Reasonable agreement was found for the transient resolidification behavior (Fig. 8.6.e).

Care must be taken to ensure the discrepancies observed do not affect the fitting for thermal properties and latent heat. Just as a slight error in K or ε_t will both affect the steady state temperature (and thus the melt pool size and resolidification plateau duration), numerical error could do the same. For this reason, the laser absorption coefficient was fitted using the steady state temperature before fitting any resolidification data. I chose fitting of the absorption coefficient as this is likely the least well known of all parameters,

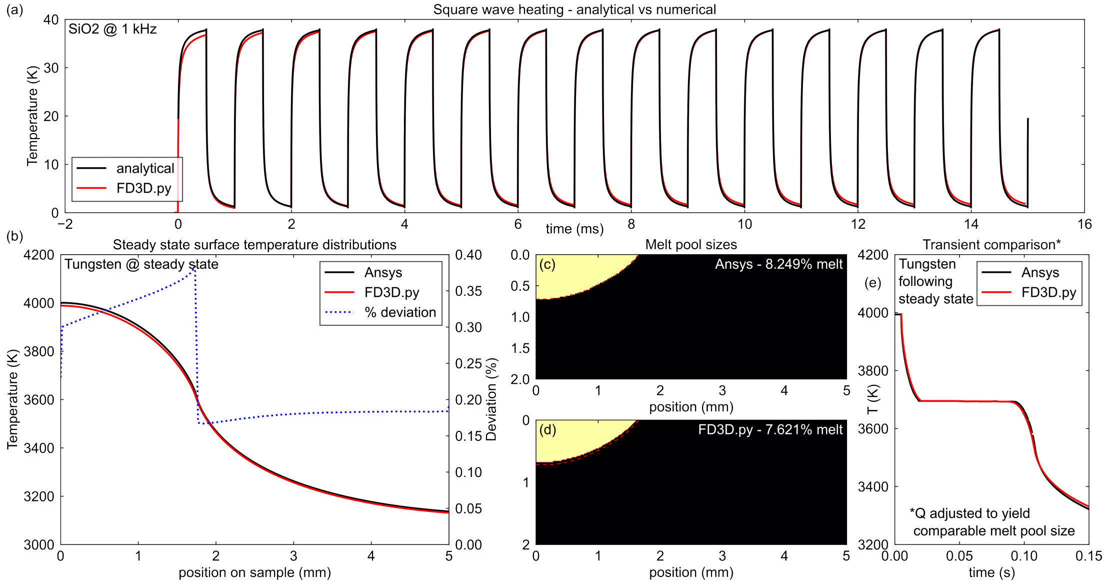

FIGURE 8.6: (a) The analytical and numerical models are compared for square wave heating. It takes several cycles for the numerical code (initialized at a uniform T=0) to arrive at a steady condition whereas the analytical code is solved in the frequency domain (and naturally captures steady state heating). A slight deviation means fitting for the magnitude of this temperature rise may yield slight errors, however the PWA signal is is normalized, negating this effect. (b) The steady state surface temperature distributions are compared between Ansys Fluent and my numerical code. A slight deviation also yields a slight difference in melt pool size (c,d). Once this issue is corrected (by adjusting the constant energy flux boundary condition), the transient resolidification trends (e) line up.

and fitting to the steady state temperature should negate errors due to changes in the melt pool size.

One initial finding from the modeling was the ability to replicate general trends within the published data, namely the absence of the melting plateau despite the presence of the resolidification plateau. Since the laser heating is localized at the surface of the sample, the surface temperature rise is dependent in part on the applied laser flux. Melt pool growth is also only possibly via conductive heating of the material neighboring the melt pool. A thermal gradient is necessarily required for conductive transport, meaning the center of the melt pool (where heat is applied) is necessarily higher in temperature than the edges of the pool. A continually-increasing pool temperature thus obscures the effects of melt pool growth in the signal.

This is in contrast to melt pool shrinking and resolidification, where heat is removed through conduction from the outer perimeter of the melt pool (and to a lesser degree, surface radiation). This means the molten surface does not cool substantially until the entire melt pool has shrunk and resolidified, resulting in a clear thermal arrest. This can be seen in Figure 8.7, showing the temperature distribution in a simulated tungsten sample during melt pool growth and resolidification.

8.3 Data Analysis

The duration of the melt plateau should be roughly proportional to the enthalpy of fusion h_f, however numerous other thermal and experimental parameters also play a role. Both enthalpy of fusion and heat capacity are often thought of as energy storage parameters, and the modeling of energy absorption from h_f via temperature adjustments of $\Delta T = h/C$ suggests uncertainty in C may proportionally affect the fitted h_f. Thermal conductivity K of the sample and radiative emissivity ε_t both play a role as well, as these affect how quickly energy is drawn out of the melt pool. More subtly, both of these (and the ratio of heat carried away via radiation) will also affect the physical size of the melt pool at steady state, leading to a proportional change in the duration of the resolidification plateau. The pump laser beam's spot size is also critical, as this affects the size of the melt pool. Less obviously, the size of the reflected probe laser beam, or the size of the area viewed by the pyrometer, may also play a role, as the temperature reading comes from the weighted integrated temperature across this area. Extraction or validation of each of these parameters will be discussed in depth below for each experiment.

Inferring unknown parameters - Pyrometry for high-temperature measurements on bulk samples

Given the importance of the various thermal parameters for modeling, their accuracy is critical for an accurate quantification of the enthalpy of fusion (h_f). Fortunately, multiple of these parameters can be fitted using specific regimes within the dataset (or if the parameters

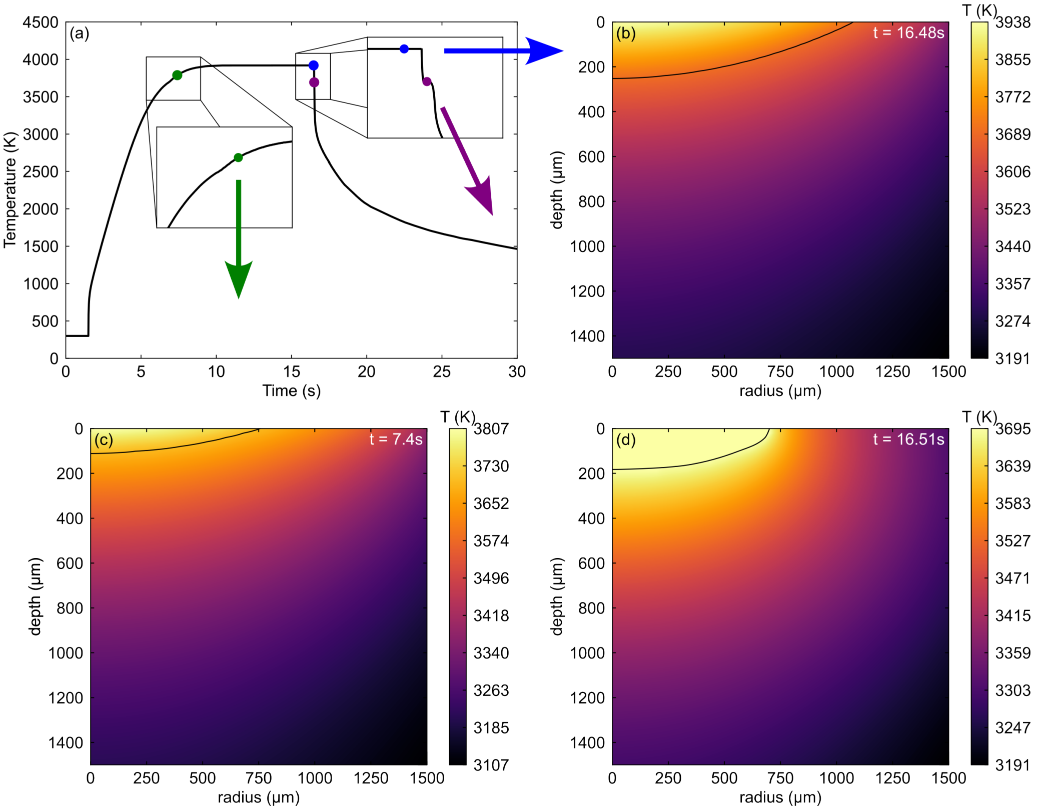

FIGURE 8.7: (a) The probed temperature as a function of time was modeled, with 3 points in time (insets) selected and the corresponding temperature distributions shown (b-d). The black line in b-d denotes the melt front. During melting (inset left, c), only a slight flattening of the thermal rise is visible. Since laser flux is applied to the surface, the surface continues to increase in temperature as the melt pool grows. This serves to obfuscate the melting signature in the data. At steady state (inset right, b), the melt pool is stable in size, and the temperature gradient depends on thermal transport properties only (thermal conductivity and emissivity). During solidification (inset right, c), a thermal arrest is clearly visible in the transient data. Since the melt pool is at a uniform temperature and primarily cools via conduction around the perimeter, the duration of the thermal arrest depends on the enthalpy of fusion, thermal conductivity, and the melt pool size.

are already known, these regimes can serve as a sanity check should other errors be present). These will be discussed below, and are outlined in the Fig. 8.8.a as well.

I began by fitting the steady-state temperature rise for a single unknown thermal or experimental parameter, as this is unaffected by h_f. Next, additional unknown thermal parameters could be extracted from the curvature and slope of thermal decay immediately following the resolidification plateau (similarly unaffected by h_f, assuming a lateral shift can be applied between data and model). The steady state temperature is insensitive to heat capacity [17, 195], and sensitive to laser absorption, radiative emissivity, thermal conductivity, and in some cases, the sample geometry. By comparison, the post-solidification thermal decay is insensitive to pump laser absorption, while being sensitive to thermal conductivity, radiative emissivity, and heat capacity. Note that the curvature and slope of this post-resolidification thermal decay are differently sensitive to the each parameter, meaning it may be possible to fit multiple using data in this regime.

Based on Kirchhoff's law, one might expect the absorption coefficient to be equal to the radiative emissivity, however this is not always the case. Emissivity often has a slight wavelength and/or angle dependence [196], and the radiative emissivity used for modeling the heat flow away from the sample is the total hemispherical emissivity (ε_t), which is the spectrally- and angle-dependent emissivity ($\varepsilon(T,\phi,\lambda)$) integrated over all angles (ϕ) and wavelengths (λ). Surface roughness also affects the apparent emissivity [191, 193], and particularly in the case of a sample with a melt pool, the surface texture of the melt may differ substantially from that of the unmelted (or resolidified) sample around it. Additionally, the solid vs. liquid emissivity may not be the same [197–200]. All of these factors may contribute to slightly differing values for pump laser absorption, pyrometer wavelength-specific emissivity values, and the total hemispherical emissivity ε_t contributing to radiative cooling across the sample. Nonetheless, the laser absorption and pyrometer emissivity values (found from the true-temperature correction step during data post-processing) may be close (depending on the accuracy of the gray-body assumption and the proximity between laser and pyrometer wavelengths), and setting laser absorption from pyrometer emissivity may be a suitable approximation. Total hemispherical emissivity values may also be drawn from literature, assuming the sample surface quality is assessed (e.g., polish level or surface roughness). Additionally, I recommend the use of multi-channel pyrometry [192] (rather than single-color as alluded to previously), as this and related measurements can enable better characterization of the total hemispherical emissivity (ε_t) required for modeling. In other words, if a many-channel pyrometer is used for calculating the true temperature data, the same many-channel spectral readings of radiance temperature ($T_{rad}(\lambda)$) can serve as a check on the grey-body assumption or provide clues as to how the total hemispherical emissivity may differ.

Literature data on sample thermal conductivity may not be available at high temperature, however the works of Milich *et al.* [189] showed these can be extracted from experiments using the same apparatus with a different heating regimen. In the technique referred to as Steady State Temperature Differential Radiometry (SSTDR), the laser power is perturbed, and the change in steady-state temperature is used to determine the thermal conductivity at varying temperatures. While the authors intentionally chose this measurement scheme to avoid sensitivity to heat capacity (taking inspiration from the low-temperature SSTR technique [17]), it may be possible to fit the rise-time for this perturbative heating as well (analogous to a related technique, Square Pulse Thermoreflectance [18]). Both of these strategies would yield *in situ* direct measurements of thermal conductivity and heat capacity respectively without needing a separate apparatus. The use of a secondary laser with a tightly-focused laser spot to initiate this secondary heating [2] would also mean the perturbative measurement would benefit from preserved semi-infinite boundary conditions (as used by SSTR [17] and SPTR [18]) to simplify the analysis.

Knowing the sample diameter and thickness are also key, as this will affect the relative contributions between energy dissipated via conductivity vs. radiation (including surface radiation, and radiation from the back side of the sample). For nanoscale thermoreflectance experiments, the semi-infinite approximation is almost always made (adiabatic sample back side), however for these high-temperature experiments, even a ~ 2 mm thick sample saw a

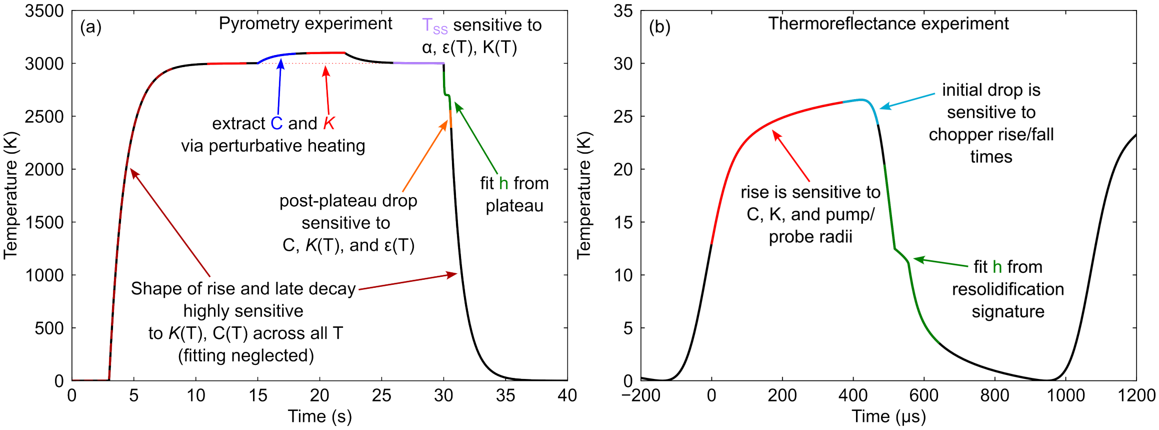

FIGURE 8.8: (a) Separate regimes within the pyrometry dataset can be used for fitting or confirmation of several thermal parameters. I neglect fitting of the initial rise, but recommend a perturbative heating scheme (as seen in Milich *et al.* [189]) to measure K and C once steady state is reached (red/blue). The steady-state temperature (lavender) is sensitive to pump absorption (α), $\varepsilon(T)$, and $K(T)$. The post-resolidification curvature (orange) is sensitive to C, $K(T)$, and $\varepsilon(T)$. Once all unknowns are quantified, the plateau can be fit for the enthalpy of fusion h_f. (b) A similar approach can be used for the cyclic-heating thermoreflectance data. The rise is primarily sensitive to K, C, and the pump and probe spot sizes, and the initial decay is sensitive to the rise/fall times associated with the chopper. Error in any of these parameters can affect fitting of the enthalpy of fusion h_f.

significant contribution due to back-side radiation.

Finally, a physical measurement of the melt pool diameter *in situ* may also be used to guide and validate any fitting performed. The melt pool size directly impacts the duration of resolidification, and is linked to many of the parameters mentioned (e.g., a high thermal conductivity will increase thermal spreading within the sample).

It is also critical to note that many of these properties are temperature dependent (thermal conductivity, heat capacity, radiative emissivity), however some approximations can be made. Temperature-dependent heat capacity is the least important of these, as I will analyze a relatively narrow range of temperatures around the resolidification plateau, and the temperature range of this region is unlikely to see a dramatic variation in C. In contrast, the emissivity and thermal conductivity of regions of the sample far from the melt pool will still affect thermal transport away from the melt pool (as evident by the importance of the back-side radiation in our high-temperature samples), meaning the temperature-dependent conductivity and emissivity may be critical. While full $K(T)$ and $\varepsilon_t(T)$ curves may not be readily available or easily acquired, approximations may suffice (e.g., thermal conductivity and emissivity may be treated as linear depending on the steady-state temperature distribution within the sample and temperature-dependent trends of each property). An example of this for emissivity specifically is shown in Fig. 8.9 in the following section. The degree to which each parameter affects the fitted result will also be shown in Figure 8.11 of the following section.

Once all thermal and physical parameters are adequately characterized, the width of the plateau can be analyzed. This is done by selecting points at two temperatures immediately above and below the plateau and adjusting h_f until the time between these points matches between data and model. By fitting the plateau width in this manner, I avoid error due to subtle differences in the round-off of the plateau. This round-off can occur due to the radial-averaging of the pyrometer reading, as the pyrometer is simultaneously sampling portions of the melt pool that may be above T_{melt}, and solidified portions that may be below T_{melt}. Rounding off (or a stair-step behavior) of the plateau edges is also strongly affected in the model by the spatial discretization used. I also observed a slight increase in apparent temperature as resolidification progresses in some datasets, which could be due to a slight change in pyrometer emissivity during the phase change [197–200] or an undercooling phenomena [183–185]. In many materials, softening and melting may occur over a range of temperatures, and this will lead to a rounding off of the plateau as well. While the model is capable of capturing this effect, I did not fit for it.

Inferring unknown parameters - Thermoreflectance for low temperature measurements on thin films and semi-infinite samples

Given that the thermoreflectance experiments will typically be performed at less extreme temperatures (due to limitations in transducer performance at high temperatures [201]), the measurement of the required unknown thermal parameters is less challenging. A measurement of the thermal conductivity and heat capacity up to and around the melting point should be performed with any existing technique, e.g., via SSTR [17], FDTR [16], or SPTR [18]. Each of these techniques can be performed on the apparatus discussed, using external heating to hold the sample at a constant temperature while measurements are performed. This external heating can be applied via a separate laser [2, 201] or a heating stage [201]. Each techniques also has differing sensitivity to thermal conductivity and heat capacity, meaning one or more may be used in conjunction to minimize experimental uncertainty.

SSTR and FDTR are both insensitive to the rise/fall times associated with the modulated beam waveform, as the lock-in amplifier selects the component of the signal at the modulated frequency (i.e., higher order terms in the Fourier series can be neglected). This is a key parameter for accurate modeling of the waveform in SPTR however. For a mechanically chopped beam with a Gaussian intensity profile, the rise/fall will be a Gaussian error function (the integral over the Gaussian beam intensity profile) with a width directly dependent on the Gaussian beam's diameter. Modeling the Gaussian waveform was not discussed in the original works developing SPTR however [18]. In the interest of having an analytical model to represent the waveform (excluding melting and radiative transport), I thus developed a slight modification to the model used for SPTR.

For the existing thermoreflectance techniques, an analytical solution to the heat equation (for an arbitrary planar stack of materials, axisymmetric conditions) can describe the sinusoidal temperature rise ($\Delta T(\omega)$) under a sinusoidal applied laser flux. The solution for the probe response is a complex value, with the real component denoting the temperature oscillations (at frequency ω) in phase with the cyclic heating, while the imaginary component denotes the temperature oscillations out of phase with the cyclic heating. The ratio of in-phase vs. out-of-phase (real vs. imaginary) components can be used to find a phase angle or temporal lag between the cyclically applied heat flux and cyclic temperature rise.

To transform this frequency-domain solution to the time domain (or to consider a more complex heating waveform, i.e., anything but perfectly sinusoidal), a Fourier series can be used to represent the true time-dependent heating waveform. In the case of TDTR, Cahill [15] used the Fourier series representing a train of pulses (at a laser repetition rate ω_p) with modulated intensity (at a modulated frequency ω_m), as:

$$T(t_d) = \sum_{n=-\infty}^{\infty} \Delta T(\omega_m + n \cdot \omega_p) * e^{(i \cdot n \cdot \omega_p \cdot t_d)} \tag{8.16}$$

for a given time delay t_d. Note $T(t_d)$ is still complex, and the lock-in amplifier returns the real/imaginary components of $V(t_d)$, which is a photodetector voltage response dependent on $T(t_d)$ along with physical scaling parameters (the probe intensity, thermoreflectance coefficient, detector sensitivity, etc). Similarly, the temporal response for the idealized case of square-wave modulation [18] is derived from the Fourier series representing a square wave:

$$f(t) = \frac{4}{\pi} \sum_{n=1,3,5...}^{\infty} \frac{1}{n} sin(\frac{n \cdot \pi \cdot t}{L}) \tag{8.17}$$

where L is the cycle duration, or

$$T(t) = \sum_{n=0}^{\infty} \Delta T(\omega_m \cdot (2 \cdot n - 1))) * e^{(i \cdot \omega_m \cdot t \cdot (2 \cdot n - 1))} \tag{8.18}$$

at a point in time t, or simply:

$$T(t_d) = \sum_{n=0}^{\infty} \Delta T(\omega_m \cdot n) * e^{(i \cdot \omega_m \cdot t \cdot n)} \tag{8.19}$$

for odd integers n.

Given that the time-domain temperature response can be computed by way of a Fourier series of the pump waveform and calculating the temperature rise for each component frequency in the frequency domain, one can easily extend this to an arbitrary waveform. Given an arbitrary waveform (e.g., the square waveform with Gaussian error functions for the rise/fall rather than the perfectly-abrupt step), I simply generate the discrete pump waveform function ($P = f(t_n)$ for n time points) and take its discrete Fourier transform ($A_n = \mathscr{F}(f(t_n))$ for n frequencies ω_n). Each resulting complex value (A_n) is the pre-factor for the corresponding term in the Fourier series, and the thermal response is calculated at each frequency. The resulting temporal thermal response then comes from the sum over each component, i.e., the discrete inverse Fourier transform:

$$T(t) = \sum_n A_n \cdot \Delta T(\omega_n) \cdot e^{i \cdot \omega_n \cdot t} \tag{8.20}$$

or

$$T(t) = \sum_n Re\left[A_n \cdot \Delta T(\omega_n)\right] \cdot cos(\omega_n \cdot t) - Im\left[A_n \cdot \Delta T(\omega_n)\right] \cdot sin(\omega_n \cdot t) \tag{8.21}$$

The Gaussian rise-time can be measured by directing the pump beam to a photodetector and acquiring a PWA signal or by fitting on a sample of known thermal properties. Note that this rise/fall time is a set percentage of the cycle duration (and thus inversely proportional to the modulation frequency) since it is a product of the beam's diameter relative to the chopper blade opening and fin width.

This analytical thermal model is exceptionally fast computationally (especially compared to the finite element model) and I took advantage of this in a number of ways. First, specific regimes within the melting dataset could sometimes be used to dial in unknown modeling parameters or to confirm that the correct parameters were being used (Fig. 8.8.b). For example, melting only minimally affects the shape of the thermal rise (as opposed to the resolidification signature during the thermal decay). This regime is sensitive to thermal conductivity and heat capacity (the rise time being inversely proportional to thermal diffusivity $\alpha = K/C$), laser spot sizes (the rise time being dependent on the size of the heated volume), or transducer thickness (contributing to in-plane thermal spreading). Similarly, the initial moments of the thermal decay are primarily dependent on the rise/fall times associated with the beam passing through the chopper. Confirmation of the chopper rise/fall times is especially important, as this is directly dependent on the day-to-day apparatus alignment.

Sensitivity analysis using the analytical model can also serve as guidance for accelerating the numerical modeling. The curvature of thermal rise and decay, and the size of the melting plateau, are significantly affected by thermal spreading in the transducer (which affects the size of the heated volume). This means the measurement is highly sensitive to the transducer thickness and in-plane thermal conductivity, but negligible sensitivity to the transducer through-plane thermal conductivity. Due to limitations relating to von Neumann stability (where modeling of high K, low C, and small finite element mesh sizes Δr and Δz will require small timestep sizes Δt), numerical modeling of thin metal transducers (e.g., 180 W m^{-1} K^{-1}, 2.6 MJ m^{-3} K^{-1}, and 80 nm, which requires small Δz) for long a duration (hundreds of μs) can take prohibitively long. For a material system / measurement scheme insensitive to the cross-plane transducer thermal conductivity however, artificially-low values for the through-plane thermal conductivity can be used with negligible effect on the final modeled curves (within reason). Using high- aspect-ratio rectangular finite elements ($\Delta r >> \Delta z$) I could maintain the correct in-plane thermal conductivity by simply using larger in-plane discretization (Δr).

8.4 Experimental results

Pyrometry results - Tungsten

Tungsten is the highest-temperature experimental dataset analyzed, and also the sample with the highest influence of temperature-dependent properties. The sample consisted of a 10 mm diameter disk with a thickness of 2 mm, which was heated with a laser power of 1.9 kW in the center of the circular face (with 86% transmission through the enclosure window). Thermal conductivity as a function of temperature was taken from Touloukian *et al.* [202], with the more-recent measurements from Milich *et al.* [189] used as confirmation. Heat capacity was taken from Touloukian *et al.* [203] as well, using a density of 19.3 Mg m^{-3}. Noting the huge variation in the data for total hemispherical emittance from Touloukian *et al.* [191] but a general upwards trend with increasing temperature, I fit for the radiative emissivity using the post-plateau decay, finding a linearly-dependent emissivity between 0.1 and 0.6 between 300 K and 4000 K fit well (shown in Figure 8.9). I also explored the sensitivity of the experiment to the linear approximation for $\varepsilon_t(T)$ by perturbing the line and re-generating the melting trend. In general, perturbing the high-

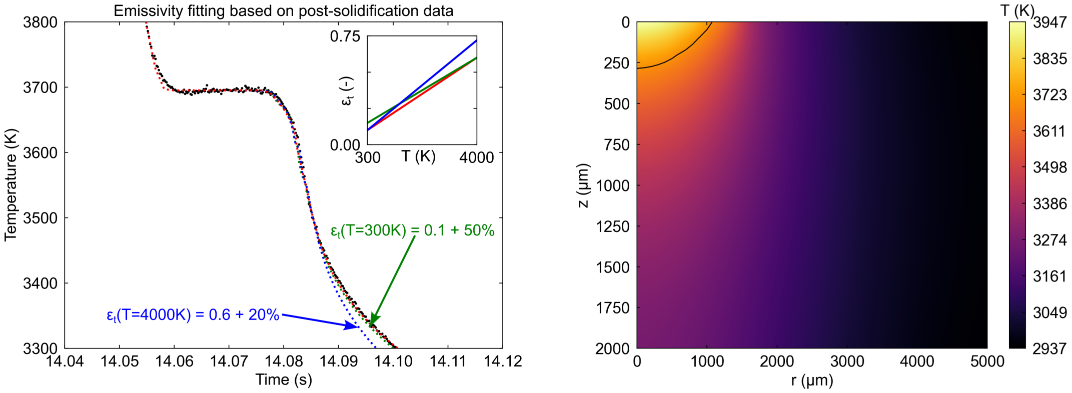

FIGURE 8.9: (left) The initial post-solidification data was used for fitting a temperature dependent total hemispherical emissivity $\varepsilon_t(T)$. I used a linear approximation (inset, red), and also present perturbations on this linear $\varepsilon_t(T)$ to explore the post-solidification data's sensitivity. (right) The modeled temperature distribution in the sample immediately prior to removal of laser flux was used to justify the linear $\varepsilon_t(T)$ approximation. No sample surface was below 2900 K, suggesting the curvature of the realistic $\varepsilon_t(T)$ should not affect the h_f fitting.

temperature emissivity had a larger effect on the data, and the post-solidification curvature could also be seen to change (Figure 8.9). As a point of reference, Milich *et al.* [189] used an assumed emissivity of 0.38 at the pyrometer wavelength (663 nm, based on literature) to convert between radiance- and true-temperature, and found an excellent match for melting temperature (3698 K). It should be noted that differences in surface texture and wavelength-dependence can affect these values however. Fitting for the enthalpy of fusion, I found a value of 4.89 GJ m^{-3} (254 J g^{-1} or 46.7 kJ mol^{-1}). This is in line with the values from electrical heating/resistivity measurements and theory [204, 205] ranging from 46.0 - 54.9 kJ mol^{-1}).

I also ran a form of sensitivity analysis for the tungsten dataset, investigating each experimental parameter's effect on the results. This can be seen in Figure 8.11. Each parameter was perturbed by 10%, the laser absorption was adjusted to achieve the correct steady state temperature, and the temporal resolidification curve was regenerated. The original (dotted red) and deviated solidification curves (solid) can then be then compared. In some cases (e.g., pump beam radius or sample thickness), a small change to the assumed value drastically affects the resulting size of the solidification plateau, suggesting that an accurate

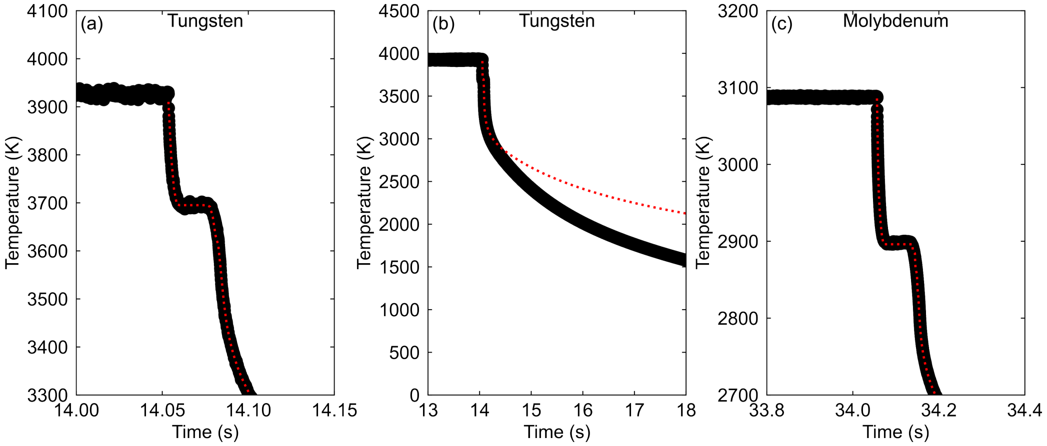

FIGURE 8.10: (a) Fitted data for the resolidification plateau for tungsten used to determine the enthalpy of fusion. (b) Fitting was not performed over the entire cooling portion of the tungsten dataset, as this would require knowledge of all temperature-dependent properties, $C(T)$, $K(T)$, $\varepsilon_t(T)$. (c) Fitted data for the resolidification plateau for molybdenum used to determine the enthalpy of fusion. The duration of the molybdenum plateau was larger despite a smaller h_f, since tungsten has a slightly higher $K(T)$ and experiences more radiative cooling at higher temperature. Faster heat flow away from the melt pool thus yields a faster resolidification.

quantification of these values is critical for an accurate assessment of h_f. In other words, an error in the assumed parameter would require a large (and erroneous) adjustment to h_f in order to find a modeled plateau duration matching the data. In other cases the perturbed parameter has little or no effect on the plateau size (e.g., heat capacity or pyrometer viewing area). This suggests that approximations or assumptions for these values may be acceptable, as error or uncertainty in these parameters should have little effect on the fitted h_f. Changes to the post-solidification thermal decay (curvature and slope) are also visible, indicating that these regions of the dataset can be used for fitting (or validation) of one or more parameters. A full discussion of each parameter's influence on the data is discussed briefly in Table 8.1.

Pyrometry results - Molybdenum

I also considered pyrometry data for a molybdenum sample, with an identical geometry and experimental configuration used for the tungsten measurements. Laser power was set to 1.2 kW (again with a 86% transmission through the window). Thermal conductivity and

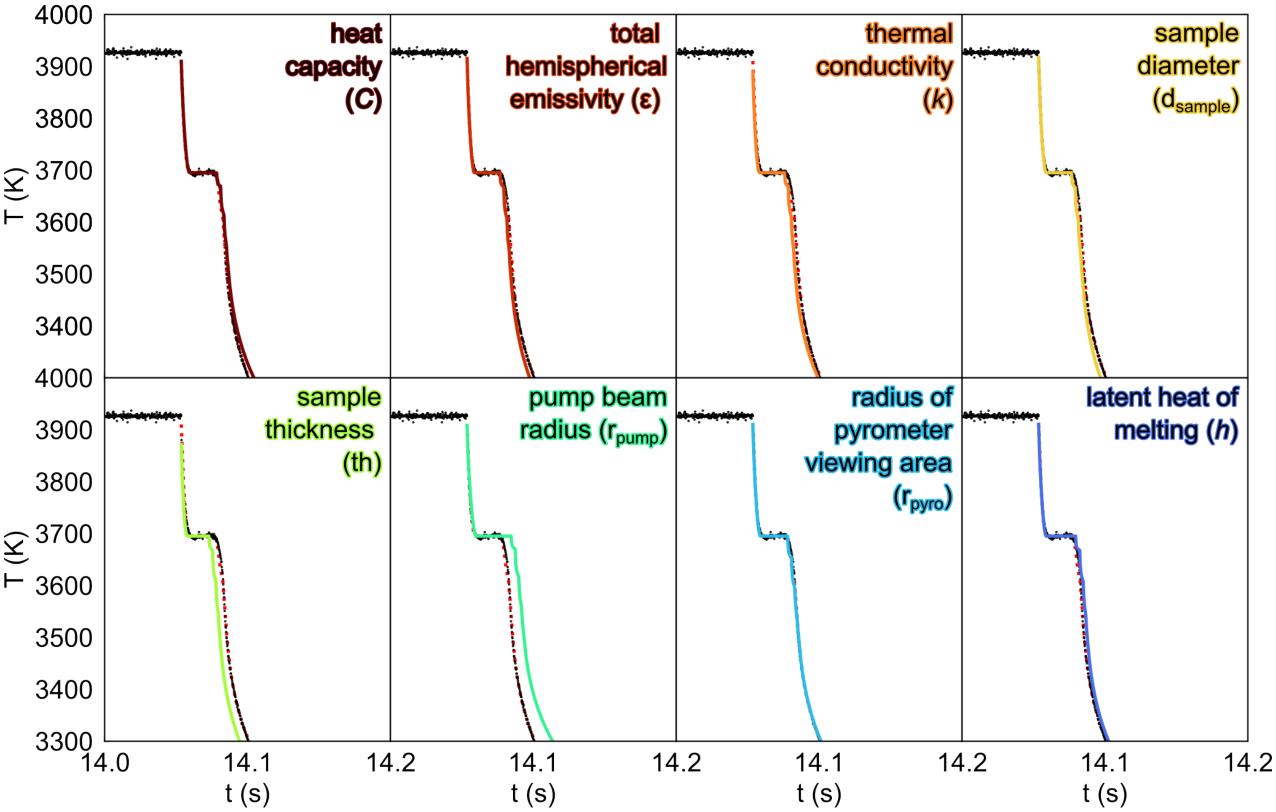

FIGURE 8.11: To explore the sensitivity of each parameter on the fitted resolidification plateau, each parameter is perturbed by 10%. The pump absorption parameter is refit using the steady-state temperature, and the resolidification plateau is modeled. In some cases, the plateau barely changes (e.g., viewed pyrometer area, heat capacity, ε), implying error or simplifying assumptions in these parameters may not drastically affect the fitted h_f. In some cases, the change is large (e.g., pump laser beam diameter, as a larger beam yields a larger melt pool) meaning these parameters must be carefully quantified. In all cases, the trends can be explained, e.g., increasing ε and K increases heat flux away from the melt pool, reducing the plateau duration. Each parameter's sensitivity is discussed briefly in Table 8.1.

TABLE 8.1: The trends in Figure 8.11 may not always be intuitive, so each parameter's sensitivity is explained briefly here.

Parameter	Observation	Explanation
heat capacity (C)	no change in plateau size. shallower post-solidification decay	Modeling melting via $T_{effective} = h/C$ would seem to imply an increase in C should yield a decrease in the plateau size (this is not the case). Conversely, one could think in terms of energy removal from the melt pool; a high C means more energy is stored in the melt pool, more energy must be removed, and one should expect a larger plateau. C is an energy storage property however, not a transport property. h_f can be thought of as an energy-*generation* property within this context however. The temperature rise of a unit of material during a timestep ΔT is calculated from energy flux Q divided by heat capacity C, and C in the denominator of both $T_{effective}$ and ΔT will cancel. Prior to melt pool resolidification, the melt pool temperature equilibrates quickly (uniform T) meaning transport within the melt pool is minimal and constant (insensitivity to C), and transport outside the melt pool merely sees the melt pool as a constant-T source (insensitive to C).
total hemispherical emissivity (ε_t)	reduction in plateau size, steeper decay	Increased flux away from melt pool results in faster resolidification, and faster cooling.
thermal conductivity (K)	reduction in plateau size, steeper decay	Increased flux away from melt pool results in faster resolidification, and faster cooling.
sample diameter (d_{sample})	slight reduction in plateau size	Changes to the sample geometry affect the relative contributions of $Q_{conductive}$ vs $Q_{radiative}$, where $Q_{conductive}$ is larger. Higher $Q_{conductive}$ due to additional material is slightly canceled out by the availability of larger surface area for radiation. While the net heat removed from the sample is entirely radiative, the removal of the heat from the melt pool specifically depends on both conduction and radiation.
sample thickness (th)	large reduction in plateau size	$Q_{radiative}$ on the back side of the sample is larger than $Q_{radiative}$ out the sides, so a change in thickness has a larger effect vs a change in radius.
pump beam radius (r_{pump})	great increase in plateau size	A larger pump beam yields a larger melt pool. Time of resolidification is directly proportional to pool size.
radius of pyrometer viewing area (r_{pyro}	no change	Pyrometer is viewing a relatively small area (0.8 mm diameter) as compared to the melt pool size ($\sim$ 3.5 mm diameter), yielding a constant temperature reading once the pool has equilibrated in temperature. The only change occurs once the melt front passes into view.
latent heat of fusion (h_f)	increase in plateau size, no change in decay	Increasing the energy stored in the phase change means more energy is released, delaying solidification. h_f only affects phase transition, not thermal transport.

heat capacity data was again taken from Touloukian *et al.* [202, 203], assuming a density of 10.2 Mg m^{-3}. Given the lower temperatures experienced during the molybdenum experiment and slightly lower overall emissivity, I found a constant emissivity (0.36) to be sufficient (a value of 0.33 was found at the pyrometer wavelength). I found a fitted enthalpy of fusion value of 3.86 GJ m^{-3} (378 J g^{-1} or 36.3 kJ mol^{-1}), with literature values ranging from 27.8 - 35.1 kJ mol^{-1} [204, 206].

Thermoreflectance results - PureTemp^{TM}37 PCM

I next present thermoreflectance results on the commercially-available PCM (PureTemp^{TM} PCM-37, T_{melt}=37 °C). My sample consisted of an 80 nm aluminum transducer deposited on a glass slide, with the PCM melted on the aluminum surface using a hot plate. The aluminum transducer was deposited via electron-beam evaporation, with the thermal conductivity determined from four point probe electrical resistivity measurements and the Wiedemann-Franz relation (163±2 W m^{-1} K^{-1}), and heat capacity was assumed from Touloukian *et al.* [203]. The pump/probe laser beams were both directed at the aluminum surface through the glass, meaning bidirectional thermal modeling was required [207, 208]. The aluminum transducer served to isolate pump absorption to a finite depth in the sample, and provided an optically-reflective surface for the probe laser beam. Direct thermoreflectance measurements on reflective phase-change samples may be possible, however a changing thermoreflectance coefficient upon melting will greatly complicate analysis. Similarly, fluid motion within the melt pool causing deflection of the probe beam could affect the thermoreflectance response. For the PCM sample stack, no phase change occurred for the aluminum over the $\sim$ 20 °C temperature perturbations applied, and the glass slide ensured an optically-smooth and stationary reflective surface was maintained throughout the experiment. Thermal conductivity and heat capacity values for the PCM are provided by the supplier (0.25 W m^{-1} K^{-1} and 2.03 MJ m^{-3} K^{-1} for the solid state, 0.15 W m^{-1} K^{-1} and 2.21 MJ m^{-3} K^{-1} for molten). The glass thermal conductivity has been measured previously at 1.35 W m^{-1} K^{-1}.

The enthalpy of fusion of 210 J g^{-1} (or 176 GJ m^{-3}) as provided by the manufacturer fits the data well, however damping of the resolidification signal from the transducer limits the measurement sensitivity to the enthalpy of fusion. Thermal spreading in the transducer yields a larger effective pump beam spot size, and cyclic heating means the steady state heating of the system [195] may prevent full resolidification (depending on laser spot sizes and modulation frequency). The use of a thinner or lower conductivity transducer may help mitigate some of these effects, yielding a more pronounced resolidification plateau, with better sensitivity to enthalpy of fusion. More abrupt modulation of the pump laser power would also help obtain a more clear resolidification signature. The PWA-acquired thermoreflectance signal is also extremely noisy compared to the high-temperature pyrometry measurements, since thermoreflectance coefficients are small [19], and since the experiments occur at lower temperatures with lower temperature perturbations. In Figure 8.12, the data was smoothed using a Gaussian function. Better laser stability, electronic modulation (as opposed to mechanically chopped), and selection of the transducer based on the thermoreflectance coefficient at the probe laser wavelength [19] could all help to increase the signal to noise of the experiment. The PWA signal was also normalized (with arbitrary scaling and shifting allowed for alignment to the model), however the use of a reference sample (as in SSTR [17]) could mean this is avoided, which would increase the measurement sensitivity to small changes resulting from melting.

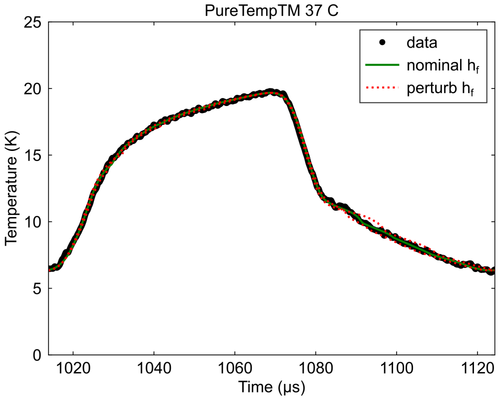

FIGURE 8.12: An a-SiO$_2$/Aluminum/PCM sample stack was measured (pumped/probed through the a-SiO$_2$), with the resolidification plateau visible in the data. When applying perturbations on h_f (scaling by a factor of 2, dotted red curves), slight changes in the modeled curves were observed, however the experiment had low sensitivity to h_f (little change in the curve following a change in h_f). Modeling shows that in-plane heat spreading served to obfuscate the signal acquired, so I would recommend the use of thinner and lower-conductivity transducers for future experiments.

8.5 Relevant publications

I have thus presented two apparatus for non-contact laser-based measurement of the enthalpy of fusion (h_f), both of which acquire a time-dependent reading of a sample's temperature as it passes through a phase change. At high temperature, pyrometry can be used to acquire the signal, whereas thermoreflectance can be used at lower temperature. Through rigorous thermal modeling, I show extraction of h_f from the thermal arrest on resolidification, including discussion on the additional measurement parameters requiring consideration. For example, accurately capturing the size of the melt pool is critical in both experiments for obtaining the correct results, meaning characterization of the related parameters (e.g., K, ε, thermal spreading in the transducer) or measurement of the melt pool separately is key. For the high-temperature experiments, I showed extraction of h_f on both tungsten and molybdenum, however the low temperature experiment merely showed a reasonable agreement between model and data. This was due to experimental noise and thermal spreading in the transducer, which obfuscates the resolidification signature and yields poor sensitivity. Both of these issues would need to be addressed for future measurements.

A manuscript for this work is nearing completion, and I expect to submit shortly. (T. W. Pfeifer, S. Bender, H. B. Schonfeld, S. H. Makarem, K. Boboridis, L. Vlahovic, D. Robba, and P. E. Hopkins; "Development of a microscale calorimetry technique for the measurement of enthalpy of fusion"

Chapter 9

Conclusions

The measurement of nanoscale thermal properties remains critical for accurate modeling and materials engineering for a variety of modern and future technology. Even macroscale properties are often dominated by nanoscale effects such as defect scattering, phonon-phonon scattering, and boundary scattering. I have thus presented a number of projects, falling under three distinct thrusts, aimed at pushing the study of nanoscale thermal properties forwards. These include “Development of new analysis methodologies for existing measurement techniques”, “Advancements to computational techniques”, and “Development of new experimental metrologies”.

Before making modifications to existing thermoreflectance techniques, a thorough understanding of the drawbacks and limitations was required. In the chapter titled “Measurement uncertainty and systematic error”, I explored the sources of uncertainty and error both generally and through specific examples. In most measurements (not limited to thermoreflectance experiments), the quantitative extraction of results depends on assumptions and measurements of various input parameters. This includes both experimental parameters (e.g., focused laser spot sizes) and sample properties (e.g., transducer thermal conductivity or thickness), and any uncertainty in these will propagate to an uncertainty in the final measured values. There are also various sources of systematic error, such as potential undetected apparatus misalignment. For example, imperfectly overlapped pump and probe beams will result in scaling of the data, and misalignment down a mechanical TDTR delay stage will yield a systematic adjustment to the slope or curvature of the thermal decay. The assumption that the apparatus returns the exactly correct curve is dependent on the alignment and calibration procedure. No calibration procedure is perfect (e.g., we measure calibration samples and accept a range of fitted values), meaning some flexibility in the fit due to uncaught systematic error should be included. Both of these concepts are critical for recognizing the limitations of our measurements, understanding where additional measurements (or better alignment and calibration procedures) may be necessary, and accurately relaying our uncertainty in publication.

I then applied some of these concepts to develop a depth-dependent thermal conductivity fitting procedure, which I used for fitting a series of irradiated silicon samples ("Measurement of depth-varying thermal conductivity"). By applying a Gaussian function to the thermal conductivity profile, I was able to fit for the minimum thermal conductivity, radiation damage broadening, and the location of the lowest thermal conductivity. Ordinarily, fitting for this many unknowns (3 Gaussian parameters, plus the transducer/silicon TBR) would not be permitted, however I showed that multi-frequency TDTR could adequately resolve all unknowns. Proving this required probing the entire 4D parameter space, and led to the development of a new methodology for performing contour analysis (by sweeping through values for a single unknown and fitting for the remaining). The ability to measure the spatially-resolved (through depth) conductivity profile also enabled measurement of unique structures such as a partially-amorphous/partially-crystalline region where the effects of boundary scattering and defect scattering could be separated.

Having seen the power of multi-frequency TDTR fitting, I next explored scenarios where the traditional measurement techniques fail, exploring both buried interfaces and highly-anisotropic samples. In both scenarios, there are too many unknown thermal properties for TDTR to sufficiently extract all parameters. In the case of buried interfaces, this includes the film K, and transducer/film and film/substrate TBR, and for anisotropic samples, the unknowns include the transducer/film TBR and $K_{inplane}$ vs. $K_{throughplane}$. While 3 unknowns may not seem like too many, rigorous contour analysis shows that the parameters of interest can not be accurately resolved for certain material systems. A similar challenge might include the use of SSTR for any sample with two or more unknowns. In the chapter titled "An algorithm for multi-measurement data fitting" I addressed these concerns by developing a methodology for fitting data from multiple sources. I began by demonstrating a multi-frequency SSTR approach for extracting two unknowns, which I applied to fitting for K and TBR or K and C. This offers an alternative to TDTR (simpler and faster measurements), and I also showed it exceeding the capabilities of TDTR for resolving TBR. I also showed the simultaneous fitting of TDTR and SSTR data for Aluminum/diamond/AlGaN to measure the diamond/AlGaN interface, and AlN/AlGaN superlattices to measure both the in-plane and through-plane thermal conductivity. In both scenarios, no other experimental technique would be able to resolve the necessary parameters with reasonable error.

I next applied some of these concepts to the study of TBR on GaN, which was also my first foray into molecular dynamics simulations. In the chapter titled "Measurement and simulation of the effects of irradiation on Thermal Boundary Resistance", I designed a study in which GaN was irradiated with multiple ions (C, Ga, N) to study the effects of impurities and structural disorder. Aluminum transducers were deposited, and the Al/GaN TBR was measured via TDTR, with combined magnitude+ratio fitting used to ensure reasonable error was acquired. To characterize spatial variability across the samples, SSTR maps were also performed. On the computational side, I ran MD on a toy silicon / heavy-silicon system, allowing exploration of potential changes in the vibrational density of states (vibrational populations present) and spectral heat flux (vibrations carrying heat). Structural defects were added to the simulations (rather than to compositional, as has been explored previously), and the TBR was extracted. In both experiment and simulation, I observed a universal reduction in TBR following the introduction of defects, which I attributed to increases in scattering. While scattering inhibits heat flow in bulk solids, the interfacial thermal resistance is fundamentally a product of the requirement for energy to be converted between vibrational populations. Increased scattering (including within the bulk of the sample or simulation, rather than localized at the interface) thus serves to accelerate this energy conversion, reducing the TBR.

I was next curious if targeted increases in scattering, through direct phonon excitation, could be used to reduce TBR. In the chapter titled "Phonon pumping in MD: Exploring the possibility of switchable Thermal Boundary Resistance", I experimented with pumping specific phonon modes in MD. In theory, if phonon modes could be artificially brought far out of equilibrium, the scattering associated with these modes could be increased, and a reduction in TBR might be obtained. I tested this by applying a sinusoidally-varying force field in LAMMPS. I began by demonstrating the ability to couple to (and excite) specific phonon modes by monitoring the temperature rise when a specific frequency and wavelength excitation was applied. To explore the effects on TBR, the same excitation was applied within NEMD. Unfortunately, inherent scattering rates within even the most highly-harmonic systems (e.g., Stillinger-Weber silicon) are high enough such that it is difficult to excite specific modes measurably out of equilibrium without heating the system substantially. No meaningful reduction in TBR was thus observed (outside of uncertainty, nor beyond the reduction in TBR from merely heating the system). Computational advances from this study may serve to guide future time-resolved out-of-equilibrium MD simulations however.

With irradiation damage fresh in mind from the irradiated GaN study, I wanted to explore the use of thermoreflectance as a tool for the detection of surface damage. In the chapter titled "Using thermoreflectance to detect surface defects", I designed a study in which a series of samples were Focus Ion Beam (FIB) milled, and I mapped the surrounding area using both TDTR and SSTR. I showed that the TBR was affected up to 300 µm away from the milled region, and more surprisingly, the thermoreflectance response was affected beyond 1 mm away. Additional measurements (including profilometry, secondary ion mass spectroscopy, scanning transmission electron microscopy, and energy dispersive x-ray spectroscopy) were also performed, with all signs pointing to an ion-repulsion mechanism within the ion beam itself. For an ion beam with a distribution of ion energy, lower-energy (slower) ions are pushed out of the focused ion beam, which results in an extremely broad distribution of surface damage. This study also showed that thermoreflectance can serve as a highly sensitive tool (assuming the right material systems are being considered) for the detection of surface damage. This is because dopant-levels of contamination can serve to change optical properties (including both absorption and temperature-dependent changes in reflectivity), which can be detected via pump-probe experiments.

Finally, I applied thermoreflectance to calorimetry measurements, using laser-based experiments as a tool for the measurement of the enthalpy of melting. In general, a brief thermal arrest will occur as a sample passes through a phase transition, meaning time-dependent data can be used to determine the latent heat. In the chapter titled "Microscale calorimetry: Measuring enthalpy of phase change", I developed the computational tools necessary to analyze both high-temperature pyrometry-based and lower-temperature thermoreflectance-based melting data. I also modified an existing SSTR apparatus, incorporating a high-power laser for melting, showing the acquisition of melting data using the lock-in amplifier's periodic waveform analyzer (PWA) function. In the case of both high-temperature pyrometry and low-temperature thermoreflectance, extensive discussion is also included on how to properly characterize all unknowns (including temperature dependent properties) as required to allow for extraction of latent heat.

Several of these projects also offered opportunities for future research. Other applications for the depth-varying thermal conductivity profiling would be interesting. For example, a diffusion gradient between two materials will have every alloy composition between 0-100% of each material, meaning the "bathtub curve" [95, 96, 209] for alloy composition could be mapped. Similarly, spatially-varying grain size and defect composition can result from growth [210], and accurate characterization of these effects is critical for understanding growth effects on thermal properties.

In the study of irradiated GaN, I highlighted the importance of scattering in the conversion of energy between phonon populations (including between bulk and interfacial populations). It would be interesting to explore how the scattering effect on TBR translates to other materials. For example, one might expect a stronger effect in highly-harmonic materials (where the irradiation damage can most strongly increase the scattering). Studies on the highest-quality diamond interfaces, with and without the introduction of defects, might show an even more pronounced effect, and this could be a key to solving the issues of thermal dissipation in diamond semiconductor devices. I also identified a spatially-varying set of vibrations which appeared to be standing waves with the interface pinning the motion of specific monolayers. This would be fascinating to explore further, as it has not been observed elsewhere to my knowledge.

While exploring the direct pumping of phonons in MD, the requirement for time-averaging (to extract TBR from NEMD), and the desire to couple to phonons in the system (thus potentially heating the system) were fundamentally at odds. This meant I was unable to drive specific phonons in the system far out of equilibrium (and the system was simply heated), and no targeted scattering-induced reduction in TBR could be observed. Future study might try to emulate a short-pulsed laser excitation experiment however, with an excitation applied at a much higher magnitude for a much shorter duration. Alternate strategies for extracting an instantaneous TBR would be required, or the evolution of phonon populations could be observed. I have briefly experimented with Spectral Energy Density (SED) calculations on a time-resolved basis (using a windowed series of timesteps), and I believe it should be possible to use this to track the evolution of out-of-equilibrium excitation and scattering pathways. After a specific mode is driven out of equilibrium, the mode should be visible in a time windowed SED calculation. For subsequent time windows, neighboring modes may appear with an increased population, indicating their participation in the thermalization of the originally-pumped mode.

For laser-based calorimetry measurements, further development is required to clean up the thermoreflectance signal and achieve higher sensitivity to the latent heat. For example, the use of the traditional 80 nm aluminum transducer led to substantial in-plane thermal spreading, which muddled the resolidification signature in the data. Other transducer materials (thinner, and with lower thermal conductivity) should be explored. For high-temperature measurements, multiple small adjustments to the experiment could also help avoid complications from unknown thermal parameters. Thermal dissipation from the melt pool has a significant effect on the resolidification plateau duration, so characterization of these is critical. The use of an unfocused heating beam to bring the sample to uniform elevated temperature, and a second tightly-focused pump laser to initiate localized melting, would minimize sensitivity to temperature dependent thermal conductivity (K), heat capacity (C), and total hemispherical emissivity (ε_t). Additional characterization to measure the size of the melt pool during the experiment would also help reduce uncertainty. If sufficient signal and uncertainty can be obtained, it would be interesting to then apply these measurements to other types of phase changed beyond melting.

9.0.1 Publications

Below is a list of published (or in progress) publications for which I have been involved.

- **T. W. Pfeifer**, E. R. Hoglund, A. V. Ievlev, P. E. Hopkins, “Optical Pump-Probe Measurements of Point Defects Resulting from Focused Ion Beam Milling” *Under review: Advanced Engineering Materials*

- K. Ma, R. Abernethy, S. von Tiedemann, N. Peng, G. Greaves, A. H. Mir, C. Hofer, **T. W. Pfeifer**, K. Sun, L. Wang, P. Ferreirós, C. Hardie, E.R. Hoglund, P.E. Hopkins, A. Knowles, “Intermetallic Dispersion-Strengthened Ferritic Superalloys with Exceptional Resistance to Radiation-Induced Hardening” *Under review: Science Advances*

- H. T. Aller, **T. W. Pfeifer**, A. Chaney, K. Averett, T. Asel, Z. Engel, A. Khan, P. E. Hopkins, A. Doolittle, S. Mou, S. Graham, “The Impact of Device Architecture on the Thermal Response of AlN/AlGaN Digital Alloy Field-Effect Transistors” *Under review: Applied Thermal Engineering*

- K. Huynh, M. Liao, X. Yan, J. Tomko, **T. W. Pfeifer**, V. Dragoi, N Razek, E. Guiot,

R. Caulmilone, X. Pan, P. E. Hopkins, M. Goorsky, “Stability of Interface Morphology and Thermal Boundary Conductance of Direct Wafer Bonded GaN/Si Heterojunction Interfaces Annealed at Growth and Annealing Temperatures” *Under review: ACS Applied Materials and Interfaces*

- **T. W. Pfeifer**, H. B. Schonfeld, H. T. Aller, E. A. Scott, J. T. Gaskins, D. H. Olson, J. Braun, S. Graham, P. E. Hopkins “Limitations and Advances in Optical Thermometry: Nanoscale Resistances, High Thermal Conductivity Materials, and Ultrahigh Temperatures” *Recently accepted: Annual Review of Materials Science*

- W. Hutchins, J. A. Tomko, D. M. Hirt, J. R. Matson, K. Diaz-Granados, M. He, **T. W. Pfeifer**, S. Zare, J. Li, J. Edgar,J. P. Maria, J. D. Caldwell, P. E. Hopkins, “Ultrafast Evanescent Heat Transfer across Solid Interfaces via Hyperbolic Phonon-Polaritons in Hexagonal Boron Nitride” *Nature Materials* DOI: 10.1038/s41563-025-02154-5

- M. Milich, H. B. Schonfeld, C. Miller, L. Doumaux, M. Ridley, **T. W. Pfeifer**, W. Riffe, D. Robba, L. Vlahovic, K. Boboridis, R. J. M. Konings, A. Chamberlain, E. Opila, P. E. Hopkins “Melting Temperature, Emissivity, and Thermal Conductivity of Rare-Earth Silicates for Thermal and Environmental Barrier Coatings” *Scripta Materialia* (2025) DOI: 10.1016/j.scriptamat.2025.116576

- M. R. Islam, P. Karna, J. A. Tomko, E. R. Hoglund, D. M. Hirt, M. S. B. Hoque, S. Zare, K. Aryana, **T. W. Pfeifer**, C. Jezewski, A. Giri, C. D. Landon, S. W. King, P. E. Hopkins “Evaluating Size Effects on the Thermal Conductivity and Electron-Phonon Scattering Rates of Copper Thin Films for Experimental Validation of Matthiessen’s Rule” *Nature Communications* (2024) DOI: 10.1038/s41467-024-53441-9

- H. T. Aller, **T. W. Pfeifer**, A. Mamun, K. Huynh, M. Tadjer, T. Feygelson, K. Hobart, T. Anderson, B. Pate, A. Jacobs, J. S. Lundh, M. Goorsky, A. Khan, P. E. Hopkins, S. Graham, “Low Thermal Resistance of Diamond-AlGaN Interfaces Achieved Using Carbide Interlayers” *Advanced Materials Interfaces* (2024) DOI:

10.1002/admi.202400575

- M. Malakoutian, K. Woo, D. Rich, R. Mandia, X. Zheng, A. Kasperovich, D. Saraswat, R. Soman, Y. Jo, **T. W. Pfeifer**, T. Hwang, H. Aller, J. Kim, J. Lyu, J. K. Mabrey, T. A. Rodriguez, J. Pomeroy, P. E. Hopkins, S. Graham, D. J. Smith, S. Mitra, K. Cho, M. Kuball, S. Chowdhury, "Lossless Phonon Transition Through Interfaces with Diamond" *Advanced Electronic Materials* (2024) DOI: 10.1002/aelm.202400146

- **T. W. Pfeifer**, H. T. Aller, E. R. Hoglund, E. A. Scott, J. A. Tomko, H. Ahmad, A. Doolittle, A. Giri, K. Hattar, A. J. H. McGaughey, P. E. Hopkins, "Ion Irradiation Induced Crystalline Disorder Accelerates Interfacial Phonon Conversion and Reduces Thermal Boundary Resistance" *Physical Review B* (2024) DOI: 10.1103/PhysRevB.109.165421

- K. Woo, M. Malakoutian, Y. Jo, X. Zheng, **T. W. Pfeifer**, R. Mandia, T. Huang, H. T. Aller, D. Field, A. Kasperovich, D. Saraswat, D. Smith, P. E. Hopkins, S. Graham, M. Kuball, K. Cho, S. Chowdhury "Interlayer Engineering to Achieve <1 m^2 K GW^{-1} Thermal Boundary Resistances to Diamond for Effective Device Cooling" *IEDM* (2023) DOI: 10.1109/IEDM45741.2023.10413734

- K. Huynh, Y. Wang, M. E. Liao, **T. W. Pfeifer**, J. A. Tomko, E. A. Scott, K. Hattar, P. E. Hopkins, M. S. Goorsky, "Depth-Dependent Recovery of Thermal Conductivity After Recrystallization of Amorphous Silicon" *Journal of Applied Physics* (2023) DOI: 10.1063/5.0133548

- E. R. Hoglund, D. Bao, A. O'Hara, **T. W. Pfeifer**, Md S. Bin Hoque, S. Makarem, J. M. Howe, S. T. Pantelides, P. E. Hopkins, J. A. Hachtel, "Direct Visualization of Localized Vibrations At Complex Grain Boundaries" *Advanced Materials* (2023) DOI: 10.1002/adma.202208920

- **T. W. Pfeifer**, J. A. Tomko, E. R. Hoglund, E. A. Scott, K. Huynh, M. Liao, K. Hattar, M. Goorsky, P. E. Hopkins, "Measuring Sub-surface Spatially Varying Thermal

Conductivity of Silicon Implanted with Krypton" *Journal of Applied Physics: Ion Irradiation, Editor's Pick* (2022) DOI: 10.1063/5.0094876

- K. Aryana, J. A. Tomko, R. Gao, E. R. Hoglund, T. Mimura, S. Makarem, A. Salanova, Md. S. B. Hoque, **T. W. Pfeifer**, D. H. Olson, J. L. Braun, J. Nag, J. C. Read, J. M. Howe, E. J. Opila, L. W. Martin, J. F. Ihlefeld, P. E. Hopkins, "Observation of Solid-state Bidirectional Thermal Conductivity Switching in Antiferroelectric Lead Zirconate (PbZrO3)" *Nature Communications* (2022) DOI: 10.1038/s41467-022-29023-y

- **T W. Pfeifer**, H. A. Walker, H. T. Aller, S. Graham, S. Pantelides, J. A. Hachtel, P. E. Hopkins, E. R. Hoglund, "Understanding phonon selection and interference in momentum-resolved electron energy loss spectroscopy" *In Preparation* DOI: 10.48550/arXiv.2503.09792

- **T. W. Pfeifer**, S. Bender, H. B. Schonfeld, S. H. Makarem, K. Boboridis, L. Vlahovic, D. Robba, P. E. Hopkins, "Development of a Laser-based Microscale Calorimetry Technique for the Measurement of Enthalpy of Fusion" *In Preparation*

- B. Carson, K. Hyunh, **T. W. Pfeifer**, X. Yan, G. Jernigan, K. Hobart, M. Goorsky, P. E. Hopkins, "Dislocation Mediated Corrugation of Ge-Si (001) Interfaces" *In Preparation*

Bibliography

[1] P. Šichman, R. Stoklas, S. Hasenöhrl, D. Gregušová, M. Ťapajna, B. Hudec, Haščík, T. Hashizume, A. Chvála, A. Šatka, and J. Kuzmík, "Vertical gan transistor with semi-insulating channel," *physica status solidi (a)*, vol. 220, no. 16, p. 2 200 776, 2023. DOI: https://doi.org/10.1002/pssa.202200776. eprint: https://onlinelibrary.wiley.com/doi/pdf/10.1002/pssa.202200776. [Online]. Available: https://onlinelibrary.wiley.com/doi/abs/10.1002/pssa.202200776.

[2] K. Aryana, J. A. Tomko, R. Gao, E. R. Hoglund, T. Mimura, S. Makarem, A. Salanova, M. S. B. Hoque, T. W. Pfeifer, D. H. Olson, J. L. Braun, J. Nag, J. C. Read, J. M. Howe, E. J. Opila, L. W. Martin, J. F. Ihlefeld, and P. E. Hopkins, "Observation of solid-state bidirectional thermal conductivity switching in antiferroelectric lead zirconate (PbZrO3)," *Nature Communications*, vol. 13, no. 1, pp. 1–9, 2022, ISSN: 20411723. DOI: 10.1038/s41467-022-29023-y.

[3] C. Kittel, *Introduction to Solid State Physics*. John Wiley & Sons, 2005.

[4] G. P. Srivastava, *The Physics of Phonons: Second Edition*, ISBN: 9780367685263.

[5] G. Chen, *Nanoscale Energy Transport and Conversion: A Parallel Treatment of Electrons, Molecules, Phonons, and Photons* (MIT-Pappalardo Series in Mechanical Engineering). Oxford University Press, 2005, ISBN: 9780199774685. [Online]. Available: https://books.google.com/books?id=M3n3lUJpYDYC.

[6] G. Slack, "Nonmetallic crystals with high thermal conductivity," *Journal of Physics and Chemistry of Solids*, vol. 34, no. 2, pp. 321–335, 1973, ISSN: 0022-3697. DOI: https://doi.org/10.1016/0022-3697(73)90092-9. [Online]. Available: https://www.sciencedirect.com/science/article/pii/0022369773900929.

[7] G. Yang, P. R. Romeo, A. Apostoluk, and B. Vilquin, "First principles study on the lattice thermal conductivity of α-phase Ga2O3," *Journal of Vacuum Science & Technology A*, vol. 40, no. 5, 2022, ISSN: 0734-2101. DOI: 10.1116/6.0001870.

[8] A. Ward and D. A. Broido, "Intrinsic phonon relaxation times from first-principles studies of the thermal conductivities of Si and Ge," *Physical Review B - Condensed Matter and Materials Physics*, vol. 81, no. 8, pp. 1–5, 2010, ISSN: 10980121. DOI: 10.1103/PhysRevB.81.085205.

[9] L. Lindsay, D. A. Broido, and T. L. Reinecke, "First-principles determination of ultrahigh thermal conductivity of boron arsenide: A competitor for diamond?" *Physical Review Letters*, vol. 111, no. 2, pp. 1–5, 2013, ISSN: 00319007. DOI: `10.1103/PhysRevLett.111.025901`.

[10] A. Giri and P. E. Hopkins, "A Review of Experimental and Computational Advances in Thermal Boundary Conductance and Nanoscale Thermal Transport across Solid Interfaces," *Advanced Functional Materials*, vol. 30, no. 8, pp. 1–21, 2020, ISSN: 16163028. DOI: `10.1002/adfm.201903857`.

[11] E. T. Swartz and R. O. Pohl, "Thermal boundary resistance," *Reviews of Modern Physics*, vol. 61, no. 3, pp. 605–668, 1989, ISSN: 00346861. DOI: `10.1103/RevModPhys.61.605`.

[12] C. Monachon, L. Weber, and C. Dames, "Thermal Boundary Conductance: A Materials Science Perspective," *Annual Review of Materials Research*, vol. 46, pp. 433–463, 2016, ISSN: 15317331. DOI: `10.1146/annurev-matsci-070115-031719`.

[13] I. M. Khalatnikov, "Heat Exchange Between a Solid and Helium II," *Zhurnaleksperimental'noi i teoreticheskoi fiziki (Journal of Experimental and Theoretical Physics)*, vol. 22, pp. 687–704, 1952.

[14] W. A. Little, "The transport of heat between dissimilar solids at low temperatures," *Canadian Journal of Physics*, vol. 37, 1959. DOI: `10.1139/p59-037`.

[15] D. G. Cahill, "Analysis of heat flow in layered structures for time-domain thermoreflectance," *Review of Scientific Instruments*, vol. 75, no. 12, pp. 5119–5122, 2004, ISSN: 00346748. DOI: `10.1063/1.1819431`.

[16] A. J. Schmidt, R. Cheaito, and M. Chiesa, "A frequency-domain thermoreflectance method for the characterization of thermal properties," *Review of Scientific Instruments*, vol. 80, no. 9, 2009, ISSN: 00346748. DOI: `10.1063/1.3212673`.

[17] J. L. Braun, D. H. Olson, J. T. Gaskins, and P. E. Hopkins, "A steady-state thermoreflectance method to measure thermal conductivity," *Review of Scientific Instruments*, vol. 90, no. 2, 2019, ISSN: 10897623. DOI: `10.1063/1.5056182`.

[18] Y. Wang, V. Chauhan, Z. Hua, R. Schley, C. A. Dennett, D. Murray, M. Khafizov, G. Beausoleil, and D. H. Hurley, "A Square Pulse Thermoreflectance Technique for the Measurement of Thermal Properties," *International Journal of Thermophysics*, vol. 43, no. 4, pp. 1–24, 2022, ISSN: 15729567. DOI: `10.1007/s10765-021-02949-z`. [Online]. Available: `https://doi.org/10.1007/s10765-021-02949-z`.

[19] Y. Wang, J. Y. Park, Y. K. Koh, and D. G. Cahill, "Thermoreflectance of metal transducers for time-domain thermoreflectance," *Journal of Applied Physics*, vol. 108, no. 4, pp. 1–4, 2010, ISSN: 00218979. DOI: `10.1063/1.3457151`.

[20] E. L. Radue, J. A. Tomko, A. Giri, J. L. Braun, X. Zhou, O. V. Prezhdo, E. L. Runnerstrom, J. P. Maria, and P. E. Hopkins, "Hot Electron Thermoreflectance Coefficient of Gold during Electron-Phonon Nonequilibrium," *ACS Photonics*, vol. 5, no. 12, pp. 4880–4887, 2018, ISSN: 23304022. DOI: `10.1021/acsphotonics.8b01045`.

[21] Y. K. Koh and D. G. Cahill, "Frequency dependence of the thermal conductivity of semiconductor alloys," *Physical Review B - Condensed Matter and Materials Physics*, vol. 76, no. 7, pp. 1–5, 2007, ISSN: 10980121. DOI: `10.1103/PhysRevB.76.075207`.

[22] J. L. Braun and P. E. Hopkins, "Upper limit to the thermal penetration depth during modulated heating of multilayer thin films with pulsed and continuous wave lasers: A numerical study," *Journal of Applied Physics*, vol. 121, no. 17, pp. 1–13, 2017, ISSN: 10897550. DOI: `10.1063/1.4982915`.

[23] R. J. Warzoha, A. A. Wilson, B. F. Donovan, A. Clark, X. Cheng, L. An, and G. Feng, "Measurements of Thermal Resistance Across Buried Interfaces with Frequency-Domain Thermoreflectance and Microscale Confinement," *ACS Applied Materials and Interfaces*, 2024, ISSN: 19448252. DOI: `10.1021/acsami.4c05258`.

[24] N. Poopakdee, Z. Abdallah, J. W. Pomeroy, and M. Kuball, "In situ Thermoreflectance Characterization of Thermal Resistance in Multilayer Electronics Packaging," *ACS Applied Electronic Materials*, vol. 4, no. 4, pp. 1558–1566, 2022, ISSN: 26376113. DOI: `10.1021/acsaelm.1c01239`.

[25] J. P. Feser and D. G. Cahill, "Probing anisotropic heat transport using time-domain thermoreflectance with offset laser spots," *Review of Scientific Instruments*, vol. 83, no. 10, 2012, ISSN: 00346748. DOI: `10.1063/1.4757863`.

[26] P. Jiang, X. Qian, and R. Yang, "A new elliptical-beam method based on time-domain thermoreflectance (TDTR) to measure the in-plane anisotropic thermal conductivity and its comparison with the beam-offset method," *Review of Scientific Instruments*, vol. 89, no. 9, pp. 1–35, 2018, ISSN: 10897623. DOI: `10.1063/1.5029971`.

[27] L Wang, R Cheaito, J. L. Braun, A Giri, and P. E. Hopkins, "Thermal conductivity measurements of non-metals via combined time- and frequency-domain thermoreflectance without a metal film transducer," *Review of Scientific Instruments*, vol. 87, no. 9, 2016, ISSN: 10897623. DOI: `10.1063/1.4962711`. [Online]. Available: `http://dx.doi.org/10.1063/1.4962711`.

[28] X. Zheng, D. G. Cahill, R. Weaver, and J. C. Zhao, "Micron-scale measurements of the coefficient of thermal expansion by time-domain probe beam deflection," *Journal of Applied Physics*, vol. 104, no. 7, 2008, ISSN: 00218979. DOI: `10.1063/1.2988111`.

[29] J. L. Braun, C. M. Rost, M. Lim, A. Giri, D. H. Olson, G. N. Kotsonis, G. Stan, D. W. Brenner, J. P. Maria, and P. E. Hopkins, "Charge-induced disorder controls the thermal conductivity of entropy-stabilized oxides," *Advanced Materials*, vol. 30, no. 51, pp. 1–8, 2018, ISSN: 15214095. DOI: `10.1002/adma.201805004`.

[30] A. Giri, J. P. Niemelä, C. J. Szwejkowski, M. Karppinen, and P. E. Hopkins, "Reduction in thermal conductivity and tunable heat capacity of inorganic/organic hybrid superlattices," *Physical Review B*, vol. 93, no. 2, pp. 1–7, 2016, ISSN: 24699969. DOI: 10.1103/PhysRevB.93.024201.

[31] A. Giri, S. W. King, W. A. Lanford, A. B. Mei, D. Merrill, L. Li, R. Oviedo, J. Richards, D. H. Olson, J. L. Braun, J. T. Gaskins, F. Deangelis, A. Henry, and P. E. Hopkins, "Interfacial Defect Vibrations Enhance Thermal Transport in Amorphous Multilayers with Ultrahigh Thermal Boundary Conductance," *Advanced Materials*, vol. 30, no. 44, pp. 1–6, 2018, ISSN: 15214095. DOI: 10.1002/adma.201804097.

[32] H. Babaei, M. E. DeCoster, M. Jeong, Z. M. Hassan, T. Islamoglu, H. Baumgart, A. J. H. McGaughey, E. Redel, O. K. Farha, P. E. Hopkins, J. A. Malen, and C. E. Wilmer, "Observation of reduced thermal conductivity in a metal-organic framework due to the presence of adsorbates," *Nature Communications*, vol. 11, no. 1, 2020, ISSN: 20411723. DOI: 10.1038/s41467-020-17822-0. [Online]. Available: http://dx.doi.org/10.1038/s41467-020-17822-0.

[33] K. Chen, B. Song, N. K. Ravichandran, Q. Zheng, X. Chen, H. Lee, H. Sun, S. Li, G. A. G. U. Gamage, F. Tian, Z. Ding, Q. Song, A. Rai, H. Wu, P. Koirala, A. J. Schmidt, K. Watanabe, B. Lv, Z. Ren, L. Shi, D. G. Cahill, T. Taniguchi, D. Broido, and G. Chen, "Ultrahigh thermal conductivity in isotope-enriched cubic boron nitride," *Science*, vol. 367, no. 6477, pp. 555–559, 2020. DOI: 10.1126/science.aaz6149. eprint: https://www.science.org/doi/pdf/10.1126/science.aaz6149. [Online]. Available: https://www.science.org/doi/abs/10.1126/science.aaz6149.

[34] H. S. Carslaw and J. C. Jaeger, *Carslaw and Jaeger, Conduction of Heat in Solids.pdf*, 1959.

[35] P. K. Schelling, S. R. Phillpot, and P. Keblinski, "Comparison of atomic-level simulation methods for computing thermal conductivity," *Physical Review B - Condensed Matter and Materials Physics*, vol. 65, no. 14, pp. 1–12, 2002, ISSN: 1550235X. DOI: 10.1103/PhysRevB.65.144306.

[36] A. Giri, P. E. Hopkins, J. G. Wessel, and J. C. Duda, "Kapitza resistance and the thermal conductivity of amorphous superlattices," *Journal of Applied Physics*, vol. 118, no. 16, 2015, ISSN: 10897550. DOI: 10.1063/1.4934511. [Online]. Available: http://dx.doi.org/10.1063/1.4934511.

[37] A. Giri and P. E. Hopkins, "Giant reduction and tunability of the thermal conductivity of carbon nanotubes through low-frequency resonant modes," *Physical Review B*, vol. 98, no. 4, pp. 1–8, 2018, ISSN: 24699969. DOI: 10.1103/PhysRevB.98.045421.

[38] K. Gordiz and A. Henry, "Phonon transport at interfaces between different phases of silicon and germanium," *Journal of Applied Physics*, vol. 121, no. 2, 2017, ISSN: 10897550. DOI: 10.1063/1.4973573.

[39] D. P. Sellan, E. S. Landry, J. E. Turney, A. J. McGaughey, and C. H. Amon, "Size effects in molecular dynamics thermal conductivity predictions," *Physical Review B - Condensed Matter and Materials Physics*, vol. 81, no. 21, pp. 1–10, 2010, ISSN: 10980121. DOI: 10.1103/PhysRevB.81.214305.

[40] Z. Liang, A. Jain, A. J. McGaughey, and P. Keblinski, "Molecular simulations and lattice dynamics determination of Stillinger-Weber GaN thermal conductivity," *Journal of Applied Physics*, vol. 118, no. 12, 2015, ISSN: 10897550. DOI: 10.1063/1.4931673. [Online]. Available: http://dx.doi.org/10.1063/1.4931673.

[41] A. J. H. Mcgaughey and J. M. Larkin, "CHAPTER 3 PREDICTING PHONON PROPERTIES FROM EQUILIBRIUM MOLECULAR DYNAMICS SIMULATIONS 1 . 1 Motivation : Thermal Conductivity Prediction," *Annual Review of Heat Transfer*, vol. 17, no. N/A, pp. 49–87, 2014, ISSN: 1049-0787. [Online]. Available: http://www.dl.begellhouse.com/journals/5756967540dd1b03,forthcoming,6915.html%5Cnhttp://dl.begellhouse.com/journals/5756967540dd1b03,forthcoming,6915.html%5Cnhttp://www.dl.begellhouse.com/references/5756967540dd1b03,7deb9f2f1087a9e3,15a8c1a1156da7dd.html.

[42] W. Lv and A. Henry, "Direct calculation of modal contributions to thermal conductivity via Green-Kubo modal analysis," *New Journal of Physics*, vol. 18, no. 1, 2016, ISSN: 13672630. DOI: 10.1088/1367-2630/18/1/013028.

[43] J. A. Thomas, J. E. Turney, R. M. Iutzi, C. H. Amon, and A. J. H. McGaughey, "Predicting phonon dispersion relations and lifetimes from the spectral energy density," *Physical Review B - Condensed Matter and Materials Physics*, vol. 81, no. 8, pp. 1–4, 2010, ISSN: 10980121. DOI: 10.1103/PhysRevB.81.081411.

[44] Y. Chalopin, K. Esfarjani, A. Henry, S. Volz, and G. Chen, "Thermal interface conductance in Si/Ge superlattices by equilibrium molecular dynamics," *Physical Review B - Condensed Matter and Materials Physics*, vol. 85, no. 19, pp. 1–7, 2012, ISSN: 10980121. DOI: 10.1103/PhysRevB.85.195302.

[45] K. Sääskilahti, J. Oksanen, J. Tulkki, and S. Volz, "Role of anharmonic phonon scattering in the spectrally decomposed thermal conductance at planar interfaces," *Physical Review B - Condensed Matter and Materials Physics*, vol. 90, no. 13, pp. 1–8, 2014, ISSN: 1550235X. DOI: 10.1103/PhysRevB.90.134312. arXiv: 1405.3868.

[46] A. Giri, J. L. Braun, and P. E. Hopkins, "Implications of interfacial bond strength on the spectral contributions to thermal boundary conductance across solid, liquid, and gas interfaces: A molecular dynamics study," *Journal of Physical Chemistry C*, vol. 120, no. 43, pp. 24 847–24 856, 2016, ISSN: 19327455. DOI: 10.1021/acs.jpcc.6b08124.

[47] K. Sääskilahti, J. Oksanen, J. Tulkki, and S. Volz, "Spectral mapping of heat transfer mechanisms at liquid-solid interfaces," *Physical Review E*, vol. 93, no. 5, pp. 1–8, 2016, ISSN: 24700053. DOI: `10.1103/PhysRevE.93.052141`. arXiv: `1512.05914`.

[48] J. Yang, E. Ziade, and A. J. Schmidt, "Uncertainty analysis of thermoreflectance measurements," *Review of Scientific Instruments*, vol. 87, no. 1, 2016, ISSN: 10897623. DOI: `10.1063/1.4939671`. [Online]. Available: `http://dx.doi.org/10.1063/1.4939671`.

[49] Z. Xiang, Y. Pang, X. Qian, and R. Yang, "Machine learning reconstruction of depth-dependent thermal conductivity profile from pump-probe thermoreflectance signals," *Applied Physics Letters*, vol. 122, no. 14, 2023, ISSN: 00036951. DOI: `10.1063/5.0138060`.

[50] H. T. Aller, T. W. Pfeifer, A. Mamun, K. Huynh, M. Tadjer, T. Feygelson, K. Hobart, T. Anderson, B. Pate, A. Jacobs, J. S. Lundh, M. Goorsky, A. Khan, P. Hopkins, and S. Graham, "Low thermal resistance of diamond-algan interfaces achieved using carbide interlayers," *Advanced Materials Interfaces*, vol. n/a, no. n/a, p. 2 400 575, DOI: `https://doi.org/10.1002/admi.202400575`. eprint: `https://onlinelibrary.wiley.com/doi/pdf/10.1002/admi.202400575`. [Online]. Available: `https://onlinelibrary.wiley.com/doi/abs/10.1002/admi.202400575`.

[51] P. E. Hopkins, J. C. Duda, S. P. Clark, C. P. Hains, T. J. Rotter, L. M. Phinney, and G. Balakrishnan, "Effect of dislocation density on thermal boundary conductance across GaSb/GaAs interfaces," *Applied Physics Letters*, vol. 98, no. 16, p. 161 913, Apr. 2011, ISSN: 0003-6951. DOI: `10.1063/1.3581041`. eprint: `https://pubs.aip.org/aip/apl/article-pdf/doi/10.1063/1.3581041/14448749/161913\_1\_online.pdf`. [Online]. Available: `https://doi.org/10.1063/1.3581041`.

[52] H. Sun, R. B. Simon, J. W. Pomeroy, D. Francis, F. Faili, D. J. Twitchen, and M. Kuball, "Reducing GaN-on-diamond interfacial thermal resistance for high power transistor applications," *Applied Physics Letters*, vol. 106, no. 11, p. 111 906, Mar. 2015, ISSN: 0003-6951. DOI: `10.1063/1.4913430`. eprint: `https://pubs.aip.org/aip/apl/article-pdf/doi/10.1063/1.4913430/19755570/111906\_1\_online.pdf`. [Online]. Available: `https://doi.org/10.1063/1.4913430`.

[53] J. Anaya, T. Bai, Y. Wang, C. Li, M. Goorsky, T. L. Bougher, L. Yates, Z. Cheng, S. Graham, K. D. Hobart, T. I. Feygelson, M. J. Tadjer, T. J. Anderson, B. B. Pate, and M. Kuball, "Simultaneous determination of the lattice thermal conductivity and grain/grain thermal resistance in polycrystalline diamond," *Acta Materialia*, vol. 139, pp. 215–225, 2017, ISSN: 13596454. DOI: `10.1016/j.actamat.2017.08.007`.

[54] J. Cho, D. Francis, D. H. Altman, M. Asheghi, and K. E. Goodson, "Phonon conduction in GaN-diamond composite substrates," *Journal of Applied Physics*, vol. 121, no. 5, 2017, ISSN: 10897550. DOI: `10.1063/1.4975468`. [Online]. Available: `http://dx.doi.org/10.1063/1.4975468`.

[55] L. Yates, J. Anderson, X. Gu, C. Lee, T. Bai, M. Mecklenburg, T. Aoki, M. S. Goorsky, M. Kuball, E. L. Piner, and S. Graham, "Low thermal boundary resistance interfaces for gan-on-diamond devices," *ACS Applied Materials & Interfaces*, vol. 10, no. 28, pp. 24 302–24 309, 2018, PMID: 29939717. DOI: `10.1021/acsami.8b07014`. eprint: `https://doi.org/10.1021/acsami.8b07014`. [Online]. Available: `https://doi.org/10.1021/acsami.8b07014`.

[56] C. Yuan, J. W. Pomeroy, and M. Kuball, "Above bandgap thermoreflectance for non-invasive thermal characterization of GaN-based wafers," *Applied Physics Letters*, vol. 113, no. 10, 2018, ISSN: 00036951. DOI: `10.1063/1.5040100`. [Online]. Available: `http://dx.doi.org/10.1063/1.5040100`.

[57] Z. Cheng, L. Yates, J. Shi, M. J. Tadjer, K. D. Hobart, and S. Graham, "Thermal conductance across Ga2O3-diamond van der Waals heterogeneous interfaces," *APL Materials*, vol. 7, no. 3, p. 031 118, Mar. 2019, ISSN: 2166-532X. DOI: `10.1063/1.5089559`. eprint: `https://pubs.aip.org/aip/apm/article-pdf/doi/10.1063/1.5089559/14562426/031118\_1\_online.pdf`. [Online]. Available: `https://doi.org/10.1063/1.5089559`.

[58] Z. Cheng, T. Bai, J. Shi, T. Feng, Y. Wang, M. Mecklenburg, C. Li, K. D. Hobart, T. I. Feygelson, M. J. Tadjer, B. B. Pate, B. M. Foley, L. Yates, S. T. Pantelides, B. A. Cola, M. Goorsky, and S. Graham, "Tunable thermal energy transport across diamond membranes and diamond–si interfaces by nanoscale graphoepitaxy," *ACS Applied Materials & Interfaces*, vol. 11, no. 20, pp. 18 517–18 527, 2019. DOI: `10.1021/acsami.9b02234`.

[59] F. Mu, Z. Cheng, J. Shi, S. Shin, B. Xu, J. Shiomi, S. Graham, and T. Suga, "High Thermal Boundary Conductance across Bonded Heterogeneous GaN-SiC Interfaces," *ACS Applied Materials and Interfaces*, vol. 11, no. 36, pp. 33 428–33 434, 2019, ISSN: 19448252. DOI: `10.1021/acsami.9b10106`.

[60] Z. Cheng, F. Mu, L. Yates, T. Suga, and S. Graham, "Interfacial thermal conductance across room-temperature-bonded gan/diamond interfaces for gan-on-diamond devices," *ACS Applied Materials & Interfaces*, vol. 12, no. 7, pp. 8376–8384, 2020, PMID: 31986013. DOI: `10.1021/acsami.9b16959`. eprint: `https://doi.org/10.1021/acsami.9b16959`. [Online]. Available: `https://doi.org/10.1021/acsami.9b16959`.

[61] C. Yuan, R. Hanus, and S. Graham, "A review of thermoreflectance techniques for characterizing wide bandgap semiconductors' thermal properties and devices' temperatures," *Journal of Applied Physics*, vol. 132, no. 22, 2022, ISSN: 10897550. DOI: `10.1063/5.0122200`.

[62] P. E. Hopkins, L. M. Phinney, J. R. Serrano, and T. E. Beechem, "Effects of surface roughness and oxide layer on the thermal boundary conductance at aluminum/silicon interfaces," *Physical Review B - Condensed Matter and Materials Physics*, vol. 82, no. 8, pp. 1–5, 2010, ISSN: 10980121. DOI: `10.1103/PhysRevB.82.085307`.

[63] M. E. DeCoster, K. E. Meyer, B. D. Piercy, J. T. Gaskins, B. F. Donovan, A. Giri, N. A. Strnad, D. M. Potrepka, A. A. Wilson, M. D. Losego, and P. E. Hopkins, “Density and size effects on the thermal conductivity of atomic layer deposited TiO2 and Al2O3 thin films,” *Thin Solid Films*, vol. 650, no. February, pp. 71–77, 2018, ISSN: 00406090. DOI: `10.1016/j.tsf.2018.01.058`. [Online]. Available: `https://doi.org/10.1016/j.tsf.2018.01.058`.

[64] Y. K. Koh, M. H. Bae, D. G. Cahill, and E. Pop, “Heat conduction across monolayer and few-layer graphenes,” *Nano Letters*, vol. 10, no. 11, pp. 4363–4368, 2010, ISSN: 15306984. DOI: `10.1021/nl101790k`.

[65] M. V. Simkin and G. D. Mahan, “Minimum Thermal Conductivity of Superlattices,” *Physical Review Letters*, vol. 84, no. 5, pp. 927–930, 2000, ISSN: 00319007. DOI: `10.1103/PhysRevLett.84.927`. arXiv: `9907368 [cond-mat]`.

[66] J. Ravichandran, A. K. Yadav, R. Cheaito, P. B. Rossen, A. Soukiassian, S. J. Suresha, J. C. Duda, B. M. Foley, C. H. Lee, Y. Zhu, A. W. Lichtenberger, J. E. Moore, D. A. Muller, D. G. Schlom, P. E. Hopkins, A. Majumdar, R. Ramesh, and M. A. Zurbuchen, “Crossover from incoherent to coherent phonon scattering in epitaxial oxide superlattices,” *Nature Materials*, vol. 13, no. 2, pp. 168–172, 2014, ISSN: 14761122. DOI: `10.1038/nmat3826`.

[67] Y. K. Koh, Y. Cao, D. G. Cahill, and D. Jena, “Heat-transport mechanisms in superlattices,” *Advanced Functional Materials*, vol. 19, no. 4, pp. 610–615, 2009, ISSN: 1616301X. DOI: `10.1002/adfm.200800984`.

[68] J. F. Ziegler, M. D. Ziegler, and J. P. Biersack, “Nuclear Instruments and Methods in Physics Research B SRIM – The stopping and range of ions in matter (2010),” *Nuclear Inst. and Methods in Physics Research, B*, vol. 268, no. 11-12, pp. 1818–1823, 2010, ISSN: 0168-583X. DOI: `10.1016/j.nimb.2010.02.091`. [Online]. Available: `http://dx.doi.org/10.1016/j.nimb.2010.02.091`.

[69] E. A. Scott, K. Hattar, C. M. Rost, J. T. Gaskins, M. Fazli, C. Ganski, C. Li, T. Bai, Y. Wang, K. Esfarjani, M. Goorsky, and P. E. Hopkins, “Phonon scattering effects from point and extended defects on thermal conductivity studied via ion irradiation of crystals with self-impurities,” *Physical Review Materials*, vol. 2, no. 9, pp. 1–8, 2018, ISSN: 24759953. DOI: `10.1103/PhysRevMaterials.2.095001`.

[70] E. A. Scott, K. Hattar, E. J. Lang, K. Aryana, J. T. Gaskins, and P. E. Hopkins, “Reductions in the thermal conductivity of irradiated silicon governed by displacement damage,” *Physical Review B*, vol. 104, no. 13, pp. 1–5, 2021, ISSN: 2469-9950. DOI: `10.1103/physrevb.104.134306`.

[71] E. A. Scott, K. Hattar, J. L. Braun, C. M. Rost, J. T. Gaskins, T. Bai, Y. Wang, C. Ganski, M. Goorsky, and P. E. Hopkins, “Orders of magnitude reduction in the thermal conductivity of polycrystalline diamond through carbon, nitrogen, and oxygen ion implantation,” *Carbon*, vol. 157, pp. 97–105, 2020, ISSN: 00086223. DOI: `10.1016/j.carbon.2019.09.076`. [Online]. Available: `https://doi.org/10.1016/j.carbon.2019.09.076`.

[72] L. Pelaz, L. A. Marqús, and J. Barbolla, "Ion-beam-induced amorphization and recrystallization in silicon," *Journal of Applied Physics*, vol. 96, no. 11, pp. 5947–5976, 2004, ISSN: 00218979. DOI: 10.1063/1.1808484.

[73] K. R. Mok, M. Jaraiz, I. Martin-Bragado, J. E. Rubio, P. Castrillo, R. Pinacho, J. Barbolla, and M. P. Srinivasan, "Ion-beam amorphization of semiconductors: A physical model based on the amorphous pocket population," *Journal of Applied Physics*, vol. 98, no. 4, 2005, ISSN: 00218979. DOI: 10.1063/1.2014940.

[74] D. P. Hickey, K. S. Jones, and R. G. Elliman, "Amorphization and graphitization of single-crystal diamond - A transmission electron microscopy study," *Diamond and Related Materials*, vol. 18, no. 11, pp. 1353–1359, 2009, ISSN: 09259635. DOI: 10.1016/j.diamond.2009.08.012.

[75] S. K. Ghandhi, *VLSI Fabrication principles: Silicon and gallium arsenide*, 1995. DOI: 10.1016/0042-207x(95)80061-1.

[76] Y. K. Koh, Y. Cao, D. G. Cahill, and D. Jena, "Heat-transport mechanisms in superlattices," *Advanced Functional Materials*, vol. 19, no. 4, pp. 610–615, 2009, ISSN: 1616301X. DOI: 10.1002/adfm.200800984.

[77] P. B. Weisensee, J. P. Feser, and D. G. Cahill, "Effect of ion irradiation on the thermal conductivity of UO 2 and U 3 O 8 epitaxial layers," *Journal of Nuclear Materials*, vol. 443, no. 1-3, pp. 212–217, 2013, ISSN: 00223115. DOI: 10.1016/j.jnucmat.2013.07.021. [Online]. Available: http://dx.doi.org/10.1016/j.jnucmat.2013.07.021.

[78] R. Cheaito, C. S. Gorham, A. Misra, K. Hattar, and P. E. Hopkins, "Thermal conductivity measurements via time-domain thermoreflectance for the characterization of radiation induced damage," *Journal of Materials Research*, vol. 30, no. 9, pp. 1403–1412, 2015, ISSN: 20445326. DOI: 10.1557/jmr.2015.11.

[79] E. A. Scott, J. L. Braun, K. Hattar, J. D. Sugar, J. T. Gaskins, M. Goorsky, S. W. King, and P. E. Hopkins, "Probing thermal conductivity of subsurface, amorphous layers in irradiated diamond," *Journal of Applied Physics*, vol. 129, no. 5, 2021, ISSN: 10897550. DOI: 10.1063/5.0038972.

[80] A. X. Levander, T. Tong, K. M. Yu, J. Suh, D. Fu, R. Zhang, H. Lu, W. J. Schaff, O. Dubon, W. Walukiewicz, D. G. Cahill, and J. Wu, "Effects of point defects on thermal and thermoelectric properties of InN," *Applied Physics Letters*, vol. 98, no. 1, pp. 1–4, 2011, ISSN: 00036951. DOI: 10.1063/1.3536507.

[81] T. R. Pavlov, S. C. Middlemas, B. D. Miller, F. Cappia, J. I. Cole, and J. J. Giglio, "Understanding the local thermal conductivity evolution of neutron irradiated U3Si2 dispersion fuel via state-of-the-art thermo-reflectance measurements," *Journal of Nuclear Materials*, vol. 557, p. 153 280, 2021, ISSN: 00223115. DOI: 10.1016/j.jnucmat.2021.153280. [Online]. Available: https://doi.org/10.1016/j.jnucmat.2021.153280.

[82] R. Cheaito, C. S. Gorham, A. Misra, K. Hattar, and P. E. Hopkins, "Thermal conductivity measurements via time-domain thermoreflectance for the characterization of radiation induced damage," *Journal of Materials Research*, vol. 30, no. 9, pp. 1403–1412, 2015, ISSN: 20445326. DOI: `10.1557/jmr.2015.11`.

[83] C. Moulet and M. S. Goorsky, "Lattice strain measurements in hydrogen implanted materials for layer transfer processes," in *Ion Implantation*, M. Goorsky, Ed. InTech, 2012, pp. 65–88, ISBN: 978-953-51-0634-0.

[84] J. Lindhard, "Influence of Crystal Lattice on Motion of Energetic Charged Particles," *Mat. Fys. Medd. Dan. Vid. Selsk.*, vol. 34, pp. 1–64, 1965.

[85] E. Chason, S. T. Picraux, J. M. Poate, J. O. Borland, M. I. Current, T. Diaz De La Rubia, D. J. Eaglesham, O. W. Holland, M. E. Law, C. W. Magee, J. W. Mayer, J. Melngailis, and A. F. Tasch, "Ion beams in silicon processing and characterization," *Journal of Applied Physics*, vol. 81, no. 10, pp. 6513–6561, 1997, ISSN: 00218979. DOI: `10.1063/1.365193`.

[86] R. G. Wilson, H. L. Dunlap, D. M. Jamba, and D. R. Myers, *Semiconductor Measurement Technology: Angular Sensitivity of Controlled Implanted Doping Profiles*. U.S. Department of Commerce, National Bureau of Standards, 1978.

[87] J Wood, "Ion Implantation," in *Encyclopedia of Materials: Science and Technology*, K. H. J. Buschow, R. W. Cahn, M. C. Flemings, B. Ilschner, E. J. Kramer, S. Mahajan, and P. Veyssière, Eds., Oxford: Elsevier, 2001, pp. 4284–4286, ISBN: 978-0-08-043152-9. DOI: `https://doi.org/10.1016/B0-08-043152-6/00751-8`. [Online]. Available: `https://www.sciencedirect.com/science/article/pii/B0080431526007518`.

[88] *Improvement of the reliability and accuracy of heavy ion beam analysis*. Vienna, Austria: n International Atomic Energy Agency (IAEA), 2019, ISBN: 978–92–0–103517–2.

[89] K. Hattar, M. J. Demkowicz, A. Misra, I. M. Robertson, and R. G. Hoagland, "Arrest of He bubble growth in Cu-Nb multilayer nanocomposites," *Scripta Materialia*, vol. 58, no. 7, pp. 541–544, 2008, ISSN: 13596462. DOI: `10.1016/j.scriptamat.2007.11.007`.

[90] F. F. Morehead, B. L. Crowder, and R. S. Title, "Formation of amorphous silicon by ion bombardment as a function of ion, temperature, and dose," *Journal of Applied Physics*, vol. 43, no. 3, pp. 1112–1118, 1972, ISSN: 00218979. DOI: `10.1063/1.1661223`.

[91] J. Wang, M. B. Toloczko, N. Bailey, F. A. Garner, J. Gigax, and L. Shao, "Modification of SRIM-calculated dose and injected ion profiles due to sputtering, injected ion buildup and void swelling," *Nuclear Instruments and Methods in Physics Research, Section B: Beam Interactions with Materials and Atoms*, vol. 387, pp. 20–28, 2016, ISSN: 0168583X. DOI: `10.1016/j.nimb.2016.09.015`. [Online]. Available: `http://dx.doi.org/10.1016/j.nimb.2016.09.015`.

[92] J. L. Pacheco, T. Byers, S. B. V. Deusen, D. L. Perry, D. Weathers, and E. Bielejec, "Comparing srim simulations and experimental results for shallow implantation of sb into s," 2016.

[93] A. Minnich and G. Chen, "Modified effective medium formulation for the thermal conductivity of nanocomposites," *Applied Physics Letters*, vol. 91, no. 7, pp. 1–4, 2007, ISSN: 00036951. DOI: 10.1063/1.2771040.

[94] S.-I. Tamura, "Isotope scattering," *Physical Review B*, vol. 27, no. 2, pp. 858–866, 1983. [Online]. Available: https://journals.aps.org/prb/pdf/10.1103/PhysRevB.27.858.

[95] R. Cheaito, J. C. Duda, T. E. Beechem, K. Hattar, J. F. Ihlefeld, D. L. Medlin, M. A. Rodriguez, M. J. Campion, E. S. Piekos, and P. E. Hopkins, "Experimental investigation of size effects on the thermal conductivity of silicon-germanium alloy thin films," *Physical Review Letters*, vol. 109, no. 19, pp. 1–5, 2012, ISSN: 00319007. DOI: 10.1103/PhysRevLett.109.195901.

[96] J. Garg, N. Bonini, B. Kozinsky, and N. Marzari, "Role of disorder and anharmonicity in the thermal conductivity of silicon-germanium alloys: A first-principles study," *Physical Review Letters*, vol. 106, no. 4, pp. 1–4, 2011, ISSN: 00319007. DOI: 10.1103/PhysRevLett.106.045901.

[97] D. G. Cahill and F. Watanabe, "Thermal conductivity of isotopically pure and Ge-doped Si epitaxial layers from 300 to 550 K," *Physical Review B - Condensed Matter and Materials Physics*, vol. 70, no. 23, pp. 1–3, 2004, ISSN: 1550235X. DOI: 10.1103/PhysRevB.70.235322.

[98] D. G. Cahill, F. Watanabe, A. Rockett, and C. B. Vining, "Thermal conductivity of epitaxial layers of dilute SiGe alloys," *Physical Review B - Condensed Matter and Materials Physics*, vol. 71, no. 23, pp. 1–4, 2005, ISSN: 10980121. DOI: 10.1103/PhysRevB.71.235202.

[99] C. Ratsifaritana and P. Klemens, "Scattering of Phonons by Vacancies," *International Journal of Thermophysics*, vol. 8, no. 6, pp. 737–750, 1987. DOI: 10.1103/PhysRevB.36.3042.

[100] Y. Lee, S. Lee, and G. S. Hwang, "Effects of vacancy defects on thermal conductivity in crystalline silicon: A nonequilibrium molecular dynamics study," *Physical Review B - Condensed Matter and Materials Physics*, vol. 83, no. 12, pp. 27–29, 2011, ISSN: 10980121. DOI: 10.1103/PhysRevB.83.125202.

[101] M. Wittmer, J. Roth, P. Revesz, and J. W. Mayer, "Epitaxial regrowth of Ne- and Kr-implanted amorphous silicon," *Journal of Applied Physics*, vol. 49, no. 10, pp. 5207–5212, 1978, ISSN: 00218979. DOI: 10.1063/1.324416.

[102] R. J. Kaplar, A. A. Allerman, A. M. Armstrong, M. H. Crawford, J. R. Dickerson, A. J. Fischer, A. G. Baca, and E. A. Douglas, "Review—Ultra-Wide-Bandgap AlGaN Power Electronic Devices," *ECS Journal of Solid State Science and Technology*, vol. 6, no. 2, Q3061–Q3066, 2017, ISSN: 2162-8769. DOI: 10.1149/2.0111702jss.

[103] T. S. English, J. C. Duda, J. L. Smoyer, D. A. Jordan, P. M. Norris, and L. V. Zhigilei, “Enhancing and tuning phonon transport at vibrationally mismatched solid-solid interfaces,” *Physical Review B - Condensed Matter and Materials Physics*, vol. 85, no. 3, pp. 1–14, 2012, ISSN: 10980121. DOI: 10.1103/PhysRevB.85.035438.

[104] Z. Liang and H. L. Tsai, “Effect of thin film confined between two dissimilar solids on interfacial thermal resistance,” *Journal of Physics Condensed Matter*, vol. 23, no. 49, 2011, ISSN: 09538984. DOI: 10.1088/0953-8984/23/49/495303.

[105] J. C. Duda and P. E. Hopkins, “Systematically controlling Kapitza conductance via chemical etching,” *Applied Physics Letters*, vol. 100, no. 11, 2012, ISSN: 00036951. DOI: 10.1063/1.3695058.

[106] A. Giri, R. Cheaito, J. T. Gaskins, T. Mimura, H. J. Brown-Shaklee, D. L. Medlin, J. F. Ihlefeld, and P. E. Hopkins, “Thickness-Independent Vibrational Thermal Conductance across Confined Solid-Solution Thin Films,” *ACS Applied Materials and Interfaces*, vol. 13, no. 10, pp. 12 541–12 549, 2021, ISSN: 19448252. DOI: 10.1021/acsami.0c20608.

[107] R. Rastgarkafshgarkolaei, J. Zhang, C. A. Polanco, N. Q. Le, A. W. Ghosh, and P. M. Norris, “Maximization of thermal conductance at interfaces via exponentially mass-graded interlayers,” *Nanoscale*, vol. 11, no. 13, pp. 6254–6262, 2019, ISSN: 20403372. DOI: 10.1039/C8NR09188A.

[108] S Woo, K and Malakoutian, M and Jo, Y and Zheng, X and Pfeifer, T and Mandia, R and Hwang, T and Aller, H and Field, D and Kasperovich, A and Saraswat, D and Hopkins, P and Graham, S and Kuball, M and Cho, K and Chowdhury, “Interlayer Engineering to Achieve 1m2KGW Thermal Boundary Resistances to Diamond for Effective Device Cooling,” *International Electron Devices Meeting*, vol. 9, pp. 51–54, 2023. DOI: 10.1109/IEDM45741.2023.10413734.

[109] M. Malakoutian, K. Woo, D. Rich, R. Mandia, X. Zheng, A. Kasperovich, D. Saraswat, R. Soman, Y. Jo, T. Pfeifer, T. Hwang, H. Aller, J. Kim, J. Lyu, J. K. Mabrey, T. A. Rodriguez, J. Pomeroy, P. E. Hopkins, S. Graham, D. J. Smith, S. Mitra, K. Cho, M. Kuball, and S. Chowdhury, “Lossless phonon transition through gan-diamond and si-diamond interfaces,” *Advanced Electronic Materials*, vol. n/a, no. n/a, p. 2 400 146, DOI: https://doi.org/10.1002/aelm.202400146. eprint: https://onlinelibrary.wiley.com/doi/pdf/10.1002/aelm.202400146. [Online]. Available: https://onlinelibrary.wiley.com/doi/abs/10.1002/aelm.202400146.

[110] O. Babchenko, J. Dzuba, T. Lalinský, M. Vojs, A. Vincze, T. Ižák, and G. Vanko, “Stability of algan/gan heterostructures after hydrogen plasma treatment,” *Applied Surface Science*, vol. 395, pp. 92–97, 2017, Progress in Applied Surface, Interface and Thin Film Science and Solar Renewable Energy News IV, ISSN: 0169-4332. DOI: https://doi.org/10.1016/j.apsusc.2016.06.105. [Online]. Available: https://www.sciencedirect.com/science/article/pii/S0169433216313344.

[111] W. Ih Choi, K. Kim, and S. Narumanchi, “Thermal conductance at atomically clean and disordered silicon/aluminum interfaces: A molecular dynamics simulation study,” *Journal of Applied Physics*, vol. 112, no. 5, 2012, ISSN: 00218979. DOI: `10.1063/1.4748872`.

[112] A. Van Roekeghem, B. Vermeersch, J. Carrete, and N. Mingo, “Thermal Resistance of Ga N / Al N Graded Interfaces,” *Physical Review Applied*, vol. 11, no. 3, pp. 1–6, 2019, ISSN: 23317019. DOI: `10.1103/PhysRevApplied.11.034036`. arXiv: `1809.11046`.

[113] J. C. Duda, T. S. English, E. S. Piekos, T. E. Beechem, T. W. Kenny, and P. E. Hopkins, “Bidirectionally tuning Kapitza conductance through the inclusion of substitutional impurities,” *Journal of Applied Physics*, vol. 112, no. 7, 2012, ISSN: 00218979. DOI: `10.1063/1.4757941`.

[114] T. Beechem and P. E. Hopkins, “Predictions of thermal boundary conductance for systems of disordered solids and interfaces,” *Journal of Applied Physics*, vol. 106, no. 12, 2009, ISSN: 00218979. DOI: `10.1063/1.3267496`.

[115] P. E. Hopkins, P. M. Norris, R. J. Stevens, T. E. Beechem, and S. Graham, “Influence of interfacial mixing on thermal boundary conductance across a chromium/silicon interface,” *Journal of Heat Transfer*, vol. 130, no. 6, pp. 1–10, 2008, ISSN: 15288943. DOI: `10.1115/1.2897344`.

[116] S. Yang, H. Song, Y. Peng, L. Zhao, Y. Tong, F. Kang, M. Xu, B. Sun, and X. Wang, “Reduced thermal boundary conductance in GaN-based electronic devices introduced by metal bonding layer,” *Nano Research*, vol. 14, no. 10, pp. 3616–3620, 2021, ISSN: 19980000. DOI: `10.1007/s12274-021-3658-7`.

[117] X. W. Zhou, R. E. Jones, C. J. Kimmer, J. C. Duda, and P. E. Hopkins, “Relationship of thermal boundary conductance to structure from an analytical model plus molecular dynamics simulations,” *Physical Review B - Condensed Matter and Materials Physics*, vol. 87, no. 9, pp. 21–27, 2013, ISSN: 10980121. DOI: `10.1103/PhysRevB.87.094303`.

[118] Z. Liang, K. Sasikumar, and P. Keblinski, “Thermal transport across a substrate-thin-film interface: Effects of film thickness and surface roughness,” *Physical Review Letters*, vol. 113, no. 6, pp. 1–5, 2014, ISSN: 10797114. DOI: `10.1103/PhysRevLett.113.065901`.

[119] P. E. Hopkins, J. C. Duda, and P. M. Norris, “Anharmonic phonon interactions at interfaces and contributions to thermal boundary conductance,” *Journal of Heat Transfer*, vol. 133, no. 6, pp. 1–11, 2011, ISSN: 00221481. DOI: `10.1115/1.4003549`.

[120] Z. Cheng, Y. R. Koh, H. Ahmad, R. Hu, J. Shi, M. E. Liao, Y. Wang, T. Bai, R. Li, E. Lee, E. A. Clinton, C. M. Matthews, Z. Engel, L. Yates, T. Luo, M. S. Goorsky, W. A. Doolittle, Z. Tian, P. E. Hopkins, and S. Graham, “Thermal conductance across harmonic-matched epitaxial Al-sapphire heterointerfaces,” *Communications Physics*, vol. 3, no. 1, pp. 1–8, 2020, ISSN: 23993650. DOI: `10.1038/s42005-`

020-0383-6. arXiv: 1906.05484. [Online]. Available: http://dx.doi.org/10.1038/s42005-020-0383-6.

[121] K. Gordiz and A. Henry, "Phonon transport at interfaces between different phases of silicon and germanium," *Journal of Applied Physics*, vol. 121, no. 2, 2017, ISSN: 10897550. DOI: 10.1063/1.4973573. [Online]. Available: http://dx.doi.org/10.1063/1.4973573.

[122] Z. Lu, A. M. Chaka, and P. V. Sushko, "Thermal conductance enhanced via inelastic phonon transport by atomic vacancies at Cu/Si interfaces," *Physical Review B*, vol. 102, no. 7, pp. 1–14, 2020, ISSN: 24699969. DOI: 10.1103/PhysRevB.102.075449.

[123] J. C. Duda, P. M. Norris, and P. E. Hopkins, "On the linear temperature dependence of phonon thermal boundary conductance in the classical limit," *Journal of Heat Transfer*, vol. 133, no. 7, pp. 2–5, 2011, ISSN: 00221481. DOI: 10.1115/1.4003575.

[124] X. Wu and T. Luo, "The importance of anharmonicity in thermal transport across solid-solid interfaces," *Journal of Applied Physics*, vol. 115, no. 1, 2014, ISSN: 00218979. DOI: 10.1063/1.4859555.

[125] T. Murakami, T. Hori, T. Shiga, and J. Shiomi, "Probing and tuning inelastic phonon conductance across finite-thickness interface," *Applied Physics Express*, vol. 7, no. 12, p. 121 801, 2014, ISSN: 18820786. DOI: 10.7567/APEX.7.121801.

[126] J. Shi, Y. Dong, T. Fisher, and X. Ruan, "Thermal transport across carbon nanotube-graphene covalent and van der Waals junctions," *Journal of Applied Physics*, vol. 118, no. 4, 2015, ISSN: 10897550. DOI: 10.1063/1.4927273. [Online]. Available: http://dx.doi.org/10.1063/1.4927273.

[127] N. Q. Le, C. A. Polanco, R. Rastgarkafshgarkolaei, J. Zhang, A. W. Ghosh, and P. M. Norris, "Effects of bulk and interfacial anharmonicity on thermal conductance at solid/solid interfaces," *Physical Review B*, vol. 95, no. 24, pp. 1–8, 2017, ISSN: 24699969. DOI: 10.1103/PhysRevB.95.245417.

[128] E. Lee and T. Luo, "Thermal transport across solid-solid interfaces enhanced by pre-interface isotope-phonon scattering," *Applied Physics Letters*, vol. 112, no. 1, 2018, ISSN: 00036951. DOI: 10.1063/1.5003827.

[129] J. Maassen and V. Askarpour, "Phonon transport across a Si-Ge interface: The role of inelastic bulk scattering," *APL Materials*, vol. 7, no. 1, 2019, ISSN: 2166532X. DOI: 10.1063/1.5051538. [Online]. Available: http://dx.doi.org/10.1063/1.5051538.

[130] Y. Guo, Z. Zhang, M. Bescond, S. Xiong, M. Nomura, and S. Volz, "Anharmonic phonon-phonon scattering at the interface between two solids by nonequilibrium Green's function formalism," *Physical Review B*, vol. 103, no. 17, pp. 1–8, 2021, ISSN: 24699969. DOI: 10.1103/PhysRevB.103.174306.

[131] P. E. Hopkins, J. A. Tomko, and A. Giri, “Quasi-harmonic theory for phonon thermal boundary conductance at high temperatures,” *Journal of Applied Physics*, vol. 131, no. 1, 2022, ISSN: 10897550. DOI: 10.1063/5.0071429.

[132] D. H. Olson, J. L. Braun, and P. E. Hopkins, “Spatially resolved thermoreflectance techniques for thermal conductivity measurements from the nanoscale to the mesoscale,” *Journal of Applied Physics*, vol. 126, no. 15, 2019, ISSN: 10897550. DOI: 10.1063/1.5120310.

[133] R. J. Stevens, L. V. Zhigilei, and P. M. Norris, “Effects of temperature and disorder on thermal boundary conductance at solid-solid interfaces: Nonequilibrium molecular dynamics simulations,” *International Journal of Heat and Mass Transfer*, vol. 50, no. 19-20, pp. 3977–3989, 2007, ISSN: 00179310. DOI: 10.1016/j.ijheatmasstransfer.2007.01.040.

[134] Z. Tian, K. Esfarjani, and G. Chen, “Enhancing phonon transmission across a Si/Ge interface by atomic roughness: First-principles study with the Green’s function method,” *Physical Review B - Condensed Matter and Materials Physics*, vol. 86, no. 23, pp. 1–7, 2012, ISSN: 10980121. DOI: 10.1103/PhysRevB.86.235304.

[135] Z. Liang and P. Keblinski, “Finite-size effects on molecular dynamics interfacial thermal-resistance predictions,” *Physical Review B - Condensed Matter and Materials Physics*, vol. 90, no. 7, pp. 1–12, 2014, ISSN: 1550235X. DOI: 10.1103/PhysRevB.90.075411.

[136] C. S. Gorham, K. Hattar, R. Cheaito, J. C. Duda, J. T. Gaskins, T. E. Beechem, J. F. Ihlefeld, L. B. Biedermann, E. S. Piekos, D. L. Medlin, and P. E. Hopkins, “Ion irradiation of the native oxide/silicon surface increases the thermal boundary conductance across aluminum/silicon interfaces,” *Physical Review B - Condensed Matter and Materials Physics*, vol. 90, no. 2, pp. 1–10, 2014, ISSN: 1550235X. DOI: 10.1103/PhysRevB.90.024301.

[137] K. Gordiz and A. Henry, “Phonon transport at crystalline Si/Ge interfaces: The role of interfacial modes of vibration,” *Scientific Reports*, vol. 6, no. February, pp. 1–9, 2016, ISSN: 20452322. DOI: 10.1038/srep23139.

[138] A. P. Thompson, H. M. Aktulga, R. Berger, D. S. Bolintineanu, W. M. Brown, P. S. Crozier, P. J. in ’t Veld, A. Kohlmeyer, S. G. Moore, T. D. Nguyen, R. Shan, M. J. Stevens, J. Tranchida, C. Trott, and S. J. Plimpton, “LAMMPS - a flexible simulation tool for particle-based materials modeling at the atomic, meso, and continuum scales,” *Comp. Phys. Comm.*, vol. 271, p. 108 171, 2022. DOI: 10.1016/j.cpc.2021.108171.

[139] Z. Fan, H. Dong, A. Harju, and T. Ala-nissila, “PHYSICAL REVIEW B 99 , 064308 (2019) Homogeneous nonequilibrium molecular dynamics method for heat transport and spectral decomposition with many-body potentials,” vol. 064308, pp. 1–9, 2019. DOI: 10.1103/PhysRevB.99.064308.

[140] R. Li, K. Gordiz, A. Henry, P. E. Hopkins, E. Lee, and T. Luo, "Effect of light atoms on thermal transport across solid-solid interfaces," *Physical Chemistry Chemical Physics*, vol. 21, no. 31, pp. 17 029–17 035, 2019, ISSN: 14639076. DOI: 10.1039/c9cp03426a.

[141] A. J. Gabourie, Z. Fan, T. Ala-Nissila, and E. Pop, "Spectral decomposition of thermal conductivity: Comparing velocity decomposition methods in homogeneous molecular dynamics simulations," *Physical Review B*, vol. 103, no. 20, pp. 1–19, 2021, ISSN: 2469-9950. DOI: 10.1103/physrevb.103.205421.

[142] T. Zhou, H. K. Chilukoti, Z. Wu, and F. Müller-Plathe, "Effect of Defects on the Interfacial Thermal Conductance betweenn-Heneicosane in Solid and Liquid Phases and a Graphene Monolayer," *Journal of Physical Chemistry C*, vol. 125, no. 25, pp. 14 149–14 162, 2021, ISSN: 19327455. DOI: 10.1021/acs.jpcc.1c04676.

[143] J. Han, H. T. Aller, and A. J. H. McGaughey, "Quantifying Atomic Structural Disorder Using Procrustes Shape Analysis," pp. 1–6, 2023. arXiv: 2303.04108. [Online]. Available: http://arxiv.org/abs/2303.04108.

[144] W. G. Hoover, "Canonical dynamics: Equilibrium phase-space distributions," *Phys. Rev. A*, vol. 31, pp. 1695–1697, 3 1985. DOI: 10.1103/PhysRevA.31.1695. [Online]. Available: https://link.aps.org/doi/10.1103/PhysRevA.31.1695.

[145] J. Hickman and Y. Mishin, "Temperature fluctuations in canonical systems: Insights from molecular dynamics simulations," *Phys. Rev. B*, vol. 94, p. 184 311, 18 2016. DOI: 10.1103/PhysRevB.94.184311. [Online]. Available: https://link.aps.org/doi/10.1103/PhysRevB.94.184311.

[146] J. Dunn, E. Antillon, J. Maassen, M. Lundstrom, and A. Strachan, "Role of energy distribution in contacts on thermal transport in si: A molecular dynamics study," *Journal of Applied Physics*, vol. 120, no. 22, p. 225 112, Dec. 2016, ISSN: 0021-8979. DOI: 10.1063/1.4971254. eprint: https://pubs.aip.org/aip/jap/article-pdf/doi/10.1063/1.4971254/15188131/225112_1_online.pdf. [Online]. Available: https://doi.org/10.1063/1.4971254.

[147] A. J. Page, T. Isomoto, J. M. Knaup, S. Irle, and K. Morokuma, "Effects of molecular dynamics thermostats on descriptions of chemical nonequilibrium," *Journal of Chemical Theory and Computation*, vol. 8, no. 11, pp. 4019–4028, 2012, PMID: 26605569. DOI: 10.1021/ct3004639. eprint: https://doi.org/10.1021/ct3004639. [Online]. Available: https://doi.org/10.1021/ct3004639.

[148] Z. Li, S. Xiong, C. Sievers, Y. Hu, Z. Fan, N. Wei, H. Bao, S. Chen, D. Donadio, and T. Ala-Nissila, "Influence of thermostatting on nonequilibrium molecular dynamics simulations of heat conduction in solids," *The Journal of Chemical Physics*, vol. 151, no. 23, p. 234 105, Dec. 2019, ISSN: 0021-9606. DOI: 10.1063/1.5132543. eprint: https://pubs.aip.org/aip/jcp/article-pdf/doi/10.1063/1.5132543/15566205/234105_1_online.pdf. [Online]. Available: https://doi.org/10.1063/1.5132543.

[149] W. Marciniak, J. Marciniak, J. Ángel Castellanos-Reyes, and J. Rusz, *Mode-dependent phonon relaxation in fcc ni: Insights from molecular dynamics simulations with frozen-trajectory excitations*, 2024. arXiv: 2409.20334 [cond-mat.mtrl-sci]. [Online]. Available: https://arxiv.org/abs/2409.20334.

[150] T. Q. Qiu and C. L. Tien, "Heat transfer mechanisms during short-pulse laser heating of metals," *Journal of Heat Transfer (Transactions of the ASME (American Society of Mechanical Engineers), Series C); (United States)*, vol. 115:4, Nov. 1993, ISSN: ISSN 0022-1481. DOI: 10.1115/1.2911377. [Online]. Available: https://www.osti.gov/biblio/5549075.

[151] P. E. Hopkins and P. M. Norris, "Substrate influence in electron–phonon coupling measurements in thin au films," *Applied Surface Science*, vol. 253, no. 15, pp. 6289–6294, 2007, Proceedings of the Fifth International Conference on Photo-Excited Processes and Applications, ISSN: 0169-4332. DOI: https://doi.org/10.1016/j.apsusc.2007.01.065. [Online]. Available: https://www.sciencedirect.com/science/article/pii/S0169433207001298.

[152] J. A. Tomko, S. Kumar, R. Sundararaman, and P. E. Hopkins, "Temperature dependent electron–phonon coupling of au resolved via lattice dynamics measured with sub-picosecond infrared pulses," *Journal of Applied Physics*, vol. 129, no. 19, p. 193 104, May 2021, ISSN: 0021-8979. DOI: 10.1063/5.0043950. eprint: https://pubs.aip.org/aip/jap/article-pdf/doi/10.1063/5.0043950/15260678/193104_1_online.pdf. [Online]. Available: https://doi.org/10.1063/5.0043950.

[153] L. A. Giannuzzi and F. A. Stevie, "A review of focused ion beam milling techniques for TEM specimen preparation," *Micron*, vol. 30, no. 3, pp. 197–204, 1999, ISSN: 09684328. DOI: 10.1016/S0968-4328(99)00005-0.

[154] W. J. MoberlyChan, D. P. Adams, M. J. Aziz, G. Hobler, and T. Schenkel, "Fundamentals of focused ion beam nanostructural processing: Below, at, and above the surface," *MRS Bulletin*, vol. 32, no. 5, pp. 424–432, 2007, ISSN: 08837694. DOI: 10.1557/mrs2007.66.

[155] J. M. Cairney and P. R. Munroe, "Redeposition effects in transmission electron microscope specimens of FeAl-WC composites prepared using a focused ion beam," *Micron*, vol. 34, no. 2, pp. 97–107, 2003, ISSN: 09684328. DOI: 10.1016/S0968-4328(03)00007-6.

[156] D. A. M. de Winter and J. J. L. Mulders, "Redeposition characteristics of focused ion beam milling for nanofabrication," *Journal of Vacuum Science Technology B: Microelectronics and Nanometer Structures Processing, Measurement, and Phenomena*, vol. 25, no. 6, pp. 2215–2218, 2007, ISSN: 1071-1023. DOI: 10.1116/1.2806973.

[157] T. Vermeij, E. Plancher, and C. C. Tasan, "Preventing damage and redeposition during focused ion beam milling: The "umbrella" method," *Ultramicroscopy*, vol. 186, pp. 35–41, 2018, ISSN: 18792723. DOI: 10.1016/j.ultramic.2017.12.012. [Online]. Available: https://doi.org/10.1016/j.ultramic.2017.12.012.

[158] N. I. Kato, "Reducing focused ion beam damage to transmission electron microscopy samples," *Journal of Electron Microscopy*, vol. 53, no. 5, pp. 451–458, 2004, ISSN: 00220744. DOI: 10.1093/jmicro/dfh080.

[159] J. Huang, M. Loeffler, U. Muehle, W. Moeller, J. J. Mulders, L. F. Kwakman, W. F. Van Dorp, and E. Zschech, "Si amorphization by focused ion beam milling: Point defect model with dynamic BCA simulation and experimental validation," *Ultramicroscopy*, vol. 184, pp. 52–56, 2018, ISSN: 18792723. DOI: 10.1016/j.ultramic.2017.10.011. [Online]. Available: https://doi.org/10.1016/j.ultramic.2017.10.011.

[160] C. Lehrer, L. Frey, S. Petersen, M. Mizutam, M. Takai, and H. Ryssel, "Defects and gallium - Contamination during focused ion beam micro machining," *Proceedings of the International Conference on Ion Implantation Technology*, pp. 695–698, 2000. DOI: 10.1109/.2000.924248.

[161] B. A. Lucas and N. Grigorieff, "Quantification of gallium cryo-fib milling damage in biological lamellae," *Proceedings of the National Academy of Sciences*, vol. 120, no. 23, e2301852120, 2023. DOI: 10.1073/pnas.2301852120. eprint: https://www.pnas.org/doi/pdf/10.1073/pnas.2301852120. [Online]. Available: https://www.pnas.org/doi/abs/10.1073/pnas.2301852120.

[162] Y. Kwon, B. S. An, Y. J. Shin, and C. W. Yang, "Method of Ga removal from a specimen on a microelectromechanical system-based chip for in-situ transmission electron microscopy," *Applied Microscopy*, vol. 50, no. 1, pp. 0–5, 2020, ISSN: 22874445. DOI: 10.1186/s42649-020-00043-6.

[163] J. Liu, J. Zhu, M. Tian, X. Gu, A. Schmidt, and R. Yang, "Simultaneous measurement of thermal conductivity and heat capacity of bulk and thin film materials using frequency-dependent transient thermoreflectance method," *Review of Scientific Instruments*, vol. 84, no. 3, 2013, ISSN: 00346748. DOI: 10.1063/1.4797479.

[164] E. A. Scott, J. T. Gaskins, S. W. King, and P. E. Hopkins, "Thermal conductivity and thermal boundary resistance of atomic layer deposited high- k dielectric aluminum oxide, hafnium oxide, and titanium oxide thin films on silicon," *APL Materials*, vol. 6, no. 5, p. 058 302, 2018, ISSN: 2166532X. DOI: 10.1063/1.5021044. [Online]. Available: http://dx.doi.org/10.1063/1.5021044.

[165] A. A. Volfson and V. K. Subashiev, "Differential Reflection Spectra of Heavily Doped Silicon and Germanium in the Ultraviolet Spectral Region," *Physica Status Solidi (B)*, vol. 33, no. 1, pp. 149–159, 1969, ISSN: 15213951. DOI: 10.1002/pssb.19690330112.

[166] A. Salnick and J. Opsal, "Quantitative photothermal characterization of ion-implanted layers in Si," *Journal of Applied Physics*, vol. 91, no. 5, pp. 2874–2882, 2002, ISSN: 00218979. DOI: 10.1063/1.1448410.

[167] A. Salnick and J. Opsal, "Dynamics of the plasma and thermal waves in surface-modified semiconductors (invited)," *Review of Scientific Instruments*, vol. 74, no. 1 II, pp. 545–549, 2003, ISSN: 00346748. DOI: 10.1063/1.1517154.

[168] J. Mayer, L. a. Giannuzzi, T. Kamino, and J. Michael, “TEM Sample Preparation and Damage,” *MRS Bulletin*, vol. 32, no. May, pp. 400–407, 2007.

[169] D. J. Graham and L. J. Gamble, “Back to the basics of time-of-flight secondary ion mass spectrometry of bio-related samples. I. Instrumentation and data collection,” *Biointerphases*, vol. 18, no. 2, 2023, ISSN: 1934-8630. DOI: `10.1116/6.0002477`.

[170] T. Tanaka, A. Harata, and T. Sawada, “Subpicosecond surface-restricted carrier and thermal dynamics by transient reflectivity measurements,” *Journal of Applied Physics*, vol. 82, no. 8, pp. 4033–4038, 1997, ISSN: 00218979. DOI: `10.1063/1.365713`.

[171] T. Maisch, C. W, T. Mi, and C Kalbitzer, “Energy spread of a focused ion beam system with a supertip,” *Nuclear Instruments and Methods in Physics Research*, vol. 81, pp. 1288–1291, 1993.

[172] G. ten Haaf, S. H. Wouters, D. F. Nijhof, P. H. Mutsaers, and E. J. Vredenbregt, “Measurements of the energy distribution of a high brightness rubidium ion beam,” *Ultramicroscopy*, vol. 190, pp. 12–20, 2018, ISSN: 18792723. DOI: `10.1016/j.ultramic.2018.03.014`. [Online]. Available: `https://doi.org/10.1016/j.ultramic.2018.03.014`.

[173] H. S. Uhm, E. H. Choi, G. S. Cho, and S. O. Kang, “Energy Distribution Properties of Focused Ion Beams From Liquid Metal Ion Sources,” *IEEE*, no. June, p. 7405, 1995.

[174] G. Masetti, M. Severi, and S. Solmi, “Modeling of Carrier Mobility Against Carrier Concentration in Arsenic-, Phosphorus-, and Boron-Doped Silicon,” *IEEE Transactions on Electron Devices*, vol. 30, no. 7, pp. 764–769, 1983, ISSN: 15579646. DOI: `10.1109/T-ED.1983.21207`.

[175] Y. Abe, Toshio Nishi, “Non-destructive measurement of surface concentrations and junction depths of diffused semiconductor layers,” *Japanese Journal of Applied Physics*, vol. 7, no. 4, p. 397, 1968, ISSN: 13474065. DOI: `10.1143/JJAP.7.397`.

[176] F. R. Kessler and E. Barta, “Optical constants and free carrier data of heavily doped semiconductors from reflection measurements in the infrared,” *Physica Status Solidi (a)*, vol. 9, no. 2, pp. 469–475, 1972, ISSN: 1521396X. DOI: `10.1002/pssa.2210090208`.

[177] P. Gill, T. T. Moghadam, and B. Ranjbar, “Differential Scanning Calorimetry Techniques: Applications in Biology and Nanoscience,” *Journal of Biomolecular Techniques*, vol. 21, pp. 167–193, 2010, ISSN: 14645491. DOI: `10.1111/dme.13173`.

[178] G Pottlacher, E Kaschnitz, and H Jager, “High-pressure, high-temperature thermophysical measurements on molybdenum,” *Journal of Physics: Condensed Matter*, vol. 3, no. 31, p. 5783, 1991. DOI: `10.1088/0953-8984/3/31/002`. [Online]. Available: `https://dx.doi.org/10.1088/0953-8984/3/31/002`.

[179] E. Kaschnitz, G. Pottlacher, and H. Jäger, "A new microsecond pulse-heating system to investigate thermophysical properties of solid and liquid metals," *International Journal of Thermophysics*, vol. 13, no. 4, pp. 699–710, 1992, ISSN: 0195928X. DOI: 10.1007/BF00501950.

[180] G. Wouch, "Containerless melting and resolidification of metals and alloys in the terrestrial and space environments," English, Copyright - Database copyright ProQuest LLC; ProQuest does not claim copyright in the individual underlying works; Last updated - 2023-02-19, Ph.D. dissertation, 1978, p. 172, ISBN: 9798661942012.

[181] E. C. Okress, D. M. Wroughton, G. Comenetz, P. H. Brace, and J. C. R. Kelly, "Electromagnetic Levitation of Solid and Molten Metals," *Journal of Applied Physics*, vol. 23, no. 5, pp. 545–552, May 1952, ISSN: 0021-8979. DOI: 10.1063/1.1702249. eprint: https://pubs.aip.org/aip/jap/article-pdf/23/5/545/18311308/545_1_online.pdf. [Online]. Available: https://doi.org/10.1063/1.1702249.

[182] L. Gao, Z. Shi, D. Li, G. Zhang, Y. Yang, A. McLean, and K. Chattopadhyay, "Applications of Electromagnetic Levitation and Development of Mathematical Models: A Review of the Last 15 Years (2000 to 2015)," *Metallurgical and Materials Transactions B: Process Metallurgy and Materials Processing Science*, vol. 47, no. 1, pp. 537–547, 2016, ISSN: 10735615. DOI: 10.1007/s11663-015-0522-8.

[183] J. H. Perepezko and G. Wilde, "Melt undercooling and nucleation kinetics," *Current Opinion in Solid State and Materials Science*, vol. 20, no. 1, pp. 3–12, 2016, ISSN: 13590286. DOI: 10.1016/j.cossms.2015.07.001. [Online]. Available: http://dx.doi.org/10.1016/j.cossms.2015.07.001.

[184] A. Munawar, Sadeeda, V. Asif, A. Jafri, F. Nisar, M. Wegener, J. Su, and F. Kargl, "Effect of Undercooling on the Microstructure and Mechanical Properties of Hypereutectic Ni–Sn Alloy," *Metallurgical and Materials Transactions A: Physical Metallurgy and Materials Science*, vol. 54, no. 11, pp. 4387–4395, 2023, ISSN: 10735623. DOI: 10.1007/s11661-023-07172-z. [Online]. Available: https://doi.org/10.1007/s11661-023-07172-z.

[185] J. Xu, D. Fan, and T. Zhang, "The effect of superheat on the nucleation undercooling of metallic melts," *Mathematical Methods in the Applied Sciences*, vol. 44, no. 16, pp. 12 351–12 359, 2021, ISSN: 10991476. DOI: 10.1002/mma.7471.

[186] D. Manara, C. Ronchi, M. Sheindlin, M. Lewis, and M. Brykin, "Melting of stoichiometric and hyperstoichiometric uranium dioxide," *Journal of Nuclear Materials*, vol. 342, no. 1-3, pp. 148–163, 2005, ISSN: 00223115. DOI: 10.1016/j.jnucmat.2005.04.002.

[187] "Investigating the highest melting temperature materials: A laser melting study of the TaC-HfC system," *Scientific Reports*, vol. 6, no. October, pp. 1–11, 2016, ISSN: 20452322. DOI: 10.1038/srep37962.

[188] D. Manara, L. Soldi, S. Mastromarino, K. Boboridis, D. Robba, L. Vlahovic, and R. Konings, “Laser-heating and radiance spectrometry for the study of nuclear materials in conditions simulating a nuclear power plant accident,” *Journal of Visualized Experiments*, vol. 2017, no. 130, 2017, ISSN: 1940087X. DOI: 10.3791/54807.

[189] M. Milich, H. B. Schonfeld, K. Boboridis, D. Robba, L. Vlahovic, R. J. Konings, J. L. Braun, J. T. Gaskins, N. Bhatt, A. Giri, and P. E. Hopkins, “Validation of the Wiedemann-Franz Law in Solid and Molten Tungsten above 2000 K through Thermal Conductivity Measurements via Steady-State Temperature Differential Radiometry,” *Physical Review Letters*, vol. 132, no. 14, p. 146 303, 2024, ISSN: 10797114. DOI: 10.1103/PhysRevLett.132.146303. arXiv: 2309.01062. [Online]. Available: https://doi.org/10.1103/PhysRevLett.132.146303.

[190] D. Manara, M. Sheindlin, W. Heinz, and C. Ronchi, “New techniques for high-temperature melting measurements in volatile refractory materials via laser surface heating,” *Review of Scientific Instruments*, vol. 79, no. 11, p. 113 901, Nov. 2008, ISSN: 0034-6748. DOI: 10.1063/1.3005994. eprint: https://pubs.aip.org/aip/rsi/article-pdf/doi/10.1063/1.3005994/14116376/113901_1_online.pdf. [Online]. Available: https://doi.org/10.1063/1.3005994.

[191] Y. S. Touloukian and D. P. DeWitt, *Thermophysical Properties of Matter - The TPRC Data Series. Volume 7 : Thermal Radiative Properties - Metallic Elements and Alloys*. 1970, ISBN: 306-67027-5.

[192] A. Araújo, “Multi-spectral pyrometry—a review,” en, *Measurement Science and Technology*, vol. 28, no. 8, p. 082 002, Aug. 2017, ISSN: 0957-0233, 1361-6501. DOI: 10.1088/1361-6501/aa7b4b. [Online]. Available: https://iopscience.iop.org/article/10.1088/1361-6501/aa7b4b (visited on 09/12/2024).

[193] Z. Zhang, M. Chen, L. Zhang, H. Li, H. Huang, Z. Zhang, P. Yu, Y. Niu, S. Gao, C. Wang, and J. Jiang, “A straightforward spectral emissivity estimating method based on constructing random rough surfaces,” *Light: Science and Applications*, vol. 12, no. 1, pp. 1–12, 2023, ISSN: 20477538. DOI: 10.1038/s41377-023-01312-1.

[194] Y. Suzaki and A. Tachibana, “Measurement of the μm sized radius of gaussian laser beam using the scanning knife-edge,” *Appl. Opt.*, vol. 14, no. 12, pp. 2809–2810, 1975. DOI: 10.1364/AO.14.002809. [Online]. Available: https://opg.optica.org/ao/abstract.cfm?URI=ao-14-12-2809.

[195] J. L. Braun, C. J. Szwejkowski, A. Giri, and P. E. Hopkins, “On the steady-state temperature rise during laser heating of multilayer thin films in optical pump-probe techniques,” *Journal of Heat Transfer*, vol. 140, no. 5, pp. 1–10, 2018, ISSN: 15288943. DOI: 10.1115/1.4038713.

[196] A. A. Saad, C. Martinez, and R. W. Trice, “Radiation heat transfer during hypersonic flight: A review of emissivity measurement and enhancement approaches of ultra-high temperature ceramics,” en, *International Journal of Ceramic Engineering & Science*, vol. 5, no. 2, e10171, Mar. 2023, ISSN: 2578-3270, 2578-3270. DOI: 10.1002/ces2.10171. [Online]. Available: https://ceramics.onlinelibrary.wiley.com/doi/10.1002/ces2.10171 (visited on 09/08/2023).

[197] H Watanabe, M Susa, and K Nagata, "Discontinuity in Normal Spectral Emissivity of Solid and Liquid Copper at the Melting Point," *Metallurgical and Materials Transactions A*, vol. 28, pp. 2507–2513, 1997. DOI: 10.1007/s11661-997-0008-7.

[198] H. Watanabe, M. Susa, H. Fukuyama, and K. Nagata, "Phase (Liquid / Solid) Dependence of the Normal Spectral Emissivity for Iron , Cobalt , and Nickel at Melting Points," *International Journal of Thermophysics*, vol. 24, no. 2, 2003.

[199] C. Cagran, C. Brunner, A. Seifter, and G. Pottlacher, "Liquid-phase behaviour of normal spectral emissivity at 684.5 nm of some selected metals," *High Temperatures - High Pressures*, vol. 34, no. 6, pp. 669–679, 2002, ISSN: 00181544. DOI: 10.1068/htjr067.

[200] C. Cagran, B. Wilthan, and G. Pottlacher, "Normal Spectral Emissivity at a Wavelength of 684.5 nm and Thermophysical Properties of Solid and Liquid Molybdenum," en, *International Journal of Thermophysics*, vol. 25, no. 5, pp. 1551–1566, Sep. 2004, ISSN: 0195-928X, 1572-9567. DOI: 10.1007/s10765-004-5758-5. [Online]. Available: http://link.springer.com/10.1007/s10765-004-5758-5 (visited on 09/09/2024).

[201] C. M. Rost, J. Braun, K. Ferri, L. Backman, A. Giri, E. J. Opila, J.-P. Maria, and P. E. Hopkins, "Hafnium nitride films for thermoreflectance transducers at high temperatures: Potential based on heating from laser absorption," *Appl. Phys. Lett.*, vol. 111, no. 15, Oct. 2017, ISSN: 0003-6951. DOI: 10.1063/1.5006648.

[202] Y. S. Touloukian, R. W. Powell, C. Y. Ho, and P. G. Klemens, *Thermophysical Properties of Matter - The TPRC Data Series. Volume 1 : Thermal conductivity - Metallic Elements and Alloys*. 1970, ISBN: 306-67021-6.

[203] Y. S. Touloukian and E. H. Buyco, *Thermophysical Properties of Matter - The TPRC Data Series. Volume 4 : Specific Heat - Metallic Elements and Alloys*. 1970, ISBN: 306-67024-0.

[204] H. A. Jones, I. Langmur, and G. M. MacKay, "The rates of evaporation and the vapor pressures of tungsten, molybdenum, platinum, nickel, iron, copper and silver," *Physical Review*, vol. 30, no. 2, pp. 201–214, 1927, ISSN: 0031899X. DOI: 10.1103/PhysRev.30.201.

[205] P. Tolias, "Analytical expressions for thermophysical properties of solid and liquid tungsten relevant for fusion applications," *Nuclear Materials and Energy*, vol. 13, pp. 42–57, 2017, ISSN: 23521791. DOI: 10.1016/j.nme.2017.08.002. arXiv: 1703.06302.

[206] P. F. Paradis and W. K. Rhim, "Noncontact Measurements of Thermophysical Properties of Molybdenum at High Temperatures," *International Journal of Thermophysics*, vol. 23, no. 1, pp. 555–569, 2002. DOI: 10.1023/A:1015169721771.

[207] A. Schmidt, M. Chiesa, X. Chen, and G. Chen, "An optical pump-probe technique for measuring the thermal conductivity of liquids," *Review of Scientific Instruments*, vol. 79, no. 6, 2008, ISSN: 00346748. DOI: 10.1063/1.2937458.

[208] P. E. Hopkins, B. Kaehr, L. M. Phinney, T. P. Koehler, A. M. Grillet, D. Dunphy, F. Garcia, and C. J. Brinker, "Measuring the thermal conductivity of porous, transparent SiO2 films with time domain thermoreflectance," *Journal of Heat Transfer*, vol. 133, no. 6, pp. 1–8, 2011, ISSN: 00221481. DOI: 10.1115/1.4003548.

[209] M. Laradji, D. P. Landau, and B Dünweg, "Structural properties of Si1-xGex alloys: A Monte Carlo simulation with the Stillinger-Weber potential," *Physical Review B*, vol. 51, no. 8, pp. 4894–4902, 1995, ISSN: 01631829. DOI: 10.1103/PhysRevB.51.4894.

[210] M. S. B. Hoque, Y. R. Koh, J. L. Braun, A. Mamun, Z. Liu, K. Huynh, M. E. Liao, K. Hussain, Z. Cheng, E. R. Hoglund, D. H. Olson, J. A. Tomko, K. Aryana, R. Galib, J. T. Gaskins, M. M. M. Elahi, Z. C. Leseman, J. M. Howe, T. Luo, S. Graham, M. S. Goorsky, A. Khan, and P. E. Hopkins, "High In-Plane Thermal Conductivity of Aluminum Nitride Thin Films," *ACS Nano*, vol. 15, no. 6, pp. 9588–9599, 2021, ISSN: 1936086X. DOI: 10.1021/acsnano.0c09915.